The Hepatic Compensatory Response to Elevated Systemic Sulfide Promotes Diabetes

Title

The Hepatic Compensatory Response to Elevated Systemic Sulfide Promotes Diabetes

Authors

Roderick N. Carter[1], Matthew T.G. Gibbins[1,a], Martin E. Barrios-Llerena[1,b], Stephen E. Wilkie[1,2], Peter L. Freddolino[3], Marouane Libiad[3,c], Victor Vitvitsky[3], Barry Emerson[1,d], Thierry Le Bihan[4,e], Madara Brice[1], Huizhong Su[5,f], Scott G. Denham[1], Natalie Z.M. Homer[1], Clare Mc Fadden[1,g], Anne Tailleux[6], Nourdine Faresse[7,h], Thierry Sulpice[7], Francois Briand[7], Tom Gillingwater[8], Kyo Han Ahn[9], Subhankar Singha[9,i], Claire McMaster[10], Richard C. Hartley[10], Bart Staels[6], Gillian A Gray[1], Andrew J. Finch[5,j], Colin Selman[2], Ruma Banerjee[3], Nicholas M. Morton[1*]

[1]University/British Heart Foundation Centre for Cardiovascular Science, University of Edinburgh, Queen's Medical Research Institute, Edinburgh, EH16 4TJ, United Kingdom

[2]Glasgow Ageing Research Network (GARNER), Institute of Biodiversity, Animal Health and Comparative Medicine, University of Glasgow, Glasgow, G12 8QQ, United Kingdom

[3]The Department of Biological Chemistry, University of Michigan Medical School, Ann Arbor, MI 48109, USA

[4]SynthSys - Systems and Synthethic Biology, Edinburgh, EH9 3JD, United Kingdom

[5]Cancer Research UK Edinburgh Centre, MRC Intitute of Genetics & Molecular Medicine, University of Edinburgh, Western General Hospital, Edinburgh, EH4 2XR, United Kingdom

[6]Université de Lille, Inserm, CHU Lille, Institut Pasteur de Lille, U101-EGID, F-59000, Lille, France

[7]Physiogenex S.A.S, Prologue Biotech, 516 rue Pierre et Marie Curie, 31670 Labège, France

[8]College of Medicine & Veterinary Medicine, University of Edinburgh, Old Medical School (Anatomy), Teviot Place, Edinburgh, EH8 9AG, United Kingdom

[9]Department of Chemistry, POSTECH, 77 Cheongam-Ro, Nam-Gu, Pohang, Gyungbuk, 37673, South Korea

[10]School of Chemistry, Joseph Black Building, University of Glasgow, Glasgow, G12 8QQ, United Kingdom

Current affiliations where different from the place where work for the manuscript was carried out;

[a]Cambridge Biomedical Campus, Royal Papworth Hospital NHS Foundation Trust, Cardiology department, Cambridge, CB2 0AY, United Kingdom

[b]The International Clinical Research Centre, St. Anne's University Hospital, Brno, 656 91, Czech Republic

[c]Institute for Integrative Biology of the Cell (I2BC), CEA, CNRS, Univ. Paris-Sud, Université Paris-Saclay, 91198, Gif-sur-Yvette cedex, France

[d]BD Research Centre Ireland, Co. Limerick, Castletroy, Ireland

[e]Rapid Novor Inc, 44 Gaukel St, Kitchener, ON N2G 4P3, Canada

[f]Wellcome Trust Centre for Mitochondrial Research, Newcastle University, NE2 4HH, United Kingdom

[g]Springer Nature Campus, London, N1 9FN, United Kingdom

[h]D.I.V.A-expertise, 1 place Pierre Potier, 31100 Toulouse, France

[i]Institute of Advanced Studies and Research, JIS University, Kolkata 700091, India

[j]Cancer Research UK Barts Centre, London, EC1M 6BQ, United Kingdom

* Lead contact

Nicholas M. Norton

nik.morton@ed.ac.uk

SUMMARY

Impaired hepatic glucose and lipid metabolism are hallmarks of type–2 diabetes. Increased sulfide production or sulfide–donor compounds may beneficially regulate hepatic metabolism. Disposal of sulfide through the sulfide oxidation pathway (SOP) is critical for maintaining sulfide within a safe physiological range. We show that mice lacking the liver–enriched mitochondrial SOP enzyme thiosulfate sulfur–transferase (*Tst*$^{-/-}$ mice) exhibit high circulating sulfide, increased gluconeogenesis, hypertriglyceridemia and fatty liver. Unexpectedly, hepatic sulfide levels are normal in *Tst*$^{-/-}$ mice due to exaggerated induction of sulfide disposal, with an associated suppression of global protein persulfidation and nuclear respiratory factor–2 target protein levels. Hepatic proteomic and persulfidomic profiles converge on gluconeogenesis and lipid metabolism, revealing a selective deficit in medium–chain fatty acid oxidation in *Tst*$^{-/-}$ mice. We reveal a critical role for TST in hepatic metabolism that has implications for sulfide-donor strategies in the context of metabolic disease.

INTRODUCTION

The prevalence of Type 2 diabetes (T2D) continues to soar in parallel with that of obesity (OMS, 2014). Increased hepatic glucose production and aberrant hepatic lipid metabolism are cardinal features of T2D (Consoli *et al.*, 1989; Lewis *et al.*, 2002). Dysregulation of hepatic nutrient metabolism in T2D is a promising area for therapeutic intervention because it precipitates the more severe liver pathologies that manifest along the spectrum of non-alcoholic fatty liver disease (NAFLD), steatosis, steatohepatitis and hepatocellular carcinoma (Caron *et al.*, 2011).

Hydrogen sulfide (hereafter referred to as sulfide), an endogenously produced gaseous signalling molecule (Abe and Kimura, 1996; Wang, 2012; Mishanina, Libiad and Banerjee, 2015; Filipovic *et al.*, 2017), has recently emerged as a modulator of nutrient metabolism (Desai *et al.*, 2011; Szabo, 2011; Hine *et al.*, 2015; Carter and Morton, 2016). Enzymatic sulfide production from sulfur amino acids is catalysed by cystathionine beta–synthase; CBS, and cystathionine gamma lyase; CTH (Chen, Jhee and Kruger, 2004; Singh *et al.*, 2009) and by 3-mercaptopyruvate sulfur transferase; MPST (Shibuya *et al.*, 2009; Mikami *et al.*, 2011; Yadav *et al.*, 2013). Thioredoxin-mediated reduction of cysteine persulfides on proteins also regulates free sulfide and cysteine persulfide levels (Wedmann *et al.*, 2016). Endogenously produced and exogenously administered sulfide specifically influences hepatic glucose and lipid metabolism (Mani *et al.*, 2014; Pichette and Gagnon, 2016). Thus, *in vitro,* treatment of murine hepatocytes with NaHS, or overexpression of rat *Cth* in HepG2 liver cells, increased glucose production through increased gluconeogenesis and reduced glycogen storage (Zhang *et al.*, 2013). Conversely, glucose production was lower in hepatocytes from *Cth* gene knockout mice ($Cth^{-/-}$ mice) that exhibit low sulfide production (Zhang *et al.*, 2013). Elevation of sulfide with NaHS administration *in vivo* reduced cholesterol and triglyceride accumulation

in the liver of high fat diet (HFD)–fed mice (Wu *et al.*, 2015). In contrast, inter-cross of sulfide production–deficient *Cth*$^{-/-}$ mice with the hyperlipidemic *Apoe*$^{-/-}$ mouse strain (*Cth*$^{-/-}$ *Apoe*$^{-/-}$ mice) produced a phenotype of elevated plasma cholesterol following exposure to an atherogenic diet (Mani *et al.*, 2013). Consistent with their higher cholesterol, *Cth*$^{-/-}$*Apoe*$^{-/-}$ mice developed fatty streak lesions earlier than *Apoe*$^{-/-}$ mice, and this effect was reversed by NaHS administration (Mani *et al.*, 2013). Sulfide may also indirectly impact hepatic nutrient metabolism through its effect on hepatic artery vasorelaxation and thus liver perfusion (Fiorucci *et al.*, 2005; Distrutti *et al.*, 2008). The apparently beneficial effects of sulfide administration in multiple disease indications has led to a major drive towards development of targeted H_2S–donor molecules as a therapeutic approach (Whiteman *et al.*, 2011; Sestito *et al.*, 2017). However, an often-overlooked aspect of net sulfide exposure, key to the efficacy of therapeutic H_2S–donors, is that it is regulated through its oxidative disposal. Thus, endogenous sulfide exposure is actively limited to prevent mitochondrial respiratory toxicity (Reiffenstein, 1992; Tiranti *et al.*, 2009; Libiad *et al.*, 2018). Sulfide is rapidly oxidized (Hildebrandt and Grieshaber, 2008; Norris *et al.*, 2011) through the mitochondrial sulfide oxidation pathway (SOP), consisting of sulfide quinone oxidoreductase (SQOR), persulfide dioxygenase (ETHE1/PDO) and thiosulfate sulfurtransferase (TST, also known as rhodanese) (Hildebrandt and Grieshaber, 2008; Jackson, Melideo and Jorns, 2012; Libiad *et al.*, 2014). The liver is highly abundant in SOP enzymes, and is a major organ of whole body sulfide disposal (Norris *et al.*, 2011). Mice lacking the *Ethe1* gene (*Ethe1*$^{-/-}$ mice) die of fatal sulfide toxicity (Tiranti *et al.*, 2009), consistent with its critical role in sulfide oxidation and the severe pathological consequences of unchecked sulfide build-up in tissues. However, the importance of mitochondrial TST in the SOP *in vivo* remains obscure. In contrast to *Ethe1*$^{-/-}$ mice, *Tst*$^{-/-}$ mice were grossly normal despite exhibiting substantially elevated blood sulfide levels, as

implied by qualitative measures (Morton *et al.*, 2016). This revealed an important yet distinct role for TST in the SOP *in vivo*. Nevertheless, *Tst*$^{-/-}$ mice showed an apparently diabetogenic impairment of glucose tolerance (Morton *et al.*, 2016), consistent with the concept that increased sulfide promotes hepatic glucose production (Zhang *et al.*, 2013). As *Tst* deficiency represents a model of chronic but viable sulfide elevation, determining the molecular mechanisms driving their aberrant metabolic profile can provide important insights into the optimal range for therapeutic sulfide exposure, particularly in light of the current interest in developing mitochondrially–targeted sulfide–donors (Gero, Domokos Torregrossa *et al.*, 2016; Karwi, Bice and Baxter, 2018). To this end we sought to define the impact of *Tst* deficiency on the underlying molecular pathways that impact hepatic metabolism.

RESULTS

Tst$^{-/-}$ *mice exhibit increased hepatic gluconeogenesis and dyslipidaemia despite mild peripheral insulin sensitisation.*

TST *mRNA* expression is highest in the liver, http://biogps.org/#goto=genereport&id=22117; tissue hierarchy of expression was validated in our own mouse substrain (Figure S1A). We therefore hypothesised that liver TST deficiency was the principal driver of the impaired glucose tolerance previously observed in *Tst*$^{-/-}$ mice (Morton *et al.*, 2016). *Tst*$^{-/-}$ mice exhibited higher glucose levels than C57BL/6J controls in response to a pyruvate challenge, consistent with higher hepatic glucose production (Figure 1A). We next tested phosphoenolpyruvate carboxykinase (PEPCK) activity, a key enzyme of *de-novo* hepatic glucose synthesis, and found it was higher in liver homogenates from *Tst*$^{-/-}$ mice (Figure 1B). Next, we performed a 1 hour $^{13}C_3$-pyruvate metabolite–pulse incorporation experiment in isolated hepatocytes cultured in $^{12}C_3$-pyruvate–free medium. Hepatocytes from *Tst*$^{-/-}$ mice displayed ^{13}C labelling consistent with increased metabolism of pyruvate to oxaloacetate – a critical early step in gluconeogenesis. Specifically, aspartate, which is derived from pyruvate via oxaloacetate was significantly increased in the *Tst*$^{-/-}$ (Figure 1C). A trend towards higher $^{13}C_3$ malate, and lower $^{13}C_2$ acetyl–CoA was also observed (Figure S1B and S1C). $^{13}C_3$ Lactate was similar between genotypes, suggesting a similar activity of glycolytic disposal of pyruvate through lactate dehydrogenase (Figure S1B and S1C). Isotopologue distribution is shown in Fig S1C. Total pool sizes for all measured metabolites were similar between genotypes (Figure S1D). Although not a direct measure of glucose production, the data from *in vitro* hepatocytes suggested skewing of hepatocyte metabolism towards gluconeogenesis, and we therefore investigated this possibility by further means. Indeed, consistent with increased endogenous

glucose production in the *Tst*$^{-/-}$ mice, fasting plasma glucose was higher in *Tst*$^{-/-}$ mice relative to 6J mice during the pre-clamp 3-^{3}H glucose tracer infusion phase (60-90 minutes post tracer) of euglycemic, hyperinsulinemic (EH) clamp experiments (Figure 1D, Table S1A). Higher plasma glucose levels in *Tst*$^{-/-}$ mice under these conditions was not explained by lower glucose utilization in *Tst*$^{-/-}$ mice; glycogen synthesis and glycolysis were comparable between genotypes across 60–90 minutes (Table S1A). Glucose turnover – a derived parameter used to infer glucose production – was also comparable between genotypes (Table S1A). However, derivation of glucose turnover requires that glucose levels are stable during the period in which it is calculated. In our pre-clamp baseline period, a highly significant effect of time (Figure 1D) indicated that this assumption was not met, and thus true endogenous glucose production cannot be inferred from the glucose turnover parameter in this instance. Combined with the pyruvate tolerance, PEPCK activity and $^{13}C_3$-pyruvate pulse data, higher fasting glucose levels in the *Tst*$^{-/-}$ mice, given comparable glucose utilization, is most likely due to higher endogenous glucose production in the *Tst*$^{-/-}$ mice.

We next wished to explore whether the changes to glucose metabolism were driven by insulin resistance. Liver glycogen, a marker of long–term carbohydrate storage typically impaired with insulin resistance, was comparable between *Tst*$^{-/-}$ and C57BL/6J control mice (Figure S2A). Despite unchanged steady–state markers of hepatic insulin sensitivity, impaired glucose tolerance, previously described in the *Tst*$^{-/-}$ mice (Morton *et al.*, 2016), suggested that whole body, and usually hepatic, insulin–resistance was present. We investigated this using the euglycaemic clamp where, unexpectedly, we observed whole–body insulin sensitisation under these short–term steady–state conditions. During the clamp, when insulin was high, and blood glucose levels were maintained constant, the glucose infusion rate was comparable between genotypes (Table S1B). However, an increase in whole–body glucose uptake

(integral glucose) by tissues in the *Tst*$^{-/-}$ mice was apparent (Figure 1E, Table S1B), supporting increased peripheral insulin–sensitivity, with a directionally consistent trend for increased glucose uptake into several tissues. We confirmed this finding using standard insulin tolerance tests, where the glucose decrement in response to insulin was greater in *Tst*$^{-/-}$ mice (Figure 1F, Figure S2B). Together these data demonstrate a net increase in dynamic whole–body insulin sensitivity, despite increased hepatic glucose output in *Tst*$^{-/-}$ mice. Finally, we assessed whole–body glucose homeostasis with the EH–clamp method after chronic HFD feeding. Under these conditions, *Tst*$^{-/-}$ mice maintained increased hepatic glucose output (Figure 1D) but showed convergence of the insulin–sensitivity profile to that of the insulin-resistant C57BL/6J mice.

We also assessed whether *Tst* deficiency was associated with impaired lipid metabolism, another hallmark of diabetes. Fast protein liquid chromatography analysis of triglyceride levels and their lipoprotein distribution revealed significantly higher total plasma triglycerides in *Tst*$^{-/-}$ mice (Figure 1G). The higher triglyceride was selectively associated with an increased VLDL triglyceride fraction (Figure 1G), consistent with a dominant liver-driven impairment in lipid metabolism (Mason, 1998). Total and distinct lipoprotein fraction plasma cholesterol levels were similar between genotypes (Figure S2C and S2D), suggestive of a triglyceride–selective effect of *Tst* deficiency on hepatic lipid efflux. HFD significantly increased liver lipid content of C57BL/6J mice but did not further increase the elevated lipid levels in the liver of *Tst*$^{-/-}$ mice (Figure 1H-1I).

TST deficiency elicits compensatory hepatic sulfide disposal mechanisms that drive reduced global protein persulfidation.

192 A role for TST in the disposal of sulfide was suggested by its participation in the SOP
193 (Hildebrandt and Grieshaber, 2008; Libiad *et al.*, 2014) and supported *in vivo* by the
194 qualitatively higher blood sulfide of *Tst*$^{-/-}$ mice (Morton *et al.*, 2016), schematically shown in
195 Figure 2A. Here, we quantified circulating sulfide, showing approximately 10–fold elevation
196 in the blood and plasma of *Tst*$^{-/-}$ mice (Table 1A and 1B). Thiosulfate, an oxidised metabolite
197 of sulfide (Vitvitsky *et al.*, 2015, 2017) and a TST substrate (Banerjee *et al.*, 2015), was
198 approximately 20–fold higher in plasma (Table 1B), and profoundly higher (450–fold) in urine
199 (Table 1C) of *Tst*$^{-/-}$ mice compared to C57Bl/6J mice. Reduced glutathione (GSH) levels were
200 ~2–fold higher in the plasma of *Tst*$^{-/-}$ mice (Table 1B). To determine any direct hepatic
201 contribution to the elevated systemic sulfide *in vivo*, whole blood was sampled from the
202 inferior vena cava (IVC) (Table 1D). IVC sulfide levels tended to be higher in the *Tst*$^{-/-}$ mice,
203 but the magnitude of the increase (~3-fold) did not parallel that in trunk blood (~10-fold),
204 suggesting liver was not a major source of the elevated circulating sulfide. Surprisingly, liver
205 homogenate sulfide, thiosulfate, cysteine and GSH levels were similar between *Tst*$^{-/-}$ and
206 C57BL/6J mice (Table 1E). Further, cultured hepatocytes from *Tst*$^{-/-}$ and C57BL/6J mice
207 exhibited similar intracellular sulfide levels, as estimated using P3, a sulfide–selective
208 fluorescent probe (Singha *et al.*, 2015) (Table 1F). Mitochondrial sulfide levels in liver reported
209 by MitoA/MitoN (Arndt *et al.*, 2017) were similarly unchanged between genotypes (Table 1G).
210 The apparently unaltered hepatic steady-state sulfide levels, despite higher circulating
211 sulfide, suggested a profound homeostatic mechanism was invoked in the liver of *Tst*$^{-/-}$
212 mice. We assessed respiratory sulfide disposal (antimycin–sensitive) and found this was
213 markedly increased in hepatocytes from *Tst*$^{-/-}$ mice, whereas antimycin–insensitive sulfide
214 disposal was relatively reduced compared to hepatocytes from C57BL/6J mice (Table S2).
215 Isolated liver mitochondria from *Tst*$^{-/-}$ hepatocytes also exhibited a higher sulfide disposal

rate (Table S2). In addition, cysteine and GSH was excreted at higher levels from *Tst*$^{-/-}$ hepatocytes under basal conditions and after stimulation of sulfur amino acid metabolism by addition of methionine (Figure 2B and 2C). Consistent with higher GSH turnover, hepatocytes from *Tst*$^{-/-}$ mice showed resistance to exogenous H_2O_2–mediated mitochondrial ROS production (Figure S3). We next determined the global hepatic protein persulfidation profile, the major post–translational modification mediated by sulfide (Krishnan *et al.*, 2011; Kabil, Motl and Banerjee, 2014; Koike, Nishimoto and Ogasawara, 2017). Mass spectrometry analysis of maleimide–labelled liver peptides revealed a greater abundance of peptides with a lower persulfidation level (under-persulfidated) in the liver of *Tst*$^{-/-}$ mice (Figure 2D). We confirmed this using semi-quantitative western–blot analysis on pulled down maleimide–labelled proteins (Figure 2E). Gene Ontology (GO) analysis of under-persulfidated peptides (20 GO categories; Table 2) showed enrichment for "*FAD-binding*, *methyl transferase, peroxisome, acyl-CoA dehydrogenase activity and transaminase*". Over-persulfidated peptides (8 GO categories, Table 2) were predominantly "*Nicotinamide metabolism*". Pathway-specific peptide analysis showed a bias for over-persulfidation in gluconeogenesis proteins (Figure S4A) and a significantly higher magnitude of change (independent of direction of change) in persulfidation compared to global persulfidomic changes between C57BL/6J and *Tst*$^{-/-}$ mice (Figure S4B).

The hepatic proteome of Tst$^{-/-}$ *mice reveals a distinct molecular signature of altered sulfur and mitochondrial nutrient metabolism.*

To gain molecular insight into the mechanisms underlying the apparently diabetogenic phenotype in *Tst*$^{-/-}$ mice we compared hepatic proteomes of normal diet (ND)-fed mice. Kyoto Encyclopedia of Genes and Genomes (KEGG) analysis revealed 4 up–regulated

pathways in liver of *Tst*$^{-/-}$ mice related to amino acid metabolism, including sulfur amino acids, and sulfur metabolism (Table 3A). GO analysis revealed 95 significantly up–regulated categories in liver of *Tst*$^{-/-}$ mice (Table S3A). Among the top categories, 7 referred to amino acid metabolism and 1 referred to the organellar term '*mitochondrion*'. KEGG analysis revealed 27 down–regulated pathways in the liver of *Tst*$^{-/-}$ mice (Table 3B) including Phase 1 and 2 detoxification pathways (Cytochrome P450s, Glutathione and Glucuronidation) and '*Lysosome*', '*Protein processing in the Endoplasmic reticulum'* organellar terms. 213 GO terms were significantly down–regulated in *Tst*$^{-/-}$ mice (Table S4B). Among the most significant down–regulated terms were phase 2 detoxification *'glutathione binding'*, '*glutathione transferase activity'* and '*endoplasmic reticulum'* categories. We validated broadly consistent direction of change in a representative subset of proteins (Figures S5A and S5D). The most robust change we observed was increased MPST protein in whole liver (Figure S5A and S5D) and mitochondrial sub-fractions (Figure S5B and S5D). This change was remarkable as mRNA levels for *Mpst* were lower in *Tst*$^{-/-}$ mice (Figure S5C), likely as a result of loss of proximal *Mpst* promoter function; *Mpst* is a paralog of *Tst* (Nagahara, 2011) juxtaposed approximately 1kb from the *Tst* gene. Protein levels for other sulfide producing and disposal enzymes were comparable between genotypes (Table S4). A focussed comparison of canonical proteins in glucose and lipid metabolism pathways (Table S5) revealed four GO categories that were down–regulated in *Tst*$^{-/-}$ mice; '*Lipid metabolic process'*, '*fatty acid beta-oxidation'*, *'Acyl-CoA dehydrogenase activity' and 'Acyl-CoA hydrolase activity'* (Table S5). Canonical insulin–regulated proteins were largely comparable between genotypes (Table S6).

Hepatic protein expression in Tst$^{-/-}$ *mice is consistent with lower NRF2 activation*.

We performed a transcription factor binding site (TFBS) enrichment analysis in the promoters of proteins that were up–regulated in the liver of *Tst*$^{-/-}$ mice to look for potential hub transcriptional drivers of the proteome profile (Figure S6A). This revealed a statistically significant under-representation of TFBS for the sulfide–responsive (Yang *et al.*, 2013; Xie *et al.*, 2016) NRF2 transcription factor (Figure S6A). Consistent with reduced hepatic NRF2 activation, 10 out of 47 known NRF2-regulated proteins were lower in the liver of ND-fed *Tst*$^{-/-}$ mice compared to C57BL/6J (Figure S6B).

Proteome of TST deficiency versus HFD response in C57BL/6J mice reveals distinct regulation of lipid metabolism, sulfide metabolism and detoxification pathways.

We examined mechanistic commonalities between the diabetogenic hepatic phenotype of *Tst*$^{-/-}$ mice and that induced by the diabetogenic HFD–feeding regimen in C57BL/6J mice. Note, ND-fed *Tst*$^{-/-}$ mice were in a pre-existing diabetogenic state (Figure 1) that does not further worsen with HFD (Figure 1H-I, Table S1), suggesting gross phenotypic convergence of the two genotypes after HFD. We compared the identity and direction of change of the 188 proteins differentially expressed in ND-fed *Tst*$^{-/-}$ mice (versus ND-fed C57BL/6J mice; Figure 3A) to proteins that were differentially expressed in response to HFD in C57BL/6J mice (432 proteins; Figure 3A). There was a striking 67% overlap in individual proteins (126) in this comparison (Figure 3A). When we analysed these two protein signatures for directionally shared pathways, one up-regulated KEGG pathway *'Glycine, serine and threonine metabolism'* (Table S7A) and 12 down-regulated KEGG pathways, including *'drug metabolism'* and *'endoplasmic reticulum'* (Table S8B) were common to the liver of the ND-fed *Tst*$^{-/-}$ and HFD-fed C57BL/6J mice. Consistent with a pre-existing HFD–like proteome, the dynamic response to HFD in the liver of *Tst*$^{-/-}$ mice was muted, relative to that observed in C57BL6J mice (106

proteins, a 4–fold lower response; Figure 3B). Focussing on the sulfide pathway, MPST and SUOX were increased by HFD in C57BL/6J and *Tst*$^{-/-}$ mice (Table S8). The HFD–induced increase in MPST was less pronounced in the liver of *Tst*$^{-/-}$ mice, likely a reflection that it is already elevated in ND–fed *Tst*$^{-/-}$ mice. We then considered contrasting, rather than congruent, proteomic responses arising from TST deficiency versus HFD responses in C57BL/6J mice to illuminate potential novel pathways underlying the otherwise functionally similar diabetogenic hepatic *Tst*$^{-/-}$ phenotype. 5 KEGG pathways (Table S9A) and 4 GO terms (Table S9B) were oppositely regulated in this comparison. Strikingly, the GO terms were all related to lipid metabolism, which were up–regulated in the HFD response but down–regulated with TST deficiency (Table S9A-B). An organelle–focussed protein analysis showed shared up-regulation of mitochondrial and endoplasmic reticulum pathways between TST deficiency (Figure 3C upper row) and C57BL/6J HFD-responses (Figure 3C lower row), but a striking discordance in peroxisomal protein pathways (up-regulated by HFD, down-regulated with TST deficiency) and nuclear proteins (down-regulated by HFD, up-regulated with TST deficiency; Figure 3C).

The Tst$^{-/-}$ *liver proteome and persulfidome converge on transamination and lipid oxidation pathways.*

To assess whether conservation of changes at protein and post-translational modification levels can illuminate key regulatory hubs driving the hepatic phenotype we ran a congruence analysis of the proteome and persulfidome. We found that GO categories '*amino acid*', *'lipid metabolism*' and *'peroxisome*' were significantly regulated at both protein abundance and persulfidation levels in *Tst*$^{-/-}$ mice (Table 3C).

306 *$Tst^{-/-}$ hepatocytes exhibit elevated mitochondrial respiration and a defect in medium–chain*
307 *fatty acid oxidation.*

308 Enhanced respiratory sulfide disposal was found from *$Tst^{-/-}$* hepatocytes, and enrichment of
309 mitochondrial proteins was suggested from the liver proteome of the *$Tst^{-/-}$* mice (Table S4).
310 We therefore sought to determine if TST deficiency affected respiratory function and
311 substrate utilisation of the hepatocyte. Analysis of electron micrographs prepared from the
312 liver of ND-fed *$Tst^{-/-}$* mice and C57BL/6J controls showed morphologically normal
313 mitochondria (Figure 4A). Basal respiration, comprising ATP–linked and leak respiration, was
314 significantly higher in hepatocytes from *$Tst^{-/-}$* mice (Figure 4B–4D). Maximal hepatocyte
315 respiratory capacity and non–respiratory oxygen consumption was similar between
316 genotypes (Figures S7A and S7B). In line with phenotypic convergence following HFD,
317 hepatocyte respiration was comparable between genotypes from HFD-fed mice (Figures S7C-
318 S7H). A unique feature of the liver from *$Tst^{-/-}$* mice was a decrease in proteins and
319 persulfidation levels of proteins in lipid oxidation pathways. We therefore investigated
320 hepatocyte respiration of lipids. Using a low pyruvate (100 μM) medium to reveal respiratory
321 dependency on other substrates, we showed that CPT1A–mediated mitochondrial oxidation
322 of endogenous long chain fatty acids (LCFA; etomoxir-inhibited) was similar between
323 genotypes (Figure 4E). Next, we by–passed CPT1A–mediated LCFA transfer, and revealed a
324 marked deficit in respiration stimulated by the medium chain fatty acid octanoate in
325 hepatocytes from *$Tst^{-/-}$* mice (Figure 4F). A similar experiment adding back pyruvate
326 revealed comparable stimulation of respiration between genotypes (Figure S7I). In amino acid
327 free media, combined glutamine–, aspartate– and alanine–stimulated hepatocyte respiration
328 was comparable between genotypes (Figure S7J).

329

DISCUSSION

Elevated TST expression in adipose tissue was recently identified as a genetic mechanism driving metabolically protective leanness in mice (Morton *et al.*, 2016). Conversely, mice with genetic deletion of *Tst* (*Tst*$^{-/-}$ mice) exhibited impaired glucose tolerance (Morton *et al.*, 2016). However, *Tst*$^{-/-}$ mice had a subtle adipose tissue phenotype, suggesting a non-adipose origin for impaired glucose homeostasis. We found increased gluconeogenesis, steatosis and elevated plasma VLDL triglycerides consistent with a predominatly hepatic origin for the diabetogenic phenoptype. We cannot rule out a contribution of renal gluconeogenesis to the phenotype, and future work will address this limitation. Unexpectedly, and in spite of the markedly increased circulating sulfide levels (10-fold), steady-state sulfide level was normal in the liver of *Tst*$^{-/-}$ mice. Moreover, we found evidence for multiple mechanisms for increased hepatic sulfide disposal, reduced downstream sulfide signalling and associated underlying molecular links to an apparently diabetogenic phenotype. Our data suggest that the liver of *Tst*$^{-/-}$ mice has over-shot in its attempt to maximise hepatic sulfide removal, leading indirectly to detrimental metabolic consequences. This involves a combination of distinct compartmentalised cellular responses including increased respiratory sulfide disposal and export of cysteine and GSH. Notably, up-regulation of translation and recruitment of MPST to the mitochondria of *Tst*$^{-/-}$ mice is observed. This response, in face of reduced transcription of *Mpst*, suggests a powerful post-transcriptional cellular sulfide sensing mechanism. Interestingly, if MPST is compensating for TST–mediated sulfide disposal in this context, it implies a subversion of normal MPST function away from sulfide production (Módis *et al.*, 2013; Szabo *et al.*, 2014; Kimura *et al.*, 2017; Nagahara, 2018). Alternatively this is a response to a perceived lower sulfide environment. TST levels

were also elevated in the liver of *Mpst*$^{-/-}$ mice, providing further support for a reciprocal compensatory mechanism between these two enzymes (Nagahara *et al.*, 2019).

The unexpected finding of normal hepatic sulfide levels in the *Tst*$^{-/-}$ mice led us to discover that the metabolic phenotype we observed was driven by the very mechanisms invoked to maintain sulfide within a normal range rather than sulfide excess *per se*. Several observations were consistent with this. For example, the major amino acid pathways increased in the liver of *Tst*$^{-/-}$ mice were transaminases involved in metabolism of GSH that support increased export of sulfur equivalents as GSH (and cysteine). These same transaminases support gluconeogenesis by redirecting Krebs cycle intermediates (Rui, 2014; Qian *et al.*, 2015; Sookoian *et al.*, 2016). Re–programming of amino acid metabolism for sulfide disposal with knock–on effects to drive hepatic glucose production are suggested, rather than any change to amino acid–linked mitochondrial respiration in hepatocytes. This is supported by the shift in hepatocyte pyruvate metabolism towards aspartate. In addition, glutathione-S-transferases (GST) that inhibit gluconeogenesis (Ghosh Dastidar *et al.*, 2018) were lower in the liver of *Tst*$^{-/-}$ mice. Further, activation of NRF2, which represses gluconeogenesis (Slocum *et al.*, 2016) appears lower in liver of *Tst*$^{-/-}$ mice. The involvement of NRF2 in the *Tst*$^{-/-}$ liver phenotype is further supported by the phenotype of *Nrf2*$^{-/-}$ mice that similarly exhibited steatohepatitis in the absence of insulin resistance (Meakin *et al.*, 2014). However, we note that NRF2 signalling can be complex and dependent upon dietary context; *Nrf2*$^{-/-}$ mice showed improved glucose tolerance after a high fat diet (Zhang *et al.*, 2012) suggesting any contribution of a NRF2 signalling deficit in the liver of the *Tst*$^{-/-}$ mice changes upon high fat feeding. Beyond altered pyruvate flux, we also showed that the hepatocytes of *Tst*$^{-/-}$ mice exhibited defective lipid metabolism. Specifically, medium–chain fatty acid (MCFA) oxidation was impaired, associated with selective reduction of both protein and

377 persulfidation levels of lipid catabolic enzymes. This represents a mechanism linking altered
378 sulfide metabolism to lipid oxidation, hepatic lipid accumulation and dyslipidaemia.
379 Consistent with impaired MCFA oxidation defects as one driver of the phenotype, steatosis is
380 observed in medium–chain acyl-CoA dehydrogenase (*Mcad*)$^{-/-}$ mice (Tolwani *et al.*, 2005)
381 and dyslipidemia is found in MCADD deficient humans (Onkenhout *et al.*, 1995). The data we
382 present adds to a growing understanding of the link between sulfide regulating genes and
383 nutrient metabolism that has hitherto focussed on the enzymes of sulfide production.
384 Specifically, we provide support for the importance of the sulfide oxidising pathway as a
385 regulator of cellular sulfide exposure. Unexpectedly, the data reveal cellular mechanisms that
386 are engaged to homeostatically regulate sulfide disposal and that can impact upon cell
387 energetics and nutrient metabolism.
388 Our findings may have implications for potentially unexpected side effects of sulfide donor
389 therapeutics. In normal mice, *in vivo* sulfide administration for 4 weeks post–HFD partially
390 reversed hepatic lipid accumulation invoked by chronic (16 weeks) HFD (Wu *et al.*, 2015). No
391 evidence was provided for whether sulfide disposal mechanisms were altered (Wu *et al.*,
392 2015). This efficacious sub-chronic sulfide administration regimen contrasts with our genetic
393 model of chronic sulfide elevation as a driver of dysregulated metabolism and NAFLD. Clearly,
394 the normal mice in the Na_2S administration studies had a fully functional SOP, suggesting the
395 presence of TST is required to achieve the beneficial metabolic effects of Na_2S administration.
396 This is also consistent with the apparently low sulfide signalling status (evidenced by lower
397 persulfidation, NRF2 target protein abundance) in the liver of the *Tst*$^{-/-}$ mice. The benefits
398 of elevated sulfide cannot be realised perhaps because a major mediator of those effects is
399 missing and the alternate mechanisms invoked do not fully compensate (e.g. MPST), or
400 actively drive aberrant nutrient metabolism. Comparable studies of glucose and lipid

401 metabolism after manipulation of other sulfide regulating genes are limited. However in a
402 contrasting model of reduced sulfide production (*Cth*$^{-/-}$ mice), plasma triglycerides were
403 lowered (Mani *et al.*, 2013), opposite to what we observed with the *Tst*$^{-/-}$ mice. The hepatic
404 sulfide disposal status of the *Cth*$^{-/-}$ mouse model is unknown, but our findings predict a
405 suppression of the SOP to spare the limited endogenous sulfide produced. Intriguingly they
406 also predict a knock-on effect on nutrient homeostasis due to reduced metabolic demand of
407 the TST/SOP axis. A more direct model informing on the effects of impairment of the sulfide
408 disposal pathway is deficiency of the key mitochondrial SOP enzyme ETHE1. *Ethe1*$^{-/-}$ mice
409 suffer fatal sulfide toxicity (Tiranti *et al.*, 2009) and therefore comparable metabolic studies
410 are lacking. However, one notable observation is that *Ethe1*$^{-/-}$ mice have an apparently 10-
411 fold higher liver sulfide exposure than control mice (Tiranti *et al.*, 2009), in contrast to the
412 normalised hepatic sulfide levels of *Tst*$^{-/-}$ mice. Circulating sulfide levels were not reported
413 for comparison, but the presumably relatively lower systemic sulfide levels of *Tst*$^{-/-}$ mice
414 appear to have permitted an effective homeostatic sulfide disposal response in the liver to
415 avoid toxicity, albeit with a metabolic cost. Consequently, the liver of *Tst*$^{-/-}$ mice has a
416 distinct functional and proteomic profile to that of the *Ethe1*$^{-/-}$ mice. For example, in the
417 liver of *Tst*$^{-/-}$ and *Ethe1*$^{-/-}$ mice (Hildebrandt *et al.*, 2013), proteins of the glutathione–S–
418 transferase Mu type (GSTM) and peroxiredoxin (PRDX) families were altered, but sometimes
419 in the opposite direction or with alteration of distinct protein sub-classes. A notable
420 difference is also observed in amino acid metabolism. The liver of *Ethe1*$^{-/-}$ mice exhibited
421 increased expression of enzymes of branched chain amino acid metabolism (Hildebrandt *et*
422 *al.*, 2013), distinct from the predominantly glutathione–related amino acid pathways that are
423 increased in liver of *Tst*$^{-/-}$ mice. Beyond sulfide, TST may also have distinct cellular roles that
424 affect metabolism such as mitoribosomal synthesis, ROS attenuation and modulation of

mitochondrial iron-sulfur clusters (Bonomi *et al.*, 1977; Pagani and Galante, 1983; Nandi and Westley, 1998; Nandi, Horowitz and Westley, 2000; Smirnov *et al.*, 2010).

Given the pro-diabetogenic liver phenotype in *Tst*$^{-/-}$ mice, its was surprising that insulin signalling in the liver appeared normal and peripheral insulin sensitivity was increased. There are precedents for increased hepatic glucose production independent of insulin resistance, as found in the *Nrf2*$^{-/-}$ mice (Meakin *et al.*, 2014) and as driven by the transcription factor ChREBP (Uyeda and Repa, 2006; Kim *et al.*, 2016). There is also evidence to support insulin–sensitising effects of sulfide administration *in vivo* in mice and rats (Feng *et al.*, 2009; Geng *et al.*, 2013; Xue *et al.*, 2013), consistent with sulfide–mediated insulin–sensitisation of non-hepatic tissues in *Tst*$^{-/-}$ mice. Higher circulating GSH in *Tst*$^{-/-}$ mice may also promote peripheral insulin–sensitisation (Jain *et al.*, 2014; Lutchmansingh *et al.*, 2018). Clearly, the net balance of glucose production from the liver and its peripheral disposal remains abnormal in *Tst*$^{-/-}$ mice. Indeed, the baseline metabolic phenotype of *Tst*$^{-/-}$ mice resembles in many ways that of a normal mouse fed a HFD and we showed some overlapping pro-diabetogenic signatures between the liver proteome of *Tst*$^{-/-}$ mice and that of HFD-fed C57BL/6J mice. However, we also found distinct lipid metabolism and peroxisomal protein changes in *Tst*$^{-/-}$ mice. Unlike a HFD state, which is associated with dominant hepatic insulin resistance, the increased hepatic glucose production in ND-fed *Tst*$^{-/-}$ mice occurs despite normal hepatic insulin sensitivty. The significant changes in persulfidation of transaminase and gluconeogenesis proteins suggests coordinated cross–talk across metabolic pathways underlies this atypical metabolic phenotype.

Sulfide donor therapeutics were proposed as a clinical strategy for improving cardiovascular health (Szabó *et al.*, 2011; Whiteman *et al.*, 2011; Zhang *et al.*, 2018). Elevated endogenous sulfide was also implicated in the beneficial metabolic effects of caloric restriction (Miller *et*

449 *al.*, 2005; Hine *et al.*, 2015, 2017, 2018; Shimokawa *et al.*, 2015; Lee, Kaya and Gladyshev,
450 2016). Our results suggest that chronic sulfide elevation may have unintended detrimental
451 consequences, driving liver glucose production and fat accumulation to undesirable levels.
452 This caveat may be fortunately limited to cases where SOP proteins are compromised through
453 rare genetic effects – such as TST variants (Billaut-Laden *et al.*, 2006; Libiad, Sriraman and
454 Banerjee, 2015). More broadly, a number of drugs or supplements are known to increase
455 cyanide, which may dominantly inhibit TST activity and result in secondary sulfide
456 overexposure. These include nitroprusside (Morris *et al.*, 2017) and amygdalin (Bromley *et*
457 *al.*, 2005; O'brien, Quigg and Leong, 2005). Indeed, the TST metabolite thiosulfate is
458 commonly co-administered with nitroprusside to prevent cyanide toxicity (Curry, Carlton and
459 Raschke, 1997). Furthermore, dietary and environmental exposure to cyanogenic compounds
460 (Petrova, 2004), e.g. smoking (Vinnakota *et al.*, 2012) or cyanogenic diets (Kashala-Abotnes
461 *et al.*, 2019) may interfere with normal TST function and could lead to increased sensitivity to
462 sulfide therapeutics. In contrast, we have shown that administration of the TST substrate
463 thiosulfate can ameliorate diabetes (Morton *et al.*, 2016) further underlining the potential
464 utility of targeting the SOP in metabolic disease. As with all therapeutic strategies, a careful
465 cost-benefit analysis is required. A comparable case of relevance are the statins, one of the
466 most potent and widely used drugs to prevent atherosclerosis, which also carry a higher risk
467 for diabetes (Swerdlow *et al.*, 2015). The full impact of TST manipulation on opposing
468 metabolic pathways requires further study. Our current study sheds light on the underlying
469 hepatic mechanisms invoked for sulfide disposal that are relevant to current sulfide–donor
470 strategies and may inform on routes to reduce their potential metabolic side-effects.
471
472 **Limitations of the Study**

Whilst liver is the site of most (~60%) post-absorptive gluconeogenesis in normal animals within physiological fasting ranges, renal/small intestinal gluconeogenesis begins to substantially contribute to circulating glucose with prolonged fasting/starvation (Sasaki et al., 2017, Mutel *et al*., 2011, Mithieux *et al.,* 2003, Stumvoll 1998, Owen 1969). We cannot rule out a role for renal or intestinal gluconeogenesis in the diabetogenic phenotype of *Tst*$^{-/-}$ mice. This will be an important area of future work, although we note that liver TST is at least >3-fold that of kidney and small intestinal TST is very low (BioGPS, Figure S1A).

ACKNOWLEDGEMENTS

This work was funded by a Wellcome Trust New Investigator Award to NMM (100981/Z/13/Z) and Diabetes UK grant (17/0005697). RCH was funded by a Medical Research Council Discovery Award (MC-PC-15076). We would like to thank Professor Ken Olsen and Eric DeLeon (Notre Dame) for advice establishing sulfide measurement by probe.

AUTHOR CONTRIBUTIONS

N.M.M. and R.N.C conceived experiments. R.N.C., M.T.G.G, M. B.-L., A. M.-C., M.L., V.V., B.E., T. LeB., M.B., S.H., S.G.D., N.Z.M.H., C. Mc F., A.T., N. F., T.G., performed experiments. R.N.C., M. B.-L., P.F., V.V., T. LeB., N.Z.M.H., T.S., F.B., T.G., R.C.H., B.S., G.G., A.J.F., C.S., R.B. and N.M.M. analysed and interpreted data and commented on the manuscript. K.H.A., S.S. generated reagents. C.McM. and R.C.H. generated reagents. R.N.C. and N.M.M. wrote the manuscript.

Declaration of Interests

The authors have declared that no conflict of interest exists.

MAIN FIGURE TITLES AND LEGENDS

Figure 1. *Tst* deletion results in impaired glucose and lipid metabolism. (**A**) Plasma glucose over 120 minutes, following pyruvate (i.p., 1.5mg/g) administration in overnight fasted C57Bl/6J (black line, n = 9) and *Tst*$^{-/-}$ (red line, n = 8) normal diet-fed mice. (**B**) Extinction of NADH measured by absorbance at 340nm, coupled to PEPCK activity from liver homogenates taken from C57Bl/6J (white bar, n = 6) and *Tst*$^{-/-}$ (red bar, n = 6) normal diet-fed mice. (**C**) Production of ^{13}C (M+3) aspartate generated after a 1 hour pulse of 1mM 3-carbon labelled ^{13}C (M+3) pyruvate in ^{12}C pyruvate free media, expressed as a percentage of the total amount of detected metabolite, in primary hepatocytes from C57Bl/6J (white bars, n = 6) and *Tst*$^{-/-}$ (red bars, n = 5) normal diet-fed mice. (**D**) Blood glucose during the pre-clamp phase of the hyperinsulinemic, euglycemic clamp from C57Bl/6J (black lines), and *Tst*$^{-/-}$ (red lines) fed a control (ND, solid lines, n = 3, 6) or high fat diet (HFD, broken lines, n= 6, 7). (**E**) Mean integrated radioactive glucose (inversely related to whole body glucose uptake) during a hyperinsulinemic, euglycaemic clamp from normal diet fed C57Bl/6J control (white, n = 3), and *Tst*$^{-/-}$ (red, n = 6) mice. (**F**) Plasma glucose expressed as % of baseline glucose, over 120 minutes following insulin (i.p., 1mU/g) administration in 4 hour fasted C57Bl/6J (black line, n = 8) and *Tst*$^{-/-}$ (red line, n = 7) normal diet-fed mice. (**G**) HPLC quantified total and VLDL plasma triglyceride in 4 hour fasted C57Bl/6J (white bar, n = 6), and *Tst*$^{-/-}$ (red bar, n = 6) normal diet-fed mice. (**H**) Representative light microscopic images of fixed liver stained with Oil-Red O from normal diet-fed (ND) or high fat diet-fed (HFD) C57Bl/6J and *Tst*$^{-/-}$ mice. (**I**) Analysis of the area of red staining (Oil Red O) after thresholding, using Image J, from normal diet-fed (no pattern, n = 3-4/genotype) or high fat diet-fed (hatched pattern, n = 4-5/genotype) C57Bl/6J (white bars) and *Tst*$^{-/-}$ (red bars) mice. Data are represented as mean ±SEM. Significance was calculated using repeated measures ANOVA (**A**,**F**) 2-WAY ANOVA (**I**), 3-WAY repeated measures ANOVA (**D**) or unpaired two-tailed student's t-test (**B**,**C**,**E**,**G**) * $P < 0.05$, ** $P < 0.01$, *** $P < 0.001$, **** $P < 0.0001$. For (**D**) significant effects of time (****), diet (*) and genotype (*) were found. For (**F**) the analysis was performed on absolute glucose values and demonstrated a significant effect of time (****) and an interaction between time and genotype (*). T-tests revealed that the decrement of glucose from baseline at 30 and 60 minutes after insulin was greater in the *Tst*$^{-/-}$ (*). For (**I**) no main genotype effect was found, but a significant effect of diet (***), and an interaction (*) were found. Post Hoc analysis using Sidaks' multiple comparison test show an effect of diet on the 6J controls (***), whereas no effect of diet is found on the *Tst*$^{-/-}$. See also Fig S1, S2 and Table S1.

Figure 2. *Tst* deletion results in increased hepatic sulfur excretion and a reduction of protein persulfidation. (**A**) Schematic showing mammalian metabolism of hydrogen sulfide. The canonical production enzymes are shown in the cytosol; **MPST** (mercaptopyruvate suflur transferase), **CBS** (cystathionine beta synthase), and **CTH** (cystathionine gammalyase). Mitochondrial oxidation and disposal of hydrogen sulfide occurs through the 'sulfide oxidation pathway', through the actions of **SQOR** (sulfide quinone oxidoreductase), **ETHE1** (persulfide dioxygenase), **TST** (thiosulfate sulfurtransferase), and **SUOX** (sulphite oxidase). These seven enzymes are widely accepted as major contributors to intracellular sulfide (and other inorganic sulfur) metabolism. For simplicity, the diagram does not include sulfide production which can occur within the mitochondria, or disposal pathways in cytosol. The identity of oxidised sulfur species produced by **SQOR** remain disputed. The precise role of **TST** and other enzymes shown here remains under investigation. (**B**) Cysteine concentrations (MBB-HPLC) in the media incubated with primary hepatocytes in the presence (hatched pattern) or absence (no pattern) of 1mM methionine, from C57Bl/6J (white bars, n = 4/treatment) and *Tst*$^{-/-}$ (red bars, n = 4/treatment) mice. (**C**) Glutathione concentrations (MBB-HPLC) in the media incubated with primary hepatocytes in the presence (hatched pattern) or absence (no pattern) of 1mM methionine, from C57Bl/6J (white bars, n = 4/treatment) and *Tst*$^{-/-}$ (red bars, n = 4/treatment) mice. (**D**) Pie chart depicting the proportion of liver peptides that are significantly higher (82 peptides, purple space) or lower (311 peptides, yellow space), in their persulfidation rate in the *Tst*$^{-/-}$ (n = 3) relative to C57Bl/6J (n = 3) mice. (**E**) Total DTT-released cysteine-persulfidated liver

protein as measured by REVERT total protein stain following western blotting, normalised to the total input protein of the sample from *Tst*$^{-/-}$ (red bar, n = 4) and C57Bl/6J (white bar, n = 4) mice. Data with error bars are represented as mean ±SEM. Significance was calculated using 2-WAY ANOVA (**B**, **C**) or student's t-test (**E**), * P < 0.05, ** P < 0.01. For (**B**) and (**C**) the 2-WAY ANOVA reveals a main effect of genotype, indicated by * or ** on the histogram. A significant effect of methionine was also found for both (**B**) and (**C**) not indicated on the histogram. For (**D**) peptides were selected as being significant at a P-diff of 0.95 or greater. See also Fig S3 and Table S2.

Figure 3. *Tst* deletion engenders a high fat feeding–like hepatic proteome with a distinct organellar signature. (**A**) Venn diagram representing the number of proteins significantly different (at P < 0.01) between normal diet-fed *Tst*$^{-/-}$ and C57Bl/6J (Red circle), and the number of regulated proteins between high fat fed and normal diet-fed C57Bl/6J (Green circle). The overlap (brown) represents those proteins regulated in the same direction by both comparisons (n= 4/genotype). (**B**) Number of proteins significantly different (at p < 0.01) between 58% high fat and normal diet in either C57Bl/6J (white bar), or *Tst*$^{-/-}$ mice (Red bar), (n= 4/genotype). (**C**) Pie charts depicting the proportion of individual liver proteins that are upregulated (Blue space) compared to downregulated (yellow space) after GO term categorisation according to subcellular location. Upper row; normal diet-fed *Tst*$^{-/-}$ relative to normal diet-fed C57Bl/6J. Lower row, high fat-fed C57Bl/6J relative to normal diet-fed C57Bl/6J. See also Table 3, Figure S5, S6.

Figure 4. *Tst* deletion results in increased hepatocyte respiration but impaired medium–chain fat respiration. (**A**) Electron microscope images of liver, visualising mitochondria from normal diet-fed C57Bl/6J (n = 4) or *Tst*$^{-/-}$ (n = 4) mice. (**B**) Seahorse trace representing the mean oxygen consumption rate (OCR), normalised to protein, by hepatocytes from normal diet-fed C57Bl/6J (n = 6) or *Tst*$^{-/-}$ (n = 6) mice during a mitochondrial stress test. (**C**) Respiratory OCR linked to ATP production (oligomycin sensitive) by hepatocytes from normal diet-fed C57Bl/6J (n = 6) or *Tst*$^{-/-}$ (n = 6) mice, calculated from Figure 4B. (**D**) Respiratory OCR relating to proton leak (oligomycin insensitive) by hepatocytes from normal diet-fed C57Bl/6J (n = 6) or *Tst*$^{-/-}$ (n = 6) mice, calculated from Figure 4B. (**E**) Reduction of maximal uncoupled respiration following inhibition of long chain fatty acid mitochondrial import using etomoxir (8 µM), from normal diet-fed C57Bl/6J (n = 4) or *Tst*$^{-/-}$ (n = 4) mice. (**F**) Stimulation of maximal uncoupled respiration following addition of medium chain fatty acid octanoate (250 µM), from normal diet-fed C57Bl/6J (n = 4) or *Tst*$^{-/-}$ (n = 4) mice. Data are represented as mean ±SEM. Significance was calculated using an unpaired two tailed, student's t-test (**C**, **D**, **E**, **F**), * P < 0.05. See also Figure S7.

MAIN TABLES, TITLES AND LEGENDS

Table 1. Sulfur species in blood, urine, tissue and cells

	C57Bl/6J	*Tst*$^{-/-}$	*Tst*$^{-/-}$/6J ratio	Significance
A Trunk Blood (Micromolar)				
MBB-S (Sulfide)	2.28 +/- 0.43	22.18 +/- 0.85	9.73	****
MBB-SSO3 (Thiosulfate)	n.d.	6.25 +/- 3.17	n.c.	**ns**
B Trunk Plasma (Micromolar)				
MBB-S (Sulfide)	1.88 +/- 0.64	24.50 +/- 2.02	13.03	****
MBB-SSO3 (Thiosulfate)	3.99 +/- 0.99	80.29 +/- 13.6	20.12	**
MBB-GSH (reduced Glutathione)	48.0 +/- 1.15	86.25 +/- 6.27	1.80	***
C Urine (Micromoles/creatine/24hrs)				
MBB-SSO3 (Thiosulfate)	4.99 +/- 2.6	2374 +/- 319	475.75	****
D Inferior Vena Cava (Micromolar)				
MBB-S (Sulfide)	1.22 +/- 0.20	3.58 +/- 0.87	2.93	**ns (0.08)**
MBB-SSO3 (Thiosulfate)	6.58 +/- 4.51	88.3 +/- 13.0	13.42	*
E Liver (µmoles/kg wet liver)				
MBB-S (Sulfide)	13 +/- 1	17 +/- 3	1.31	**ns**
MBB-SSO3 (Thiosulfate)	4 +/- 1	15 +/- 7	3.75	**ns**
DNFB-GSH (reduced Glutathione)	6470 +/- 380	6850 +/- 30	1.04	**ns**
DNFB-Cysteine (Cysteine)	82 +/- 13	67 +/- 11	0.82	**ns**
F Sulfide P3 fluorescence (A510nm/protein)				
Hepatocyte	7.22 +/- 1.00	7.89 +/- 0.80	1.09	**ns**
G Mitochondrial sulfide (MitoA)				
Liver	0.78 +/- 0.16	1.14 +/- 0.45	1.46	**ns**
*** P < 0.05, ** P < 0.01, *** P < 0.001 **** P < 0.0001**				

Table 1. *Tst* deletion results in altered sulfur metabolites in blood and liver. (**A**) Sulfide dibimane, thiosulfate-MBB, measured by fluorescence detection following HPLC, from whole blood taken from trunk blood of ND-fed C57Bl/6J (n = 4) and *Tst*$^{-/-}$ (n = 4) mice. (**B**) Sulfide dibimane, thiosulfate-MBB, and rGSH-MBB, measured by fluorescence detection following HPLC, from EDTA-Plasma of ND-fed C57Bl/6J (n = 4) and *Tst*$^{-/-}$ (n = 4) mice. (**C**) Thiosulfate-MBB corrected for creatinine from 24 hour urine samples, taken from ND-fed C57Bl6/J (n = 4) and *Tst*$^{-/-}$ (n = 5) mice. (**D**) Sulfide dibimane, and thiosulfate-MBB, from whole blood taken from the inferior vena cava downstream of the hepatic vein of ND-fed C57Bl/6J (n = 3) and *Tst*$^{-/-}$ (n = 3) mice. (**E**) Sulfide dibimane, thiosulfate-MBB, rGSH-MBB, and cysteine-MBB from whole liver (n=4/genotype) of ND-fed C57Bl/6J (n = 4) and *Tst*$^{-/-}$ (n = 4) mice. (**F**) Fluorescence from cultured hepatocytes following incubation with P3 (sulfide reactive probe) from ND-fed C57Bl/6J (n = 4) and *Tst*$^{-/-}$ (n = 4) mice. (**G**) Ratio of Mito N/MitoA from the liver of ND-fed C57Bl/6J (n = 5) and *Tst*$^{-/-}$ (n = 5) mice. Data are represented as mean ±SEM. Significance was calculated using unpaired two-tailed student's t-test. * P < 0.05, ** P < 0.01, *** P < 0.001, **** P < 0.0001

Table 2. GO Terms persulfidation rate (*Tst*$^{-/-}$ vs C57Bl/6J liver, ND-fed)			
GO-ID	**Name**	**Direction (*Tst*$^{-/-}$ vs 6J)**	**Genes**
	GO terms Identified by log fold change		
0050660	FAD binding	Decreased	12
0008168	Methyltransferase activity	Decreased	9
0016741	Transferase activity, transferring one-carbon groups	Decreased	9
0008565	Protein transporter activity	Decreased	8
0008238	Exopeptidase activity	Decreased	7
0005777	Peroxisome	Decreased	7
0042579	Microbody	Decreased	7
0003995	Acyl-CoA dehydrogenase activity	Decreased	6
0008483	Transaminase activity	Decreased	6
0016769	Transferase activity, transferring nitrogenous groups	Decreased	6
0008757	S-adenosylmethionine-dependent methyltransferase activity	Decreased	6
0016655	Oxidoreductase activity, acting on NADH/NADPH, quinone	Decreased	5
0004177	Aminopeptidase activity	Decreased	5
0000059	Protein import into nucleus, docking	Decreased	3
0005643	Nuclear pore	Decreased	3
0031965	Nuclear membrane	Decreased	3
0044453	Nuclear membrane part	Decreased	3
0046930	Pore complex	Decreased	3
0015629	Actin cytoskeleton	Decreased	3
0016652	Oxidoreductase activity, NADH/NADPH, NAD/NADP acceptor	Decreased	3
0050662	Coenzyme binding	Increased	5
0016651	Oxidoreductase activity, NADH/NADPH,	Increased	5
0003954	NADH dehydrogenase activity	Increased	4
0008137	NADH dehydrogenase (ubiquinone) activity	Increased	4
0050136	NADH dehydrogenase (quinone) activity	Increased	4
0006739	NADP metabolism	Increased	3
0006769	Nicotinamide metabolism	Increased	3
0006733	Oxidoreduction coenzyme metabolism	Increased	3

Table 2. Tst deletion results in differential persulfidation rate of liver proteins. Significant GO terms represented by peptides with different persulfidation rates in the ND-fed *Tst*$^{-/-}$ liver relative to C57Bl/6J. '**Direction**' indicates whether the persulfidation is decreased or increased in *Tst*$^{-/-}$ relative to C57Bl/6J. '**Genes**' indicates the number of genes in the *Tst*$^{-/-}$ that represent the changes driving the GO term.

614

Table 3. KEGG and GO changes (*Tst*$^{-/-}$ vs C57Bl/6J liver, ND-fed)

Entry	Name	Genes	Significance
A. KEGG pathways Increased in ND *Tst*$^{-/-}$ liver			
00250	Alanine, aspartate and glutamate metabolism	6	***
00260	Glycine, serine and threonine metabolism	5	**
00270	Cysteine and methionine metabolism	4	*
04122	Sulfur relay system	2	*
B. KEGG Pathways Reduced in ND *Tst*$^{-/-}$ liver			
00980	Metabolism of xenobiotics by cytochrome P450	12	****
00982	Drug metabolism – cytochrome P450	12	****
05204	Chemical carcinogenesis	12	****
00480	Glutathione metabolism	8	***
00040	Pentose and glucoronate interconversions	5	**
04142	Lysosome	6	**
04390	Hippo signalling pathway	4	**
00500	Starch and sucrose metabolism	5	**
05215	Prostate cancer	3	**
04024	cAMP signalling pathway	4	*
04141	Protein processing in ER	9	*
05211	Renal cell carcinoma	3	*
00830	Retinol metabolism	6	*
00053	Ascorbate and aldarate metabolism	4	*
00860	Porphyrin and chlorophyll metabolism	4	*
04722	Neurotrophin signalling pathway	3	*
04670	Leukocyte transendothelial migration	4	*
04010	MAPK signalling pathway	4	*
04720	Long-term potentiation	2	*
04914	Progesterone-mediated oocyte maturation	2	*
04062	Chemokine signalling pathway	3	*
04110	Cell cycle	3	*
04015	Rap1 signaling pathway	4	*
00983	Drug metabolism - other enzymes	5	*
04918	Thyroid hormone synthesis	3	*
04612	Antigen processing and presentation	3	*
05203	Viral carcinogenesis	5	*

C. GO terms common to Persulfidome and Proteome in ND *Tst*$^{-/-}$ liver

GO-ID	Name of GO term	Persulfidation (*Tst*$^{-/-}$ vs 6J)	Abundance (*Tst*$^{-/-}$ vs 6J)
0008483	Transaminase activity	Decreased	Increased
0016769	Transferase activity, transferring nitrogenous groups	Decreased	Increased
0003995	Acyl-CoA dehydrogenase activity	Decreased	Decreased
0005777	Peroxisome	Decreased	Decreased
0042579	Microbody	Decreased	Decreased

*** P < 0.05, ** P < 0.01, *** P < 0.001 **** P < 0.0001**

615
616

Table 3. Protein abundance and persulfidation in ND-fed *Tst*$^{-/-}$ liver. (**A**) Significant KEGG pathway terms represented by proteins that are more abundant in the liver of ND-fed *Tst*$^{-/-}$ compared with ND-fed C57Bl/6J. (**B**) Significant KEGG pathway terms represented by proteins that are less abundant in the liver of ND-fed *Tst*$^{-/-}$compared with ND-fed C57Bl/6J. '**Genes**' indicates the number of genes in the *Tst*$^{-/-}$ that represent the changes driving the KEGG pathway. (**C**) GO terms that are significantly regulated at *both* the level of cysteine persulfidation and protein abundance in liver of ND-fed *Tst*$^{-/-}$ compared with ND-fed C57Bl/6J.

STAR ★ METHODS

RESOURCE AVAILABILITY

Lead contact

Further information and requests for resources and reagents should be directed to and will be fulfilled by the lead contact, Nicholas M. Morton (nik.morton@ed.ac.uk).

Materials availability

No other new unique reagents were generated for the production of the data in this paper.

Data and code availability

Proteomics and persulfidomics root data from the iTraq and persulfidated peptide mass spectrometry experiments have been deposited to the ProteomeXchange Consortium via the PRIDE (Perez-Riverol et al., 2019) partner repository with the dataset identifier PXD028909.

This paper does not report original code.

Any additional information required to reanalyse the data reported in this paper is available from the lead contact upon request.

EXPERIMENTAL MODEL AND SUBJECT DETAILS

Experimental animals. All experiments were performed according to guidelines set out by the ethical committees of The University of Edinburgh and Physiogenex S.A.S, Prologue Biotech, Labège, FRANCE. Experiments were carried out within the framework of the Animals (Scientific Procedures) Act (1986) of the United Kingdom Home Office or related laws from the European Union (France). In all studies, animals within genotype cohorts were randomly assigned to diet or intervention groups. All animals were maintained in standard housing with 12 hour light and 12 hour dark cycles (7 a.m. to 7 p.m.) and *ad libitum* access to the appropriate diet. For in vivo experiments (pyruvate tolerance test, insulin tolerance test,

671 euglycaemic clamps), operators and animal handlers were blinded to the data, which was
672 generated by a second individual who was blinded to the treatment regimen until the code
673 was broken. All of the studies used male mice housed in cages of 3-6 individual littermates
674 until intervention. The mice for this study originated from C57Bl/6N *Tst*$^{-/-}$ mice (Morton *et*
675 *al.*, 2016) backcrossed onto the C57Bl/6J genetic background for >10 generations. Mice were
676 placed onto high fat diet D12331, (58% calories from fat, Research Diets, New Brunswick,
677 USA) from between 6-8 weeks of age, for 6-7 weeks prior to testing, and compared to mice
678 maintained on standard low fat diets, RM1 or D12383 (low-fat high-cornstarch, Research
679 Diets, New Brunswick, USA).
680 ***Hepatocyte preparations.*** Mice were killed by CO_2 asphyxiation, followed by cervical
681 dislocation. The chest cavity was opened, the portal vein was cut and the thoracic vena cava
682 was cannulated via the right atrium. The liver was perfused with (37°C) perfusion media (140
683 mM NaCl, 2.6 mM KCl, 0.28 mM Na_2HPO_4, 5 mM glucose, 10 mM HEPES, 0.5 mM EGTA, pH
684 7.4), 6 mls/min for 10 min. The liver was then perfused with digestion media (perfusion media,
685 without EGTA, including 5 mM $CaCl_2$, and 100 U/ml collagenase type 1) for 5-7 min. Finally,
686 the liver was perfused with perfusion media for a further 10 min. Cells were extruded from
687 liver into DMEM medium (DMEM, 5.5 mM glucose, 10% FCS, 7 mM glutamine, and
688 penicillin/streptomycin antibiotics), and then passed through a 40 micron filter. Cells were
689 spun twice and washed with medium, at 500 rpm (47 g) for 5 min. Cells were spun through a
690 50% Percoll pH 8.5-9.5/DMEM solution at 1000 rpm (190 g) for 15 min to remove dead cells
691 and non hepatocytic liver cell types. Hepatocytes collected in the pellet fractions were
692 resuspended in medium and spun twice with washing at 500 rpm (47 g) 5 minutes. Yields and
693 viability were assessed by counting using a haemocytometer, and proportion of trypan blue
694 exclusion respectively. Yields ranged from between $2 \times 10^6 - 1.5 \times 10^7$ viable cells, and viability

was above 85%. Unless otherwise stated, hepatocytes were seeded onto collagen coated tissue culture plastic (collagen from rat tails, Sigma), and maintained in DMEM with 5.5 mM glucose, 10% FCS, 7 mM glutamine, and antibiotics).

METHOD DETAILS

Pyruvate tolerance test. Blood glucose was measured from 16 hour fasted mice before (0 time) and following bolus sodium pyruvate administration (i.p. 1.5 mg/g bodyweight). Blood was collected following tail venesection at 0, 15, 30, 60 and 120 minutes after injection. Glucose was measured from blood using a Glucometer (*OneTouch*, Lifescan, Milpitas, USA or *Accu-Chek*, Performa nano, Roche).

PEPCK activity assay. Activity of phosphoenolpyruvate carboxykinase was measured from cytosol samples obtained from frozen liver. Samples were homogenised in 250 mM sucrose, 5 mM HEPES, pH 7.4. and centrifuged at 4°C, 12,000 rpm (17,390 g) for 15 min. Supernatants were ultracentrifuged at 4° C, 60,000 rpm (289,000 g) for 30 min. Activity of PEPCK from cytosolic fractions was inferred in this assay from NADH extinction, linked to the conversion of phosphoenol pyruvate into oxaloacetate in the presence of carbonate, dGDP and $MnCl_2$, and the subsequent conversion of oxaloacetate into malate by adding malate dehydrogenase. Baseline measurements at 340 nM (NADH) were taken for 20 min before adding phosphoenol pyruvate, and the reaction proper was initiated with dGDP. The reaction was then measured for a further 40 min.

^{13}C Pyruvate metabolite tracing. After overnight culture on collagen coated 6-well tissue culture plates, hepatocytes were incubated with 1 mM $^{13}C_3$ labelled pyruvate in serum free DMEM for 60 min. Metabolites were extracted by washing individual wells with ice-cold PBS

and addition of cold extraction buffer (50% methanol, 30% acetonitrile, 20% water solution at -20°C or lower). Extracts were clarified and stored at -80°C until required. LC-MS was carried out using a 100 mm x 4.6 mm ZIC-pHILIC column (Merck-Millipore) using a Thermo Ultimate 3000 HPLC inline with a Q Exactive mass spectrometer. A 32 min gradient was developed over the column from 10% buffer A (20 mM ammonium carbonate), 90% buffer B (acetonitrile) to 95% buffer A, 5% buffer B. 10 µl of metabolite extract was applied to the column equilibrated in 5% buffer A, 95% buffer B. Q Exactive data were acquired with polarity switching and standard ESI source and spectrometer settings were applied (typical scan range 75-1050). Metabolites were identified based upon m/z values and retention time matching to standards.

Plasma lipid analysis. Mice were fasted with free access to water for 4 hours prior to cull by decapitation or pentobarbital euthanasia. Trunk blood (decapitation) was collected directly into Sarstedt Microvette CB 300 K2E EGTA containing plasma sample tubes (Sarstedt, Nümbrecht, Germany). Venous blood from the abdominal vena cava (post euthanisation) was collected into a BD Plastipak 1 ml syringe (BD, Madrid, Spain). This was then transferred to Sarstedt EGTA containing sample tubes for centrifugation. Blood samples obtained by either method were centrifuged at 20^{o}C and 5000 rpm (2655 g) for 5 min to obtain plasma samples. Plasma samples were analysed for cholesterol and triglyceride content by as previously described (Peters *et al.*, 1997). Briefly, samples were subjected to gel filtration chromatography using an integrated Alliance HPLC separations module (e2695, Waters, Milford, US) to separate lipoproteins based on size. Effluent was immediately and continuously mixed with either triglyceride (Infinity Triglyceride, Thermo Scientific, Loughborough, UK) or cholesterol (Infinity Cholesterol, Thermo Scientific, Loughborough, UK) enzymatic colourmetric detection kits at the correct conditions for reaction (as specified in

manufacturer's guidance). The optical density was then recorded using a spectrophotometer at the appropriate wavelength and the signal turned into a continuous trace i.e. a lipid profile. By identification of the lipoprotein peaks (based on their time of emergence from the chromatograph) the concentration for each could be calculated.

Oil Red-O lipid analysis of liver. 5 μm cryostat cut frozen sections of liver were collected onto Superfrost slides (Thermo), and rinsed with 60% isopropanol. Slides were incubated in freshly prepared staining solution (2.1 mg/ml Oil Red O in 40% isopropanol/water) for 10 – 30 min and rinsed with 60% isopropanol. Slides for representative images were counterstained for nuclei in haematoxylin (Harris) for 1 minute. For image analysis, slides were not counterstained. All slides were then rinsed in running tap water for 2 min, before mounting. Sections were captured using an AxioScan Z1 slide scanner at ×20 magnification and analysis of the proportional area of Oil Red O staining (area of stain/unit area of section) was performed using ImageJ software (National Institutes of Health), assessed by a blinded assessor.

Liver Glycogen measurement. Frozen liver samples (between 30-90 mg) were heated to 100°C in an Eppendorf tube with 0.3 mls of 30% KOH for 30 min with vigorous shaking at 10-min intervals. Samples were heated for a further 2-3 min after addition of 0.1 ml 1M Na_2SO_4 and 0.8 ml ethanol. Samples were then centrifuged at 4°C at 1011 g for 5 minutes. The supernatant was removed, and the pellet resuspended in distilled H_2O before 0.1 ml 1M Na_2SO_4 and 0.8 ml ethanol were again added, and samples boiled at 100°C for 5 min before centrifugation. This was repeated a final time to wash the sample. The pellet was resuspended in a 10 mg/ml (~1200 U/ml) amyloglucosidase enzyme in 0.3 M sodium acetate (pH 4.8). Samples were then incubated at 50°C for 2 hours. Quantification of samples was then performed using a standard hexokinase based glucose assay (Glucose (HK) Assay Kit, Sigma,

GAHK20). The assay was performed following manufacturer's instructions and values calculated by extrapolation from a standard curve after measuring absorbance using a plate spectrophotometer (Molecular Devices OPTImax microplate reader and software, Molecular Devices, Wokingham, UK).

Western blotting for protein abundance. Frozen liver samples (stored -80°C) from mice were homogenized in protein lysis buffer (50 mM Tris, 270 mM sucrose, 50 mM NaF, 1 mM EDTA, 1 mM EGTA, 1% Triton X-100, 10 mM B-glycerophosphate, 5 mM Na Pyrophosphate, 1 mM orthovanadate, 0.1% β-Mercaptoethanol, 1 tablet protease inhibitor cocktail inhibitor, pH 7.4, all Sigma Aldritch). Samples were then centrifuged at 13,200 rpm (18500 g) for 15 min at 4°C and the supernatants aliquoted and stored at -80°C. Protein samples were loaded onto 10% acrylamide/bis-acrylamide gels (30% acrylamide, Sigma Aldritch) and separated by electrophoresis. A coloured molecular weight marker was also run on all gels (Full range rainbow molecular weight markers, GE Healthcare). Gels were transferred overnight using a Bio Rad wet transfer system onto Amersham Hybond – P membranes (GE Healthcare). After transfer, for normalisation of specific targets to total protein, membranes were stained using the REVERT total protein stain (LICOR), according to manufacturers' instruction. Following stain and wash, lanes of each sample were analysed using a LI-COR Odyssey scanner (700nm channel). For blots using a house keeping protein for normalisation, the total protein stain was not performed, and membranes were transferred directly to blocking. All membranes were blocked in Tris buffered saline with 0.01% tween (TBST, containing 5% skimmed milk powder (Marvel skimmed milk powder) for 1 hour and then rinsed in TBST. Blocked membranes were then incubated with the appropriate primary antibody in TBST containing 5% BSA (Sigma Aldritch) overnight at 4°C. Following three 5 min washes with TBST, secondary antibody incubation for all blots was with an appropriate green or red fluorescent antibody,

incubated at room temperature for 2 hours in TBST containing 5% BSA. Membranes were washed three times in TBST then scanned using the LI-COR Odyssey scanner. Odyssey software (LI-COR Biosciences) was used to quantify band intensity. For normalization to a house keeping protein, the individual band intensity of B-actin was used for each sample. Primary antibodies used were; TST, Rabbit, GeneTex, GTX114858, MPST, Rabbit, Abcam, Ab224043, GOT1, Rabbit, Abcam, ab170950, GSTT1, Rabbit, Proteintech, 15838-1-AP, MAT1A, Rabbit, Abcam, ab129176, BHMT Rabbit, Proteintech, 15965-1-AP, CSAD, Rabbit, Abcam, ab91016, PPCS Rabbit, Atlas Antibodies, HPA031361. Secondary antibodies used were; IRDye800CW Goat anti-Rabbit, Li-Cor, 926-32211, IRDye 680RD Donkey anti-Mouse, Li-Cor, 926-68072. For normalisation B-Actin, Mouse, Abcam, ab8226 was used for whole tissue, and Cox IV (mitochondrial loading control), Abcam, ab16056 was used for mitochondrial fractions.

***Insulin tolerance test*.** Male C57BL/6J or *Tst*$^{-/-}$ mice were maintained on standard chow (RM1). Mice were fasted for 4 hours prior to injection i.p. of insulin (1 mU/g bodyweight, NovoRapid 100U/ml, Novo Nordisk). Tail venesection blood samples were taken prior to, and 15, 30, 60 and 120 minutes post injection. Blood glucose was measured from samples using a Glucometer (Accu-Check, Performa Nano, Roche). Blood glucose was plotted across time to evaluate net glucose accumulation in blood.

Euglycemic hyperinsulinemic clamps. Male C57BL/6J or *Tst*$^{-/-}$ mice were maintained on standard diet (RM1 (E) 801492, SDS) or high fat diet for 6 weeks (58% fat, D12331, Research Diets). Prior to performing the hyperinsulinemic euglycemic clamp an indwelling catheter was placed into the femoral vein under isoflurane anesthesia, sealed under the back skin, and glued onto the top of the skull. Clamps were performed 5-6 days after recovery from catheterization. Mice were fasted 6 hours prior to a basal blood sample was taken for glucose

and insulin. Mice then received a bolus of D-[3-3H] glucose (30 µCi) and perfused with 3H-glucose (30 µCi/kg/min at 2 µl/min) for 210 min (which covers the basal phase and hyperinsulinemic clamp). At steady state (60 min after start of perfusion), 5 µl of blood was collected and glycemia measured from tail tip every 10 min over 30 min for ^{3}H-radioactivity analysis for determination of whole body glucose turnover glycolysis and glycogen synthesis rate in the basal state. 90 min after start of perfusion, the hyperinsulinemic clamp starts by co-perfusion with insulin 8 mU/kg/min for the clamped phase over 120 min. Blood glucose was assessed every 10 minutes, and glucose infusion adjusted until steady state blood glucose (120 mg/dl +/- 10 mg/dl) was achieved. 5 µl of blood was collected from, tail tip every 10 min for ^{3}H- radioactivity analysis. At 150 min after the start of perfusion, a bolus of ^{14}C-2-deoxyglucose (25 µCi) was perfused to evaluate tissue specific uptake. At the end of the perfusion (210 min), blood is collected from the retro-orbital sinus to measure plasma insulin and mice sacrificed by i.v. injection of pentobarbital and cervical dislocation. Tissues (Inguinal WAT, Epididymal WAT, Soleus muscle, Extensor digitorum longus muscle, Vastus lateralis muscle, Tibialis anterior muscle, Heart apex, Liver) were removed by dissection and flash frozen in liquid nitrogen (stored -80°C until measured). Tracers were used to calculate various aspects of glucose metabolism (Altszuler *et al.*, 1956; Carter and Morton, 2016). Parameters measured or calculated include body weight, glucose infusion rate, whole body turnover, hepatic glucose production, whole body glycolytic rate, whole body glycogen synthesis rate, and tissue glucose utilization.

MBB derivatization of whole blood and plasma. Whole blood was taken after cull of mice, from trunk (following decapitation), or portal vein (following CO_2 euthanasia). EDTA-plasma was obtained from trunk blood following decapitation and collected onto ice. Blood for plasma was centrifuged within 15 min of collection for 5 min at 5000 rpm (2655 g) at 4°C.

Blood and plasma samples (15-50 µl) were derivatized with monobromobimane by addition of 200 µL of 80 mM EPPS (4-(2-Hydroxyethyl)-1-piperazine propanesulfonic acid, 8 mM DTPA (diethylenetriaminepentaacetic acid) pH 8.0, 50% acetonitrile, 2.3 mM monobromobimane. Reaction vials were capped tightly and vortexed for 1 minute and incubated protected from light at room temperature for 30 min. 1 mL ethyl acetate was added, the tube capped and vortexed for 1 min and incubated protected from light for 10 min. The reaction vials were centrifuged at 1800 rpm (350 g) for 7 min to separate aqueous and organic layers. The organic layer was collected from each extraction, transferred to a 1.5 mL brown glass vial and the solvent was evaporated completely under a nitrogen stream. Acetonitrile (200 µL) was added to each vial, and the solvent was again evaporated to remove any traces of ethyl acetate. Dried MBB-derivatives were stored at -20°C until analysed.

Fluorometric quantification of MBB-sulfur species. MBB-sulfur species (sulfide, thiosulfate, reduced glutathione, and cysteine) in samples was quantified by HPLC separation and detection with a fluorescence detector. The dried MBB derivatives were re-suspended in 50 µL of Buffer A (10 mM tetrabutylammonium phosphate aqueous, 10% methanol, 45 mM acetic acid adjusted to pH 3.4). The entire sample was transferred to an HPLC autosampler vial with a 200 µL glass sample insert, and the vial was closed with a penetrable cap. 20 µL of the sample was injected onto a C8 reverse-phase column (LiChrospher 60 RP-select B 5 µm 4.0 × 125 mm LiChroCART 125-4, Merck KGaA) and a guard column (LiChroCART 10-2, Superspher 60 RP-select B cartridge) on an Ultimate 3000 UHPLC+ focused system (Thermo Scientific). MBB derivatives were eluted with a linear gradient from 10% buffer B (10 mM tetrabutylammonium phosphate in methanol, 10% water, 45 mM acetic acid) to 100% buffer B over 30 min. The eluent was analysed by fluorescence (λex = 380 nm, λem = 480 nm).

Sulfur metabolite analysis from liver. Livers from mice were removed promptly following decapitation (within 2 min), and frozen on powdered dry ice. Frozen tissue was pulverized and derivatized with either 2,4-dinitrofluorobenzene for detecting GSH or monobromobimane for detecting sulfide and thiosulfate as described previously (Mosharov, Cranford and Banerjee, 2000; Vitvitsky *et al.*, 2006, 2015).

P3 fluorescence detection of sulfide in hepatocytes. Hepatocytes were seeded in glass bottomed, collagen coated wells (0.75 cm^2, 12,500 hepatocytes per well) and cultured in DMEM with 5.5 mM glucose, 10% FCS, 4 mM glutamax or 7 mM glutamine, and antibiotics overnight. P3 H_2S reactive probe (Singha *et al.*, 2015) was added to wells at 10 µM in serum free DMEM for 30 min, prior to gentle washing with Krebs phosphate buffered saline (pH 7.4). Plates were measured using the TECAN fluorescence plate reader, following excitation at 375 nm and detection at 510 nm. No-cell control wells were used for subtracting from the cell containing values. Corrected fluorescence emission data was normalised to protein as estimated by sulforhodamine dye. Briefly, after the run cells were fixed with 10% trichloroacetic acid overnight at 4°C. Cells were washed 9 times with tap water, and air dried. Cells were incubated with 200 µl of 0.4% Sulforhodamine dye/1% acetic acid for 1 hour at room temperature. Stain was removed, and washed 4 times with 1% acetic acid, and then air dried. Stain was dissolved in 200 µl of 10 mM Tris pH 10.5 for 30 min, and 100 µl was measured by colorimetric absorbance spectroscopy at 540 nm. After subtracting a baseline absorbance from blank controls, the absorbance was used to normalise the fluorescence data from each well.

Quantification of hydrogen sulfide levels using MitoA in vivo exomarker. MitoA and MitoN were quantified in mouse blood using LC-MS/MS. Mice received a tail vein IV injection of 50 nM MitoA in 0.9% saline (100 µL). MitoA was given 1.5 hr to distribute into mitochondria.

886 Mice were culled by decapitation 90 minutes after administration. Liver was excised and flash
887 frozen in liquid nitrogen. MitoA and MitoN were extracted from tissue by homogenization of
888 liver (50 mg) enriched with 5 pg d15-MitoN (95% ACN, 210 µL) which was used as an internal
889 standard (IS). Homogenates were centrifuged (16,000 g, 10 min, RT) and the supernatant was
890 transferred to a clean tube and stored on ice. The pellet was re-extracted (95% CAN, 210 µL),
891 spun down again (16,000 g, 10 min, rT) and the supernatants were combined and incubated
892 at 4^{o}C for 30 mins. Calibration standards comprise MitoA and MitoN standards ranging from
893 0.01 to 10 pg in 500 µL 95% ACN. 500 µL of the supernatants and calibration standards were
894 loaded onto an ISOLUTE PLD+ protein and phospholipid removal plate (Biotage, Sweden).
895 Samples and standards were pulled through the plate under vacuum into a 2 mL deep-well
896 96-well plate. Wells were dried completely at 40^{o}C under N_2 and resuspended in 100 uL 20%
897 ACN, 0.1% FA. The plate was shaken at (250 rpm, 20 min) to ensure reconstitution. Liquid
898 chromatography-Mass Spectrometry was performed on an I-class Acquity LC system-Xevo
899 TQS triple quadrupole mass spectrometer (Waters, Warrington, UK). Samples were kept at
900 10^{o}C and injected onto an Acquity UPLC BEH C18 column fitted with a 0.2 µm filter (1 x 50
901 mm, 1.7 µm, Waters). Chromatographic separation of MitoA and MitoN was achieved using
902 mobile phase A composition: water:ACN, (95:5, 0.1% FA), mobile phase B: ACN:water (90:10,
903 0.1% FA). LC mobile phases were infused at 200 µL/min using the gradient: 0– 0.3 min, 5% B;
904 0.3–3 min, 5–100% B; 3– 4 min, 100% B, 4.0– 4.10, 100–5% B; 4.10– 4.60 min, 5% B. MS/MS
905 analysis was performed under positive ion mode (Source spray voltage, 3.2 kV; cone voltage,
906 125 V; ion source temperature, 100 °C). Curtain and collision gas were nitrogen and argon,
907 respectively. Analytes were detected by multiple reaction monitoring (MRM). MitoA
908 undergoes neutral loss of N2 to a nitrene (precursor ion). For quantification the following
909 transitions were used: MitoA, *m/z* 437.2 →183.1; MitoN, *m/z* 439.2 → 120.0; d15-MitoN,

454.2 → 177.1 m/z. MassLynx 4.1 software was used to integrate the peak area of the analytes MitoA, MitoN and the d15-MitoN internal standard. Response was calculated by normalizing sample peak areas to the IS peak area. By comparison of sample responses to calibration standard responses the mass of each analyte in the tissue sample was calculated. The mass of analyte was normalised to the mass of tissue homogenizer and MitoN/MitoA ratio was calculated.

Preparation of hepatic mitochondria. Fresh liver was taken from mice, and homogenised in 250 mM sucrose, 10 mM HEPES, 1 mM EGTA. 0.5% fatty acid free bovine serum albumin (BSA) pH 7.4 at 4°C, with seven passes of a loose glass Dounce homogeniser (Type A). Homogenates were centrifuged in glass tubes at 2900 rpm (1000 g) for 10 min in a pre-chilled 4°C Beckman centrifuge (JA-20 Fixed angle rotor). The supernatant was then centrifuged in glass tubes at 8500 rpm (8700 g) for 10 min at 4°C. The supernatant was aspirated and any visible lipid was carefully removed from the sides of the tubes. The pellet was washed with 5 ml of mIR-05 buffer (0.5 mM EGTA, 3 mM $MgCl_2$, 20 mM taurine, 10 mM KH_2PO_4, 20 mM HEPES, 110 mM sucrose, 1 mg/ml fatty acid free BSA, pH 7.2), and centrifuged at 8500 rpm (8700 g) for 10 min at 4°C. After aspiration and removal of visible lipid, the pellet was suspended in 1ml of mIR-05 buffer and kept on ice until used. All measurements were taken within two hours of preparation. Protein concentration was determined using the DC-Protein Assay (BioRad) as per manufacturers instruction.

Amperometric analysis of sulfide disposal. Hepatocytes were prepared as described, and kept at room temperature in DMEM with 5.5 mM glucose, 10% FCS, 4 mM glutamax or 7 mM glutamine, and antibiotics at a concentration of 4×10^6 per ml. Mitochondria were prepared as described, and maintained on ice in mIR-05 buffer until use. All samples were analysed within 4 hours of preparation. Sulfide ($H_2S_{(g)}$) was measured (with and without samples) in a

2ml volume plastic chamber, to which an amperometric sensor was inserted, sealed with a rubber O-ring. Voltage measurements from the sensor (linear relationship to $H_2S_{(g)}$ concentration) were recorded using a TBR4100 Gas radical analyser (World Precision Instruments). A gas permeable membrane covered the sensor, and the outer glass sensor compartment was filled with H_2S detection fluid (World Precision Instruments). All measurements of $H_2S_{(g)}$ from standards and samples were recorded as voltage by the amperometric sensor at ambient temperature. Mitochondrial measurements (and standards) were taken in serum free mIR-05 buffer. Hepatocyte measurements (and standards) were taken in serum-free, bicarbonate-free DMEM, buffered with 25 mM HEPES (pH 7.4), with 5 mM glucose, 2 mM glutamax and 2 mM pyruvate. Sulfide was added to buffer in the form of Na_2S, predicted to equilibriate according to its Pka at this pH to about 1/3 of sulfide as $H_2S_{(g)}$ 2/3 as HS^-. The probes selectivity to $H_2S_{(g)}$ (vs HS^-) was confirmed with standards by demonstrating predicted signal amplification to a maximum following acidification of media to pH < 5 (approx. 100% $H_2S_{(g)}$/0% HS^-), and signal compression to a minimum following alkalinisation of standard to pH > 10 (Approx 0% $H_2S_{(g)}$/100% HS^-/S^{2-}). A final re-acidification recovered the signal to near maximal levels. Standard curves for calculating experimental measurements were prepared using freshly made Na_2S solutions ranging from 0.25 – 20 µM (corresponding to approximately 170 nm – 6.7 µM $H_2S_{(g)}$). $H_2S_{(g)}$ disposal was measured by recording the extrapolated $H_2S_{(g)}$ concentration after 10 min incubation with samples. A baseline without sample was taken for 5 min, and then after sample addition (400,000 hepatocytes, or 1.6 – 2.0 mg of mitochondrial prep), another 5 min baseline with sample was taken. In all experiments, no detectable increase in signal (limit of detection 0.25 µM Na_2S) was observed during incubation of hepatocyte or mitochondrial samples from either genotype. Following addition of 10 µM Na_2S the (voltage) signal was recorded over a period

of 10 min. Disposal rates were calculated after subtraction of a baseline disposal rate in media alone, over a 10 min period, performed each day of experimentation. Sample disposal rates were in the range of 5-20 higher than baseline disposal rate confirming good signal to noise. To determine the rate of disposal that is dependent upon respiration, a fresh aliquot of the same sample was prepared as before, but 5 min after addition of sample to chamber, Antimycin A (2.5 µM, dose titrated) was added. After a further 5 minutes, 10 µM Na_2S was added and a disposal rate (after subtraction to sample free baseline rate) was again calculated. The respiratory (Antimycin sensitive/complex III dependent) sulfide disposal rate of samples was calculated as the difference between the nieve sample rate and the Antimycin inhibited rate. After each measurement, the sample was removed, and centrifuged to collect cells or mitochondria for a final protein assessment (DC-Protein Assay, Bio-Rad) for the purposes of normalisation.

Mitochondrial ROS (MitoSOX) measurement in H_2O_2 treated hepatocytes. Hepatocytes were seeded overnight onto 96-well collagen coated plates. Cells were exposed to a range of concentrations of H_2O_2 (0.125 - 8 µM) for 2 hours. Following 3 washes with PBS, cells were incubated with MitoSOX Red mitochondrial superoxide indicator (Thermo Fisher) for 10 mins prior to three further washes. Measurement of fluorescence was carried out in a fluorescence detector plate reader (TECAN), using 510 nm for excitation and 580 nm for emission detection. Data from each well was normalised to sulfurhodamine dye protein stain.

Persulfidation Mass Spec and GO term analysis. Livers from mice were removed promptly following decapitation (within 2 min), and snap frozen in liquid nitrogen. The persulfide proteome analysis using the BTA method was conducted as described previously (Gao *et al.*, 2015). Briefly, 100-150 mg of frozen liver tissue was pulverized and lysed on ice in RIPA buffer (100 mM Tris, pH 7.5, 150 mM NaCl, 2mM EDTA, 1% Triton X-100, 25 mM deoxycholic acid, 2

tablets/ 100 ml of cOmplete™, Mini, EDTA-free Protease Inhibitor Cocktail (Roche)). The lysates were centrifuged at 14,000 g for 10 min at 4°C and protein concentrations were determined using the Bradford reagent (BioRad). Supernatant containing 6 mg of protein was incubated with 100 µM NEM-biotin (Pierce) for 60 min at room temperature after which the proteins were precipitated with cold acetone (1:4 v/v) for 1 h at -20°C, followed by a centrifugation at 14,000 g for 10 min at 4°C. The precipitated protein was re-suspended in a denaturing buffer containing 7 M urea, 1% SDS, 150 mM NaCl, 100 mM Tris, pH 7.5. Then, the samples were diluted 10-fold with trypsin reaction buffer (1 mM $CaCl_2$, 100 mM Tris pH 7.5) and incubated overnight with sequencing grade modified trypsin (1:50 trypsin:protein) (Promega) at 30 °C. The digestion products were mixed with streptavidin-agarose beads (ThermoScientific) and incubated at 4° overnight, followed by ten washes with the wash buffer (0.1 % SDS, 100 mM Tris, pH 7.5, 600 mM NaCl, 1 mM EDTA, 1% Triton X-100). The streptavidin-agarose bound peptides were incubated with elution buffer (100 mM Tris, pH 7.5, 150 mM NaCl, 1 mM EDTA, 30 mM DTT) for 1 hr at room temperature. Persulfidated peptides were eluted by centrifugation and derivatized with 40 mM iodoacetamide for 2 hrs at room temperature in the dark. The samples were then passed through a desalting column (Pierce). LC-MS/MS analysis was carried out using an LTQ-Orbitrap Elite mass spectrometer (Thermo-Fisher) coupled to an Ultimate 3000 high-performance liquid chromatography system. The alkylated peptides were loaded onto a 75 µm desalting column, C18 reverse phase resin (Dionex), and eluted onto a Dionex 15 cm x 75 µm id Acclaim Pepmap C18, 2 µm, 100 Å reverse-phase chromatography column using a gradient of 2–80% buffer B (5% water, 95% acetonitrile, 0.1% formic acid) in buffer A (0.1% formic acid). The peptides were eluted onto the mass spectrometer at a flow rate of 300 nl/min and the spray voltage was set to 1.9 kV.

GO enrichment analysis. In order to identify differentially persulfidated proteins between the C57Bl/6J and *Tst*$^{-/-}$ samples, we compared the abundances of persulfidated fragments in appropriately treated mass spectrometry data sets to the estimated overall abundance of the corresponding parent proteins in standard label-free quantitation experiments. For each observed persulfidated fragment in each experimental replicate, we calculated the persulfidation rate as the $\log_2$ ratio of the count of that persulfidated fragment to the median count of that fragment across all experimental replicates. The observed counts for the *Tst*$^{-/-}$ replicates were additionally scaled (prior to log transformation) by the ratio of abundances of the parent protein between the C57Bl/6J and *Tst*$^{-/-}$ cells to normalize for differential protein abundance across conditions. For each peptide we then assigned an approximate average $\log_2$ fold change in persulfidation rate between the C57Bl/6J and *Tst*$^{-/-}$ conditions. If a persulfidated peptide was identified in at least two biological replicates of one condition and none in the other, we assigned a $\log_2$ fold change of +/- 5.0 as placeholder values indicating a high confidence change; peptides with only one observation in one condition and none in the other were omitted from our analysis. Having thus obtained estimates for the magnitude of changes in persulfidation rate of each detectable peptide, we then performed gene ontology term enrichment analysis using the estimated $\log_2$ fold changes. We consolidated the peptide-level data to protein-level data by taking the largest magnitude change in persulfidation levels across all peptides from a given protein, and then used the iPAGE program [http://dx.doi.org/10.1016/j.molcel.2009.11.016] to identify GO terms with significant mutual information with the profile of persulfidation rates. Arguments to iPAGE were "—max_p=0.1 –minr=0.3 –ebins=9 –exptype=continuous", indicated that the data were discretized into nine equally populated bins prior to analysis, and that default hypergeometric p-value and information content thresholds were relaxed to maximize sensitivity.

Focussed analysis of persulfidation in gluconeogenesis proteins. The gluconeogenesis pathway was selected for a focussed analysis of the persulfidation rate of all cysteine sites detected in the mass spectrometry data as described above. All peptides from proteins present in the persulfidation data set used for GO enrichment analysis, that are defined by the GO term gluconeogenesis (GO 0006094) were included, these were Pgk1, Gpi1, Fbp1 and Tpi1 (22 peptides). The $\log_2$ rate ratio of persulfidation (*Tst*$^{-/-}$ /6J) of all of these 22 peptides was compared first to the entire mass spectrometry dataset for $\log_2$ rate ratio of persulfidation (1245 peptides after removal of ambiguous peptides, peptides with a P-diff of 0, and the 22 gluconeogenesis peptides). A Mann-Whitney non parametric T-test was used to detect significance. A second analysis was performed with the gluconeogenesis pathway. For this analysis, all $\log_2$ rate ratio's were given a positive sign to indicate the magnitude of change in the *Tst*$^{-/-}$ relative to 6J, independent to the direction of change. A Mann-Whitney non parametric T-test was then performed to determine if the magnitude of change in persulfidation in the gluconeogenesis pathway was significantly higher than that of the overall the data set.

Persulfidation labelling and western blotting from frozen liver. 80-120 mg of frozen liver samples were homogenized on ice using a 2 ml glass Dounce homogenizer (Kimble), in 500 µl buffer (7 M urea, 100 mM Tris pH 7.5, 150 mM NaCl, 1 mM EDTA, 1% Triton X-100, 1% deoxycholic acid; supplemented with cOmplete Protease Inhibitor Cocktail (Roche)). Initial disruption of tissue was achieved with three passes, using the loose (Type A) pestle, and after 5 min incubation on ice; complete homogenization was achieved with 9 passes using the tight fit (Type B) pestle. Homogenates were centrifuged at 5000 rpm (2655 g) for 5 min at 4°C. Protein concentrations of supernatants were determined using the *DC* BCA protein assay (Bio-Rad). Protein (6 mg) from each sample, was made up to 1 ml with phosphate buffered saline

(pH 8.0). Freshly prepared EZ-link Maleimide PEG Biotin EZ-linker (Thermo Fisher 21902BID), was added to samples to 100 µM, and incubated for 1 hour at room temperature with gentle mixing. Excess maleimide linker was removed from samples by acetone precipitation (3 volumes) at -20°C for 1 h, followed by centrifugation at 12000 rpm (17390 g) for 10 min at 4°C. Protein pellets were washed with ice-cold acetone and then dissolved in 250 µl of 50 mM Tris pH 8.0, 100 mM NaCl, 1 mM EDTA, 1 % SDS. To each sample, 750 µl of RIPA buffer (100 mM Tris pH 7.5, 150 mM NaCl, 1 mM EDTA, 1% Triton X-100, 1% deoxycholic acid) was then added. An aliquot (20 µl) was taken from each sample for estimation of total input protein for normalization (described below). The remainder of the samples were split into duplicates and incubated with gentle mixing, overnight at 4°C with 320 µl of pre-washed streptavidin agarose beads (Thermo Fisher 20347). Beads were washed 10 times with 0.8 ml washing buffer (30 mM Tris pH 7.5, 600 mM NaCl, 1 mM EDTA, 1% Triton X-100, 0.1% SDS), followed by one wash with phosphate buffered saline (pH 7.4). Beads were then centrifuged for 1 min at 1000 rpm (106 g) to dry. Elution of the duplicate samples for western blot analysis was performed by adding 300 µl of elution buffer (30 mM Tris pH 7.5, 150 mM NaCl). For each sample pair, one duplicate was eluted in buffer supplemented with 10 mM DTT and the other without DTT. The beads were incubated with the elution buffer for 1 hour at RT; and centrifuged for 1 min at 1000 rpm (106 g) to collect the eluate. Each eluted sample was concentrated to 20 ul using an Ultra-0.5 Centrifugal Filter Device, 10 K cut-off (Amicon), as per the manufacturer's instructions. Eluted samples, and input protein samples were loaded in their entirety onto SDS PAGE gels and transferred overnight at 4°C by Western blotting onto PVDF membrane. Total protein from each lane on the membrane was estimated after staining with REVERT total protein stain (LICOR) according to the manufacturer's instructions. Briefly, following overnight transfer and after rinsing the blot with water, the membranes were incubated with

1078 REVERT total protein stain for 5 min, and rinsed twice with wash solution. Blots were then
1079 imaged in the 700 nm channel with an Odyssey imaging system (LICOR). Each lane was
1080 measured for its total integrated fluorescence intensity to obtain an estimate of the total
1081 protein in each lane. Measurements from no-DTT eluted sample lanes were subtracted from
1082 DTT eluted sample lanes. Similar fluorescence measurements of input total protein lanes
1083 were used to normalise the eluted sample measurements, and this was used as a measure of
1084 relative protein-persulfidation rate.
1085 ***Mass spec analysis of liver protein.*** *Sample preparation; Tst*$^{-/-}$ and wild type (C57Bl/6J)
1086 mouse strains were fed either high-fat (58% fat) or normal (low fat) diet. Livers from mice
1087 were removed following decapitation, and snap frozen in liquid nitrogen. Four biological
1088 replicates from the 4 conditions were used to isolated proteins and performed protein
1089 quantitation using iTRAQ 8plex. Liver tissue was homogenized using 1 ml of 8 M urea with
1090 HEPES buffer pH 8.0. The protein concentration was determined using the Bio-Rad RC DC
1091 protein assay kit (Bio-Rad, Hercules, CA, USA). One hundred micro grams of protein from each
1092 of the samples were reduced with THP (Tris(hydroxypropyl)phosphine), alkylated with MMTS
1093 (methyl methanethiosulfonate) in 500 mM triethylammonium bicarbonate (TEAB, pH 8.5),
1094 trypsin digested and subsequently label with iTRAQ 8plex accordingly to the manufacturer's
1095 instructions. *Electrostatic Repulsion-Hydrophilic Interaction Chromatography (ERLIC) Peptide*
1096 *fractionation;* Peptide fractionation was performed using a pH gradient. Labeled peptides
1097 were dissolved in 100 µL of buffer A (100 mM formic acid, 25% acetonitrile, pH 3.0), followed
1098 by fractionation in a 2.6 × 200 mm, 5 µm, 200 Å PolySulfoethyl A column (Poly LC Inc.,
1099 Columbia, MD), using an Ultimate 3000 UHPLC+ focused (Thermo-Fisher Scientific) system,
1100 operating at a flow rate of 0.2 ml/min. Twenty minutes of isocratic buffer A were followed by
1101 a linear gradient from 0% to 100% buffer B (100 mM ammonium formate, 25% acetonitrile,

pH 6.0) over 20 min and then a final linear gradient from 0% to 100% buffer C (600 mM ammonium acetate, 25% acetonitrile, pH 6.0) over 10 min. A total of 22 fractions (1-min intervals) were collected. All fractions were lyophilized and stored at -20 °C. *Nanoflow Liquid Chromatography Tandem Mass Spectrometry;* NanoLC MS/MS analysis was performed using an on-line system consisting of a nano-pump UltiMate™ 3000 UHPLC binary HPLC system (Dionex, ThermoFisher) coupled with Q-Exactive mass spectrometer (ThermoFisher, San Jose, CA. iTRAQ-labeled peptides were resuspended in 2% ACN, 0.1% formic acid (20 µL) and 6 µL injected into a pre-column 300 µm×5 mm (Acclaim PepMap, 5 µm particle size). After loading, peptides were eluted to a capillary column 75 µm×50 cm (Acclaim Pepmap, 3 µm particle size). Peptides were eluted into the MS, at a flow rate of 300 nL/min, using a 90 min gradient from 0% to 35% mobile phase B. Mobile phase A was 2.5% acetonitrile with 0.1% formic acid in H_2O and mobile phase B was 90% acetonitrile with 0.025% trifluoroacetic acid and 0.1% formic acid. The mass spectrometer was operated in data-dependent mode, with a single MS scan in the orbitrap (400-2000 m/z at 70 000 resolution at 200 m/z in profile mode); automatic gain control (AGC) was set to accumulate 4×10^5 ions, with a maximum injection time of 50 ms. MS/MS scans were performed in the orbitrap at 17 500 resolution. Ions selected for MS/MS scan were fragmented using higher energy collision dissociation (HCD) at normalized collision energy of 38% with an isolation window of 0.7 m/z. MS2 spectra were acquired with a fixed first m/z of 100. The intensity threshold for fragmentation was set to 50 000 and included charge states 2+ to 7+. A dynamic exclusion of 60 s was applied with a mass tolerance of 10 ppm. *Data Analysis;* Raw files were converted to MGF files and searched against the mouse UniProt database (81033 sequences, released on March 2014) using MASCOT Version 2.4 (Matrix Science Ltd, UK). Search parameters were peptide mass tolerance of 10 ppm, and MS/MS tolerance of 0.05 amu allowing 2 missed cleavage. iTRAQ8plex (N-term) and

iTRAQ8plex (K) were set as fixed modification, and acetyl (Protein N-term), Methylthio (C) and Oxidation (M) were allowed as variable modification. Peptide assignments with ion score cut-off of 20 and a significance threshold of ρ <0.05 were exported to Excel for further analysis. Data are available from the ProteomeXchange with identifier PXD028909.

GO and KEGG enrichment analysis of proteome data. The data generated from the initial mass spectrometric analysis of iTRAQ labelled peptides from the 16 liver samples was analysed by FIOS. A total of 16 samples were QC analysed using the arrayQualityMetrics Bioconductor package to identify sub-standard and/or outlier samples. No samples were identified as outliers. All samples passed the manual and automated quality control based on three metrics (MAplot, Boxplot and Heatmap). The exploratory analysis using PCA showed that the samples clustered perfectly into four groups based on the factor Group (representing four genotype-diet combinations). The first PC captures the main source of variation in the dataset and is showing a separation of the samples based on diet, where high-fat diet and control diet samples separate. The second PC shows a separation between genotypes (Tst KO and WT). The hierarchical clustering and PCA plot both show a clear separation based on the iTRAQ labels. This is expected as the iTRAQ labels are confounded with the Groups. While the observed separation of the samples into groups is most likely due to the underlying biological differences, any technical variations (potentially introduced during the wet lab processing) could be masked. The log2 ratio data were subsequently normalised within arrays using loess, followed by normalisation between samples using the Gquantile method. A total of 4 single and/or multi-factor comparisons, using statistical approaches, were performed. The contrast "Tst KO vs WT mice (High-fat diet)" was analysed at a cut-off (unadjusted) p-value < 0.01. Due to the known bias in fold-change magnitudes of the iTRAQ technology, no fold-change cut-off was applied to the significant differentially abundant proteins. With this threshold 551

proteins were differentially abundant in at least one of the comparisons. The contrast "High-fat diet vs Control diet (WT)" had the most DAPs (432) while the contrast " *Tst*$^{-/-}$ vs 6J mice (High-fat diet)" had the least DAPs (83). Noticeably, the TST protein showed the strongest down-regulation for both of the contrasts comparing *Tst*$^{-/-}$ to 6J mice, consistent with gene deficiency and the fold change compression effect of iTRAQ. The full dataset (4,322 identified proteins) was filtered to remove proteins having less than two detected peptides (on average across all 16 samples); leaving 1,654 proteins for downstream analysis. Exploratory analysis using principal component analysis (PCA) showed that the dataset separated into four distinct groups based on the genotype-diet combinations along the two first principal components (PCs). These 1,654 proteins were used for enrichment analysis for GO terms and KEGG pathways. Individual proteins were considered of interest if they were found significantly different ($P < 0.01$) between selected pairwise comparisons. The four comparisons were *Tst*$^{-/-}$ normal diet vs C57Bl/6J normal diet, C57Bl/6J high fat diet vs C57Bl/6J normal diet, *Tst*$^{-/-}$ high fat diet vs *Tst*$^{-/-}$ normal diet, and *Tst*$^{-/-}$ high fat diet vs C57B/6J high fat diet. Normalised mean abundance of proteins was expressed as Log2 fold change ratios for each comparison.

Transcription factor enrichment analysis. 43 up-regulated proteins were selected for analysis of their promoter sequences (selected on basis of P-value < 0.05; adjusted for comparison of diet and genotype). 67 control proteins were selected from the proteome data on the basis of their equivalence of abundance between C57Bl/6J and *Tst*$^{-/-}$. We used a QIAGEN hosted/SABiosciences mouse database (sabiosciences.com) of promoter located transcription factor binding sites. 34 transcription factors were chosen to analyse, based on either their a-priori prevalence in the promoter of *Tst*$^{-/-}$ up-regulated proteins (present in the promoters of more than 50% of the up-regulated proteins) or on their links to either

sulfide or nutrient metabolism. The proportion of genes containing a TFBS was calculated for the up-regulated set (43) and the control set (67). The ratio of up-regulated to control was then calculated. The number of genes with and without the presence of the TFBS were analysed for establishing statistical difference (Up-regulated vs Control), using a Fisher Exact test ($P < 0.05$).

NRF2 target identification and proteome analysis. NRF2 target genes of the mouse liver were compiled from the following reviews (Cuadrado *et al.,* 2019, Tonelli *et al.*, 2018, Rooney *et al.*, 2018, Walsh *et al*., 2014). 106 genes were identified as target genes (upregulated at mRNA or protein level following NRF2 activation). 47 of these target genes were represented in our liver proteome, and each protein was checked for relative expression between *Tst*$^{-/-}$ and 6J (on normal diet, threshold of $P < 0.01$). 10 of the 47 target genes were lower in abundance in the *Tst*$^{-/-}$ proteome, 37 unchanged, with none upregulated. To analyse whether this was statistically significant, we compared this to the percentage of proteins upregulated, down-regulated or unchanged in the proteome database. 5.86% of proteins were upregulated, 5.62% downregulated, and 88.6% unchanged in the full database (1654 proteins total). Expected (mean) numbers of proteins from a hypothetical set of 47 proteins, predict rounded values of 3 upregulated, 3 downregulated and 42 unchanged. We used these as a reference to the actual data for NRF2 target proteins; 0 upregulated, 10 downregulated and 37 unchanged. A Freeman-Halton Fisher Exact test was used for analysis of significance, and a significant difference between predicted and actual distribution was found ($P_A = 0.039$, $P_B = 0.047$).

Electron micrograph imaging. Liver tissue for transmission electron microscopy was prepared following immersion fixation in 0.1 M PB buffer (pH 7.4, EM-grade) containing 4% paraformaldehyde and 2.5% glutaraldehyde. 1mm tissue blocks were post-fixed in 1%

osmium tetroxide in 0.1 M PB for 45 min before dehydration through an ascending series of ethanol solutions and propylene oxide. Tissue blocks were then embedded in Durcupan before ultrathin sections (~60/70 nm) were cut and collected on formvar-coated grids (Agar Scientific, UK), stained with uranyl acetate and lead citrate in an LKB Ultrostainer and then quantitatively assessed in a Philips CM12 transmission electron microscope (TEM).

***Seahorse respiratory analysis*.** Primary hepatocytes (C57Bl/6J and *Tst*$^{-/-}$ mice) were seeded immediately following purification onto collagen coated V7 Seahorse 24-well cell culture microplates (Agilent Technologies), in 200 µl medium (DMEM, 5.5 mM glucose, 10% FCS, 7 mM glutamine, and penicillin/streptomycin antibiotics), for culture in a 5% CO_2 37°C incubator. Experiments were performed between 22-28 hours following collection from mice. Optimisation experiments determined the optimal seeding density, which was then standardised at 10,000/well. Optimisation for drugs and compounds used in Seahorse experiments were performed separately with hepatocytes for each genotype and dietary regime (normal or 58% high fat). This established the doses of drugs for respiratory manipulation, which were the same for both genotypes and diets; oligomycin (2 µM), FCCP (0.5 µM), and antimycin/rotenone (1 µM/0.2 µM). In all experiments, overnight media from cells was replaced, after two washes (0.75 ml), with 525 µl of run media and incubated for 30 mins at 37°C (without CO_2), prior to entry into the Seahorse XFe24 Extracellular Flux Analyser (Agilent). The analyser was operated using Wave software (Agilent), and all oxygen consumption rate (OCR) data was normalised to protein using the Sulforhodamine B stain (described above). Data from each biological replicate was averaged from between 4-10 replicate wells, to produce a single value at each measurement time for each biological replicate. Respiratory parameters were calculated as described below for each biological replicate, and this data was used for statistical analysis of genotype effects.

Mitochondrial stress test (MST). Run media for the MST was Seahorse assay media (Agilent), supplemented with 10 mM glucose, 2 mM sodium pyruvate, pH 7.35 ± 0.5 at 37°C). Most measurements were made using 3 min mixing, 2 min wait, 3 min measure. Measurements following addition of FCCP to hepatocytes from high fat fed mice were measured using 4 min mix, 2 min wait, 2 min measure. Three measurements were taken basally, and three measurements taken after injection of each drug (in sequence; oligomycin for inhibiting ATP-linked respiration, FCCP for eliciting maximal uncoupled respiration, antimycin/rotenone for inhibiting the respiratory electron chain). Respiratory parameters for each biological replicate were calculated from the mean normalised OCR as follows. *Basal respiration* was calculated by subtracting the third OCR measurement following injection of antimycin/rotenone (12^{th} measurement) from the third basal OCR measurement (3^{rd} measurement). *ATP linked respiration* was calculated by subtracting the third OCR measurement following the injection of oligomycin (6^{th} measurement) from the third basal OCR measurement (3^{rd} measurement). *Maximum (uncoupled) respiration* was calculated by subtracting the third OCR measurement after injection of antimycin/rotenone (12^{th} measurement) from the first measurement (peak OCR) following injection of FCCP (7^{th} measurement). *Proton leak respiration* was calculated by subtracting the third OCR measurement after injection of antimycin/rotenone (12^{th} measurement) from the third measurement following the injection of oligomycin (6^{th} measurement). *Non-respiratory OCR* was taken from the third measurement after the addition of antimycin/rotenone (12^{th} measurement).

Octanoate rescue test. To investigate lipid respiratory metabolism, hepatocytes were prepared, seeded and cultured overnight as above. Run media for the Octanoate rescue was Seahorse assay media (Agilent), supplemented with 5 mM glucose, 0.1 mM sodium pyruvate, 1 mM sodium lactate, and 0.5 mM carnitine pH 7.35 ± 0.5 at 37°C). All measurements were

made using 3 min mixing, 2 min wait, 3 min measure. After washing cells into run media, and 30 min before entry into the analyser, half of the wells from each genotype were incubated with 8 µM etomoxir (or DMSO vehicle) to block carnitine dependent import of long chain fatty acids into the mitochondria. Three basal measurements were taken prior to injection of oligomycin, two measurements were taken prior to FCCP, two measurements were taken prior to injection of sodium octanoate (250 µM), three measurements taken prior to antimycin/rotenone followed by two final measurements. Standard respiratory parameters were calculated analogous to the above description for the standard mitochondrial stress test, except using the second measurement following injection of drug when only 2 measurements were taken. Dependency upon endogenous fatty acids for supporting uncoupled respiration (*Etomoxir inhibited respiration*) was calculated for each biological replicate using the maximal respiration prior to the addition of octanoate. Maximal respiration was calculated as the 6^{th} measurement (peak FCCP OCR) – 12^{th} measurement (lowest Antimycin/Rotenone OCR). The mean maximal respiration from the etomoxir treated wells was subtracted from the mean maximal respiration of the vehicle treated wells to calculate the Etomoxir inhibited respiration (long chain fatty acid dependency) for that biological replicate. Octanoate stimulation of respiration (*Octanoate stimulated respiration*), was calculated for each vehicle well by subtracting the second OCR measurement after injection of FCCP (7^{th} measurement) from the third measurement after injection of octanoate (10^{th} measurement).

Real time for mRNA analysis. RNA extraction, cDNA synthesis and real-time PCR were performed as described (Morton *et al*., 2011, Moreno-Navarrete *et al*., 2013). Probes were mouse *Mpst*, Mm00460389_m1, *Tst*, Mm00726109_m1; *Gapdh* (internal control), Mm99999915_g1; and *Tbp* (internal control), Mm0000446973_m1.

QUANTIFICATION AND STATISTICAL ANALYSIS

Quantification and Statistical Analysis. For analytes, bioenergetics, fluorescent probes, gene expression, and protein levels, generally group sizes of 6 were calculated to allow detection of differences in these variable parameters to a threshold of 15% (there is sufficient power to detect smaller differences in certain parameters with this cohort size) with a power of at least 0.8. In some studies, limitations in animal numbers, or fewer remaining samples from larger group sizes resulting from their use for multiple end-points, precluded the desired minimum of $n = 6$ per group. Protein or mRNA differences in validation studies with 2 parameters (e.g. diet with line or genotype) were analysed using 2-way ANOVA for line and diet effects followed, where appropriate, by post-hoc Tukey tests or Holm-Sidak multiple comparison tests using Sigmastat version 3.5 (Systat Software) or Prism (Graphpad Software). For simple 2 condition comparisons, *t*-test was used. For simple control versus treated (including different treatments or concentration response curves) data were analysed by 1-way ANOVA. For longitudinal measures (e.g. PTT, ITT, bodyweight gain) repeated measures (RM) ANOVA was used and multiple comparisons determined. For all main *in vivo* studies, a blinding strategy was used where the operator (e.g. for injections of glucose, or administration of drug) was blind to the genotype of the subject during the experiment. Similarly, for analysis of images (e.g. oil-red O staining) the scorer was blind to genotype and the data coded, with the code broken by a second individual. Downstream analysis of e.g. tissue mRNA and protein content was not generally blinded to allow appropriate data arrangement on e.g. representative western blots. For clamp studies, mean ± standard error of mean (sem) will be presented, statistical analysis will use t-test to investigate differences of genotype on each diet (2 independent experiments, normal diet, and high fat diet, are not compared directly to

each other). Statistical significance and the number (n) of subjects or samples for analysis are indicated in the figure legends.

KEY RESOURCES TABLE

REAGENT or RESOURCE	SOURCE	IDENTIFIER
Antibodies		
Anti-TST	GeneTex	GTX114858
Anti-MPST	Abcam	ab224043
Anti-GOT1	Abcam	ab170950
Anti-GSTT1	Proteintech	15838-1-AP
Anti-MAT1A	Abcam	ab129176
Anti-BHMT	Proteintech	15965-1-AP
Anti-CSAD	Abcam	ab91016
Anti-PPCS	Atlas Antibodies	HPA031361
IRDye 800CW Goat anti-Rabbit	LiCor	926-32211
IRDye 680RD Donkey anti-Mouse	LiCor	926-68072
Anti-B-Actin	Abcam	ab8226
Anti-CoxIV	Abcam	Ab16056
Chemicals, peptides, and recombinant proteins		
sodium pyruvate $^{13}C_3$	Sigma-Aldrich	490717
Amyloglucosidase	Roche	ROAMYGLL
Antimycin A	Sigma-Aldrich	A8674
B-glycerophosphate	Sigma-Aldrich	G9422
B-mercaptoethanol	Sigma-Aldrich	444203
Bovine serum albumin, essentially fatty acid free	Sigma-Aldrich	10775835001
Carbonyl cyanide-p-trifluoromethoxyphenylhydrazone (FCCP)	Cayman Chemicals	15218
Oligomycin A	Cayman Chemicals	11342
DL-Carnitine hydrochloride	Sigma-Aldrich	C9500
Collagenase type 1	Worthington Laboratories	LS004194
cOmplete, Mini, EDTA-free Protease Inhibitor Cocktail	Roche	11836153001
Glucose, D-[3-^{3}H]	PerkinElmer	NET331C
Deoxycholic acid	Sigma-Aldrich	D2510
2'-deoxyguanosine 5'-diphosphate, sodium salt	Sigma-Aldrich	D9250
Dithiothreitol	Sigma-Aldrich	43816
Durcupan ACM	Sigma-Aldrich	44610
(+)- Etomoxir sodium salt hydrate	Sigma-Aldrich	E1905
EZ-link Maleimide-PEG2-Biotin	Thermo Fisher Scientific	21901BID
Fetal Calf Serum, Brazilian Origin	SLS Life Science	HYC85
Prestained Protein Marker	Proteintech	PL00001
Glutamax	Thermo Fisher Scientific	35050061
L-Glutamine	Sigma-Aldrich	G7513
Glycine	Sigma-Aldrich	50046
Hematoxylin solution	Abcam	Ab220365
Iodoacetamide	Sigma-Aldrich	I1149
L-cysteine	Sigma-Aldrich	30089
Lead citrate, tribasic trihydrate	Sigma-Aldrich	15326
Malate dehydrogenase, porcine heart	Sigma-Aldrich	442610-M

Skim Milk Powder	Millipore	70166
S-Methyl methanethiosulfonate	Sigma-Aldrich	64306
MitoSOX Red Mitochondrial superoxide indicator	Thermo Fisher Scientific	M36008
NADH, Grade I disodium salt	Roche	10107735001
Pierce NEM (N-ethylmaleimide)	Thermo Fisher Scientific	23030
Sodium octanoate	Sigma-Aldrich	C5038
Oil Red O	Sigma-Aldrich	O0625
Oligomycin A	Sigma-Aldrich	75351
Penicillin Streptomycin	Thermo Fisher Scientific	15140122
PERCOLL 8.5-9.5	Sigma-Aldrich	P1644
Phosphoenol pyruvate	Roche	10108294001
cOmplete protease cocktail inhibitor	Roche	04693159001
Rat tail collagen 1	Sigma-Aldrich	08-115
REVERT total protein stain	LICOR	926-11011
Rotenone	Sigma-Aldrich	R8875
Sequencing grade modified Trypsin	Promega	V5111
Sodium fluoride	Sigma-Aldrich	S7920
Sodium L-lactate	Sigma-Aldrich	71718
Sodium orthovanadate	Sigma-Aldrich	450243
Sodium pyrophosphate	Sigma-Aldrich	221368
Sodium pyruvate	Sigma-Aldrich	P8574
Sodium sulfate	Sigma-Aldrich	S9627
Sodium thiosulfate	Sigma-Aldrich	563188
Sodium sulfide	Sigma-Aldrich	407410
Sulforhodamine B dye	Sigma-Aldrich	230162
Taurine	Sigma-Aldrich	86329
Tetrabutylammonium phosphate	Sigma-Aldrich	86833
Trichloroacetic acid	Sigma-Aldrich	T6399
Triethylammonium bicarbonate	Sigma-Aldrich	18597
Trifluoracetic acid	Sigma-Aldrich	80457
Uranyl acetate	Electron Microscopy Sciences	22400
Urea	Sigma-Aldrich	U5128
XF Seahorse Base Media (DMEM)	Agilent	102353-100
^{14}C-2-deoxyglucose	Perkin Elmer	NEC495A
4-(2-Hydroxyethyl)-1-piperazine propanesulfonic acid	Sigma-Aldrich	1.15230
2,4-nitrofluorobenzene	Sigma-Aldrich	D1529
Critical commercial assays		
Infinity Triglyceride Assay	Thermo Fisher Scientific	TR22421
Infinity Cholesterol Assay	Thermo Fisher Scientific	TR13421
Glucose Hexokinase Assay	Abcam	Ab136957
iTRAQ reagent – 8PLEX	Sigma-Aldrich	4281663
Deposited data		
Proteome	ProteomeXchange	PXD028909
Persulfidome	ProteomeXchange	PXD028909
Experimental models: Cell lines		
Primary hepatocytes	C57BL/6J and *Tst*$^{-/-}$ mice	n/a

Experimental models: Organisms/strains		
C57BL/6J (JAX mice strain)	Charles River	Strain code: 632
Tst$^{-/-}$ C57Bl/6N mouse (backcrossed for >10 generations at University of Edinburgh)	University California (Davis) International Mouse Knockout Project	VG13928; model Tst$^{tm1(KOMP)Vlcg}$
Oligonucleotides		
Tst (mouse) FAM gene expression assay 4331182	Thermo Fisher	Mm00726109_m1
Mpst (mouse) FAM gene expression assay 4331182	Thermo Fisher	Mm00460389_m1
Gapdh (mouse) FAM gene expression assay 4331182	Thermo Fisher	Mm99999915_g1
Tbp (mouse) FAM gene expression assay 4331182	Thermo Fisher	Mm0000446973_m1
Software and algorithms		
Microsoft office		
Graph Pad Prism v8, 9 and 10		
Other		
Amersham Hybond P blotting membranes, PVDF	Merck	GE10600021
Microvette CB300 K2E EDTA tubes	Sarstedt	16.444.100
Ultra-0.5 centrifugal filter, 10K cut off	Millipore	UFC501096
Streptavidin-agarose beads	Thermo Scientific	20347
Formvar coated grids	Agar Scientific	AGS138
Standard rodent diet	SDS	RM1
Cornstarch diet	Research Diets	D12383
58% High fat diet	Research Diets	D12331

SUPPLEMENTAL FIGURES and EXCEL TABLE; TITLES AND LEGENDS

Table S3 (Excel)

Table S3. *Tst* Deletion results in differential hepatic protein abundance of GO terms. Related to Table 3**.** (**A**) Significant GO terms represented by proteins that are more abundant in the ND-fed *Tst*$^{-/-}$ liver compared with normal diet-fed C57Bl/6J. (**B**) Significant GO terms represented by proteins that are less abundant in the ND-fed *Tst*$^{-/-}$ liver compared with normal diet-fed C57Bl/6J. '**Genes**' indicates the number of genes in the *Tst*$^{-/-}$ that represent the changes driving the GO term. The lists include all regulated GO terms at a significance threshold of $P < 0.05$

REFERENCES

Abe, K. and Kimura, H. (1996) 'The possible role of hydrogen sulfide as an endogenous neuromodulator.', *The Journal of neuroscience : the official journal of the Society for Neuroscience*, 16(3), pp. 1066–71. Available at: http://www.ncbi.nlm.nih.gov/pubmed/8558235.

Altszuler, N. *et al.* (1956) 'Measurement of size and turnover rate of body glucose pool by the isotope dilution method.', *The American journal of physiology*, 187(1), pp. 15–24.

Arndt, S. *et al.* (2017) 'Assessment of H 2 S in vivo using the newly developed mitochondria-targeted mass spectrometry probe MitoA', *Journal of Biological Chemistry*. American Society for Biochemistry and Molecular Biology Inc., 292(19), pp. 7761–7773. doi: 10.1074/jbc.M117.784678.

Banerjee, R. *et al.* (2015) *Assay methods for H2S biogenesis and catabolism enzymes*, *Methods in Enzymology*. Academic Press Inc. doi: 10.1016/bs.mie.2014.11.016.

Billaut-Laden, I. *et al.* (2006) 'Evidence for a functional genetic polymorphism of the human thiosulfate sulfurtransferase (Rhodanese), a cyanide and H2S detoxification enzyme', *Toxicology*. Elsevier Ireland Ltd, 225(1), pp. 1–11. doi: 10.1016/j.tox.2006.04.054.

Bonomi, F. *et al.* (1977) *Rhodanese-Mediated Sulfur Transfer to Succinate Dehydrogenase*, *Eur. J. Biochem*.

Bromley, J. *et al.* (2005) 'Life-threatening interaction between complementary medicines: Cyanide toxicity following ingestion of amygdalin and vitamin C', *Annals of Pharmacotherapy*, 39(9), pp. 1566–1569. doi: 10.1345/aph.1E634.

Caron, S. *et al.* (2011) 'Transcriptional activation of apolipoprotein CIII expression by glucose may contribute to diabetic dyslipidemia', *Arteriosclerosis, Thrombosis, and Vascular Biology*, 31(3), pp. 513–519. doi: 10.1161/ATVBAHA.110.220723.

Carter, R. N. and Morton, N. M. (2016) 'Cysteine and hydrogen sulphide in the regulation of metabolism: Insights from genetics and pharmacology', *Journal of Pathology*, pp. 321–332. doi: 10.1002/path.4659.

Chen, X., Jhee, K. H. and Kruger, W. D. (2004) 'Production of the neuromodulator H2S by cystathionine beta-synthase via the condensation of cysteine and homocysteine', *Journal of Biological Chemistry*. doi: 10.1074/jbc.C400481200.

Consoli, A. *et al.* (1989) 'Predominant role of gluconeogenesis in increased hepatic glucose production in NIDDM', *Diabetes*, 38(5), pp. 550–557. doi: 10.2337/diab.38.5.550.

Cuadrado A, Rojo AI, Wells G, *et al*., (2019) Therapeutic targeting of the NRF2 and KEAP1 partnership in chronic diseases. *Nat Rev Drug Discov*. doi:10.1038/s41573-018-0008-x

Curry, S. C., Carlton, M. W. and Raschke, R. A. (1997) 'Prevention of fetal and maternal cyanide toxicity from nitroprusside with coinfusion of sodium thiosulfate in gravid ewes', *Anesthesia and Analgesia*, 84(5), pp. 1121–1126. doi: 10.1213/00000539-199705000-00031.

Desai, K. M. *et al.* (2011) 'Hydrogen sulfide and the metabolic syndrome', *Expert Review of Clinical Pharmacology*, 4(1), pp. 63–73. doi: 10.1586/ecp.10.133.

Distrutti, E. *et al.* (2008) 'The methionine connection: Homocysteine and hydrogen sulfide exert opposite effects on hepatic microcirculation in rats', *Hepatology*, 47(2), pp. 659–667. doi: 10.1002/hep.22037.

Feng, X. *et al.* (2009) 'Hydrogen sulfide from adipose tissue is a novel insulin resistance regulator', *Biochemical and Biophysical Research Communications*. doi: 10.1016/j.bbrc.2009.01.059.

Filipovic, M. R. *et al.* (2017) 'Chemical Biology of H2S Signaling through Persulfidation', *Chemical Reviews*. doi: 10.1021/acs.chemrev.7b00205.

Fiorucci, S. *et al.* (2005) 'The third gas: H2S regulates perfusion pressure in both the isolated

and perfused normal rat liver and in cirrhosis', *Hepatology*, 42(3), pp. 539–548. doi: 10.1002/hep.20817.

Gao, X. H. *et al.* (2015) 'Quantitative H2S-mediated protein sulfhydration reveals metabolic reprogramming during the integrated stress response', *eLife*. eLife Sciences Publications Ltd, 4(NOVEMBER2015). doi: 10.7554/eLife.10067.

Geng, B. *et al.* (2013) 'Increase or Decrease Hydrogen Sulfide Exert Opposite Lipolysis, but Reduce Global Insulin Resistance in High Fatty Diet Induced Obese Mice', *PLoS ONE*, 8(9). doi: 10.1371/journal.pone.0073892.

Gero, Domokos Torregrossa, R. *et al.* (2016) *The novel mitochondria-targeted hydrogen sulfide (H2S) donors AP123 and AP39 protect against hyperglycemic injury in microvascular endothelial cells in vitro*, *Pharmacological Research*. Available at: https://reader.elsevier.com/reader/sd/pii/S1043661816306314?token=3623BE1502342420421E3956873F1E65FD3FCBDE1D675D7396DB26A…1/13.

Ghosh Dastidar, S. *et al.* (2018) ' Glutathione S -transferase P deficiency induces glucose intolerance via JNK-dependent enhancement of hepatic gluconeogenesis ', *American Journal of Physiology-Endocrinology and Metabolism*. American Physiological Society, 315(5), pp. E1005–E1018. doi: 10.1152/ajpendo.00345.2017.

Hildebrandt, T. M. *et al.* (2013) 'Proteome adaptations in Ethe1-deficient mice indicate a role in lipid catabolism and cytoskeleton organization via post-translational protein modifications', *Bioscience Reports*. Portland Press Ltd., 33(4), pp. 575–584. doi: 10.1042/bsr20130051.

Hildebrandt, T. M. and Grieshaber, M. K. (2008) 'Three enzymatic activities catalyze the oxidation of sulfide to thiosulfate in mammalian and invertebrate mitochondria', *FEBS Journal*, 275(13), pp. 3352–3361. doi: 10.1111/j.1742-4658.2008.06482.x.

Hine, C. *et al.* (2015) 'Endogenous hydrogen sulfide production is essential for dietary restriction benefits', *Cell*. doi: 10.1016/j.cell.2014.11.048.

Hine, C. *et al.* (2017) 'Hypothalamic-Pituitary Axis Regulates Hydrogen Sulfide Production', *Cell Metabolism*. doi: 10.1016/j.cmet.2017.05.003.

Hine, C. *et al.* (2018) 'Dietary and Endocrine Regulation of Endogenous Hydrogen Sulfide Production: Implications for Longevity', *Antioxidants & Redox Signaling*. Mary Ann Liebert Inc, 28(16), pp. 1483–1502. doi: 10.1089/ars.2017.7434.

Jackson, M. R., Melideo, S. L. and Jorns, M. S. (2012) 'Human sulfide:Quinone oxidoreductase catalyzes the first step in hydrogen sulfide metabolism and produces a sulfane sulfur metabolite', *Biochemistry*. doi: 10.1021/bi300778t.

Jain, S. K. *et al.* (2014) 'Vitamin D and L-cysteine levels correlate positively with GSH and negatively with insulin resistance levels in the blood of type 2 diabetic patients', *European Journal of Clinical Nutrition*. Nature Publishing Group, 68(10), pp. 1148–1153. doi: 10.1038/ejcn.2014.114.

Kabil, O., Motl, N. and Banerjee, R. (2014) 'H2S and its role in redox signaling', *Biochimica et Biophysica Acta - Proteins and Proteomics*, pp. 1355–1366. doi: 10.1016/j.bbapap.2014.01.002.

Karwi, Q. G., Bice, J. S. and Baxter, G. F. (2018) 'Pre- and postconditioning the heart with hydrogen sulfide (H2S) against ischemia/reperfusion injury in vivo: a systematic review and meta-analysis', *Basic Research in Cardiology*. Dr. Dietrich Steinkopff Verlag GmbH and Co. KG. doi: 10.1007/s00395-017-0664-8.

Kashala-Abotnes, E. *et al.* (2019) 'Konzo: a distinct neurological disease associated with food (cassava) cyanogenic poisoning', *Brain Research Bulletin*. Elsevier Inc., pp. 87–91. doi: 10.1016/j.brainresbull.2018.07.001.

1402 Kim, M. S. *et al.* (2016) 'ChREBP regulates fructose-induced glucose production
1403 independently of insulin signaling', *Journal of Clinical Investigation*. American Society for
1404 Clinical Investigation, 126(11), pp. 4372–4386. doi: 10.1172/JCI81993.
1405 Kimura, Y. *et al.* (2017) '3-Mercaptopyruvate sulfurtransferase produces potential redox
1406 regulators cysteine- and glutathione-persulfide (Cys-SSH and GSSH) together with signaling
1407 molecules H 2 S 2 , H 2 S 3 and H 2 S', *Scientific Reports*. Nature Publishing Group, 7(1), pp.
1408 1–14. doi: 10.1038/s41598-017-11004-7.
1409 Koike, S., Nishimoto, S. and Ogasawara, Y. (2017) 'Cysteine persulfides and polysulfides
1410 produced by exchange reactions with H2S protect SH-SY5Y cells from methylglyoxal-induced
1411 toxicity through Nrf2 activation', *Redox Biology*. Elsevier B.V., 12, pp. 530–539. doi:
1412 10.1016/j.redox.2017.03.020.
1413 Krishnan, N. *et al.* (2011) 'H2S-Induced Sulfhydration of the Phosphatase PTP1B and Its Role
1414 in the Endoplasmic Reticulum Stress Response', *Science Signaling*. doi:
1415 10.1126/scisignal.2002329.
1416 Lee, B. C., Kaya, A. and Gladyshev, V. N. (2016) 'Methionine restriction and life-span control',
1417 *Annals of the New York Academy of Sciences*. doi: 10.1111/nyas.12973.
1418 Lewis, G. F. *et al.* (2002) 'Disordered fat storage and mobilization in the pathogenesis of
1419 insulin resistance and type 2 diabetes', *Endocrine Reviews*, pp. 201–229. doi:
1420 10.1210/edrv.23.2.0461.
1421 Libiad, M. *et al.* (2014) 'Organization of the human mitochondrial hydrogen sulfide oxidation
1422 pathway', *Journal of Biological Chemistry*. doi: 10.1074/jbc.M114.602664.
1423 Libiad, M. *et al.* (2018) 'Thiosulfate Sulfurtransferase like Domain Containing 1 Protein
1424 Interacts with Thioredoxin.', *The Journal of biological chemistry*. American Society for
1425 Biochemistry and Molecular Biology, p. jbc.RA117.000826. doi: 10.1074/jbc.RA117.000826.

Libiad, M., Sriraman, A. and Banerjee, R. (2015) 'Polymorphic variants of human rhodanese exhibit differences in thermal stability and sulfur transfer kinetics', *Journal of Biological Chemistry*. doi: 10.1074/jbc.M115.675694.

Lutchmansingh, F. K. *et al.* (2018) 'Glutathione metabolism in type 2 diabetes and its relationship with microvascular complications and glycemia', *PLoS ONE*. Public Library of Science, 13(6). doi: 10.1371/journal.pone.0198626.

Mani, S. *et al.* (2013) 'Decreased endogenous production of hydrogen sulfide accelerates atherosclerosis', *Circulation*, 127(25), pp. 2523–2534. doi: 10.1161/CIRCULATIONAHA.113.002208.

Mani, S. *et al.* (2014) 'Hydrogen sulfide and the liver', *Nitric Oxide - Biology and Chemistry*. doi: 10.1016/j.niox.2014.02.006.

Mason, T. M. (1998) 'The role of factors that regulate the synthesis and secretion of very-low-density lipoprotein by hepatocytes', *Critical Reviews in Clinical Laboratory Sciences*, pp. 461–487. doi: 10.1080/10408369891234246.

Meakin, P. J. *et al.* (2014) 'Susceptibility of Nrf2-Null Mice to Steatohepatitis and Cirrhosis upon Consumption of a High-Fat Diet Is Associated with Oxidative Stress, Perturbation of the Unfolded Protein Response, and Disturbance in the Expression of Metabolic Enzymes but Not with I', *Molecular and Cellular Biology*. American Society for Microbiology, 34(17), pp. 3305–3320. doi: 10.1128/mcb.00677-14.

Mikami, Y. *et al.* (2011) 'Thioredoxin and dihydrolipoic acid are required for 3-mercaptopyruvate sulfurtransferase to produce hydrogen sulfide', *Biochemical Journal*. doi: 10.1042/BJ20110841.

Miller, R. A. *et al.* (2005) 'Methionine-deficient diet extends mouse lifespan, slows immune and lens aging, alters glucose, T4, IGF-I and insulin levels, and increases hepatocyte MIF

levels and stress resistance', *Aging Cell*. doi: 10.1111/j.1474-9726.2005.00152.x.

Mishanina, T. V., Libiad, M. and Banerjee, R. (2015) 'Biogenesis of reactive sulfur species for signaling by hydrogen sulfide oxidation pathways', *Nature Chemical Biology*, pp. 457–464. doi: 10.1038/nchembio.1834.

Mithieux, G. et al. (2003) 'Induction of control genes in intestinal gluconeogenesis is sequential during fasting and maximal in diabetes', *Am J Physiol Endocrinol Metab. doi: 10.1152/ajpendo 00299.2003*

Módis, K. *et al.* (2013) 'Intramitochondrial hydrogen sulfide production by 3-mercaptopyruvate sulfurtransferase maintains mitochondrial electron flow and supports cellular bioenergetics', *FASEB Journal*. doi: 10.1096/fj.12-216507.

Moreno-Navarrete J. M. *et al.* (2013) 'Decreased RB1 mRNA, protein, and activity reflect obesity-induced altered adipogenic capacity in human adipose tissue'. *Diabetes*. doi:10.2337/db12-0977

Morris, A. A. *et al.* (2017) 'Thiocyanate Accumulation in Critically Ill Patients Receiving Nitroprusside Infusions', *Journal of Intensive Care Medicine*. SAGE Publications Inc., 32(9), pp. 547–553. doi: 10.1177/0885066616657004.

Morton N. M. *et al.* (2011) 'A stratified transcriptomics analysis of polygenic Fat and Lean mouse adipose tissues identifies novel candidate obesity genes', *PLoS One*. doi:10.1371/journal.pone.0023944

Morton, N. M. *et al.* (2016) 'Genetic identification of thiosulfate sulfurtransferase as an adipocyte-expressed antidiabetic target in mice selected for leanness', *Nature Medicine*, 22(7). doi: 10.1038/nm.4115.

Mosharov, E., Cranford, M. R. and Banerjee, R. (2000) 'The quantitatively important relationship between homocysteine metabolism and glutathione synthesis by the

transsulfuration pathway and its regulation by redox changes', *Biochemistry*, 39(42), pp. 13005–13011. doi: 10.1021/bi001088w.

Mutel. E. *et al.* (2011) 'Control of blood glucose in the absence of hepatic glucose production during prolonged fasting in mice' *Diabetes*, doi: 10.2337/db11-0571/-/DC1.

Nagahara, N. (2011) 'Catalytic Site Cysteines of Thiol Enzyme: Sulfurtransferases', *Journal of Amino Acids*. doi: 10.4061/2011/709404.

Nagahara, N. (2018) 'Multiple role of 3-mercaptopyruvate sulfurtransferase: antioxidative function, H2S and polysulfide production and possible SOx production', *British Journal of Pharmacology*. John Wiley and Sons Inc., pp. 577–589. doi: 10.1111/bph.14100.

Nagahara, N. *et al.* (2019) 'Novel Characterization of Antioxidant Enzyme, 3-Mercaptopyruvate Sulfurtransferase-Knockout Mice: Overexpression of the Evolutionarily-Related Enzyme Rhodanese', *Antioxidants*. MDPI AG, 8(5), p. 116. doi: 10.3390/antiox8050116.

Nandi, D. L., Horowitz, P. M. and Westley, J. (2000) 'Rhodanese as a thioredoxin oxidase', *The International Journal of Biochemistry & Cell Biology*, 32(4), pp. 465–473. doi: 10.1016/S1357-2725(99)00035-7.

Nandi, D. L. and Westley, J. (1998) 'Reduced thioredoxin as a sulfur-acceptor substrate for rhodanese', *International Journal of Biochemistry and Cell Biology*. doi: 10.1016/S1357-2725(98)00050-8.

Norris, E. J. *et al.* (2011) 'The liver as a central regulator of hydrogen sulfide', *Shock*. doi: 10.1097/SHK.0b013e3182252ee7.

O'brien, B., Quigg, C. and Leong, T. (2005) *Severe cyanide toxicity from 'vitamin supplements'*, *European Journal of Emergency Medicine*. Lippincott Williams & Wilkins. Available at: http://www.cancer.gov/cancerinfo/pdq/cam.laetrile.

OMS (2014) ‘GLOBAL REPORT ON DIABETES WHO Library Cataloguing-in-Publication Data’, *ISBN*, 978, pp. 92–4. Available at: http://www.who.int/about/licensing/.

Onkenhout, W. *et al.* (1995) *Identification and Quantification of Intermediates of Unsaturated Fatty Acid Metabolism in Plasma of Patients with Fatty Acid Oxidation Disorders*, *#{149} Molecular Pathology and Genetics CLINICAL CHEMISTRY*.

Owen, O. E. (1969) 'Liver and kidney metabolism during proloned starvation', *The Journal of Clinical Investigation.* doi: 10.1172/JCI106016

Pagani, S. and Galante, Y. M. (1983) *INTERACTION OF RHODANESE WITH MITOCHONDRIAL NADH DEHYDROGENASE*, *Biochimica et Biophysics Acta*.

Perez-Riverol Y., Csordas A., Bai J., Bernal-Llinares M., Hewapathirana S, Kundu DJ, Inuganti A, Griss J, Mayer G, Eisenacher M, Pérez E, Uszkoreit J, Pfeuffer J, Sachsenberg T, Yilmaz S, Tiwary S, Cox J, Audain E, Walzer M, Jarnuczak AF, Ternent T, Brazma A, Vizcaíno JA (2019). The PRIDE database and related tools and resources in 2019: improving support for quantification data. Nucleic Acids Res 47(D1):D442-D450 (PubMed ID: 30395289).

Peters, J. M. *et al.* (1997) ‘Alterations in lipoprotein metabolism in peroxisome proliferator-activated receptor α-deficient mice’, *Journal of Biological Chemistry*. American Society for Biochemistry and Molecular Biology Inc., 272(43), pp. 27307–27312. doi: 10.1074/jbc.272.43.27307.

Petrova, F. (2004) ‘Hydrogen cyanide and cyanides : human health aspects’, p. 67.

Pichette, J. and Gagnon, J. (2016) ‘Implications of Hydrogen Sulfide in Glucose Regulation: How H2S Can Alter Glucose Homeostasis through Metabolic Hormones’, *Oxidative Medicine and Cellular Longevity*. doi: 10.1155/2016/3285074.

Qian, K. *et al.* (2015) ‘Hepatic ALT isoenzymes are elevated in gluconeogenic conditions including diabetes and suppressed by insulin at the protein level’, *Diabetes/Metabolism*

Research and Reviews. John Wiley and Sons Ltd, 31(6), pp. 562–571. doi: 10.1002/dmrr.2655.

Reiffenstein, R. (1992) 'Toxicology Of Hydrogen Sulfide', *Annual Review of Pharmacology and Toxicology*. Annual Reviews, 32(1), pp. 109–134. doi: 10.1146/annurev.pharmtox.32.1.109.

Rooney J, Oshida K, Vasani N, *et al.* (2018) 'Activation of Nrf2 in the liver is associated with stress resistance mediated by suppression of the growth hormone-regulated STAT5b transcription factor' *PLoS One*. doi:10.1371/journal.pone.0200004

Rui, L. (2014) 'Energy metabolism in the liver', *Comprehensive Physiology*. Wiley-Blackwell Publishing Ltd, 4(1), pp. 177–197. doi: 10.1002/cphy.c130024.

Sasaki M. et al. (2017) 'Dual regulation of gluconeogenesis by insulin and glucose in the proximal tubules of the kidney' *Diabetes* doi: 10.2337/db16-1602

Sestito, S. *et al.* (2017) 'Hydrogen Sulfide: A Worthwhile Tool in the Design of New Multitarget Drugs', *Frontiers in Chemistry*. Frontiers Media SA, 5. doi: 10.3389/fchem.2017.00072.

Shibuya, N. *et al.* (2009) '3-Mercaptopyruvate Sulfurtransferase Produces Hydrogen Sulfide and Bound Sulfane Sulfur in the Brain', *Antioxidants & Redox Signaling*. doi: 10.1089/ars.2008.2253.

Shimokawa, I. *et al.* (2015) 'The life-extending effect of dietary restriction requires Foxo3 in mice', *Aging cell*. doi: 10.1111/acel.12340.

Singh, S. *et al.* (2009) 'Relative contributions of cystathionine ??-synthase and ??-cystathionase to H2S biogenesis via alternative trans-sulfuration reactions', *Journal of Biological Chemistry*. doi: 10.1074/jbc.M109.010868.

Singha, S. *et al.* (2015) 'Toward a selective, sensitive, fast-responsive, and biocompatible

two-photon probe for hydrogen sulfide in live cells', *Analytical Chemistry*. American Chemical Society, 87(2), pp. 1188–1195. doi: 10.1021/ac503806w.

Slocum, S. L. *et al.* (2016) 'Keap1/Nrf2 pathway activation leads to a repressed hepatic gluconeogenic and lipogenic program in mice on a high-fat diet', *Archives of Biochemistry and Biophysics*. Academic Press Inc., 591, pp. 57–65. doi: 10.1016/j.abb.2015.11.040.

Smirnov, A. *et al.* (2010) 'Mitochondrial enzyme rhodanese is essential for 5 S ribosomal RNA import into human mitochondria', *Journal of Biological Chemistry*. American Society for Biochemistry and Molecular Biology Inc., 285(40), pp. 30792–30803. doi: 10.1074/jbc.M110.151183.

Sookoian, S. *et al.* (2016) 'Serum aminotransferases in nonalcoholic fatty liver disease are a signature of liver metabolic perturbations at the amino acid and Krebs cycle level', *American Journal of Clinical Nutrition*. American Society for Nutrition, 103(2), pp. 422–434. doi: 10.3945/ajcn.115.118695.

Stumvoll M. (1998) 'Glucose production by the human kidney - it's importance has been underestimated' *Nephrol Dial Transplant* doi: 10.1093/ndt/13.12.2996

Swerdlow, D. I. *et al.* (2015) 'HMG-coenzyme A reductase inhibition, type 2 diabetes, and bodyweight: Evidence from genetic analysis and randomised trials', *The Lancet*. Lancet Publishing Group, 385(9965), pp. 351–361. doi: 10.1016/S0140-6736(14)61183-1.

Szabo, C. (2011) 'Roles of Hydrogen Sulfide in the Pathogenesis of Diabetes Mellitus and Its Complications', *Antioxidants & Redox Signaling*. Mary Ann Liebert Inc, 17(1), pp. 68–80. doi: 10.1089/ars.2011.4451.

Szabo, C. *et al.* (2014) 'Regulation of mitochondrial bioenergetic function by hydrogen sulfide. Part I. Biochemical and physiological mechanisms', *British Journal of Pharmacology*. doi: 10.1111/bph.12369.

Szabó, G. *et al.* (2011) 'Cardioprotective effects of hydrogen sulfide', in *Nitric Oxide - Biology and Chemistry*, pp. 201–210. doi: 10.1016/j.niox.2010.11.001.

Tiranti, V. *et al.* (2009) 'Loss of ETHE1, a mitochondrial dioxygenase, causes fatal sulfide toxicity in ethylmalonic encephalopathy', *Nature Medicine*, 15(2), pp. 200–205. doi: 10.1038/nm.1907.

Tolwani, R. J. *et al.* (2005) 'Medium-chain acyl-CoA dehydrogenase deficiency in gene-targeted mice', *PLoS Genetics*, 1(2), pp. 0205–0212. doi: 10.1371/journal.pgen.0010023.

Tonelli C, Chio IIC, Tuveson DA. (2018) 'Transcriptional Regulation by Nrf2' *Antioxidants Redox Signal*. doi:10.1089/ars.2017.7342

Uyeda, K. and Repa, J. J. (2006) 'Carbohydrate response element binding protein, ChREBP, a transcription factor coupling hepatic glucose utilization and lipid synthesis', *Cell Metabolism*, pp. 107–110. doi: 10.1016/j.cmet.2006.06.008.

Vinnakota, C. V. *et al.* (2012) 'Comparison of cyanide exposure markers in the biofluids of smokers and non-smokers', *Biomarkers*, 17(7), pp. 625–633. doi: 10.3109/1354750X.2012.709880.

Vitvitsky, V. *et al.* (2006) 'A functional transsulfuration pathway in the brain links to glutathione homeostasis', *Journal of Biological Chemistry*, 281(47), pp. 35785–35793. doi: 10.1074/jbc.M602799200.

Vitvitsky, V. *et al.* (2015) 'Sulfide oxidation by a noncanonical pathway in red blood cells generates thiosulfate and polysulfides', *Journal of Biological Chemistry*. American Society for Biochemistry and Molecular Biology Inc., 290(13), pp. 8310–8320. doi: 10.1074/jbc.M115.639831.

Vitvitsky, V. *et al.* (2017) 'Structural and mechanistic insights into hemoglobincatalyzed hydrogen sulfide oxidation and the fate of polysulfide products', *Journal of Biological*

Chemistry. doi: 10.1074/jbc.M117.774943.

Walsh J, Jenkins RE, Wong M, *et al*. (2014) 'Identification and quantification of the basal and inducible Nrf2-dependent proteomes in mouse liver: Biochemical, pharmacological and toxicological implications' *J Proteomics*. doi:10.1016/j.jprot.2014.05.007

Wang, R. (2012) 'Physiological Implications of Hydrogen Sulfide: A Whiff Exploration That Blossomed', *Physiological Reviews*, 92(2), pp. 791–896. doi: 10.1152/physrev.00017.2011.

Wedmann, R. *et al.* (2016) 'Improved tag-switch method reveals that thioredoxin acts as depersulfidase and controls the intracellular levels of protein persulfidation', *Chemical Science*. Royal Society of Chemistry, 7(5), pp. 3414–3426. doi: 10.1039/c5sc04818d.

Whiteman, M. *et al.* (2011) 'Emerging role of hydrogen sulfide in health and disease: critical appraisal of biomarkers and pharmacological tools', *Clinical Science*, 121(11), pp. 459–488. doi: 10.1042/cs20110267.

Wu, D. *et al.* (2015) 'Exogenous hydrogen sulfide mitigates the fatty liver in obese mice through improving lipid metabolism and antioxidant potential', *Medical Gas Research*. BioMed Central Ltd., 5(1). doi: 10.1186/s13618-014-0022-y.

Xie, L. *et al.* (2016) 'Hydrogen sulfide induces Keap1 S-sulfhydration and suppresses diabetes-accelerated atherosclerosis via Nrf2 activation', *Diabetes*. American Diabetes Association Inc., 65(10), pp. 3171–3184. doi: 10.2337/db16-0020.

Xue, R. *et al.* (2013) 'Hydrogen Sulfide Treatment Promotes Glucose Uptake by Increasing Insulin Receptor Sensitivity and Ameliorates Kidney Lesions in Type 2 Diabetes', *Antioxidants & Redox Signaling*, 19(1), pp. 5–23. doi: 10.1089/ars.2012.5024.

Yadav, P. K. *et al.* (2013) 'Structure and kinetic analysis of H2S production by human mercaptopyruvate sulfurtransferase', *Journal of Biological Chemistry*. doi: 10.1074/jbc.M113.466177.

Yang, G. *et al.* (2013) 'Hydrogen sulfide protects against cellular senescence via s-sulfhydration of keap1 and activation of Nrf2', *Antioxidants and Redox Signaling*, 18(15), pp. 1906–1919. doi: 10.1089/ars.2012.4645.

Zhang, L. *et al.* (2013) 'Hydrogen sulfide impairs glucose utilization and increases gluconeogenesis in hepatocytes', *Endocrinology*. doi: 10.1210/en.2012-1658.

Zhang, L. *et al.* (2018) 'Hydrogen sulfide (H2S)-releasing compounds: Therapeutic potential in cardiovascular diseases', *Frontiers in Pharmacology*. Frontiers Media S.A. doi: 10.3389/fphar.2018.01066.

Zhang, Y. K. J. *et al.* (2012) 'Nrf2 deficiency improves glucose tolerance in mice fed a high-fat diet', *Toxicology and Applied Pharmacology*, 264(3), pp. 305–314. doi: 10.1016/j.taap.2012.09.014.

Figure 1

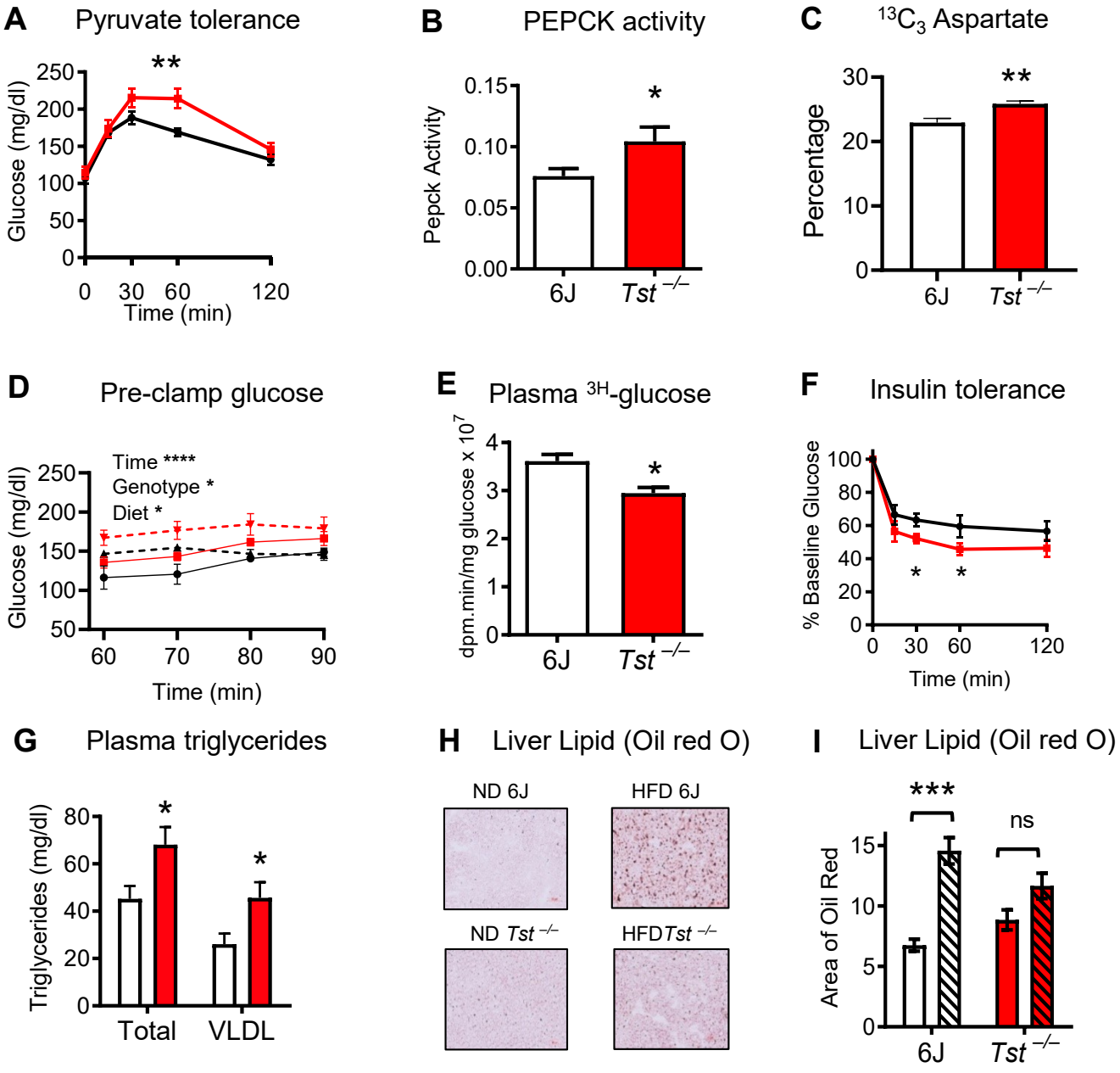
A
Pyruvate tolerance
**
Glucose (mg/dl)
250
200
150
100
50
0
0
30
60
120
Time (min)
B
PEPCK activity
*
Pepck Activity
0.15
0.10
0.05
0.00
6J
Tst −/−
C
13C3 Aspartate
**
Percentage
30
20
10
0
6J
Tst −/−
D
Pre-clamp glucose
Time ****
Genotype *
Diet *
Glucose (mg/dl)
250
200
150
100
50
60
70
80
90
Time (min)
E
Plasma 3H-glucose
*
dpm.min/mg glucose x 10^7
4
3
2
1
0
6J
Tst −/−
F
Insulin tolerance
% Baseline Glucose
100
80
60
40
20
0
*
*
0
30
60
120
Time (min)
G
Plasma triglycerides
*
*
Triglycerides (mg/dl)
80
60
40
20
0
Total
VLDL
H
Liver Lipid (Oil red O)
ND 6J
HFD 6J
ND Tst −/−
HFD Tst −/−
I
Liver Lipid (Oil red O)
***
ns
Area of Oil Red
15
10
5
0
6J
Tst −/−

Figure 2

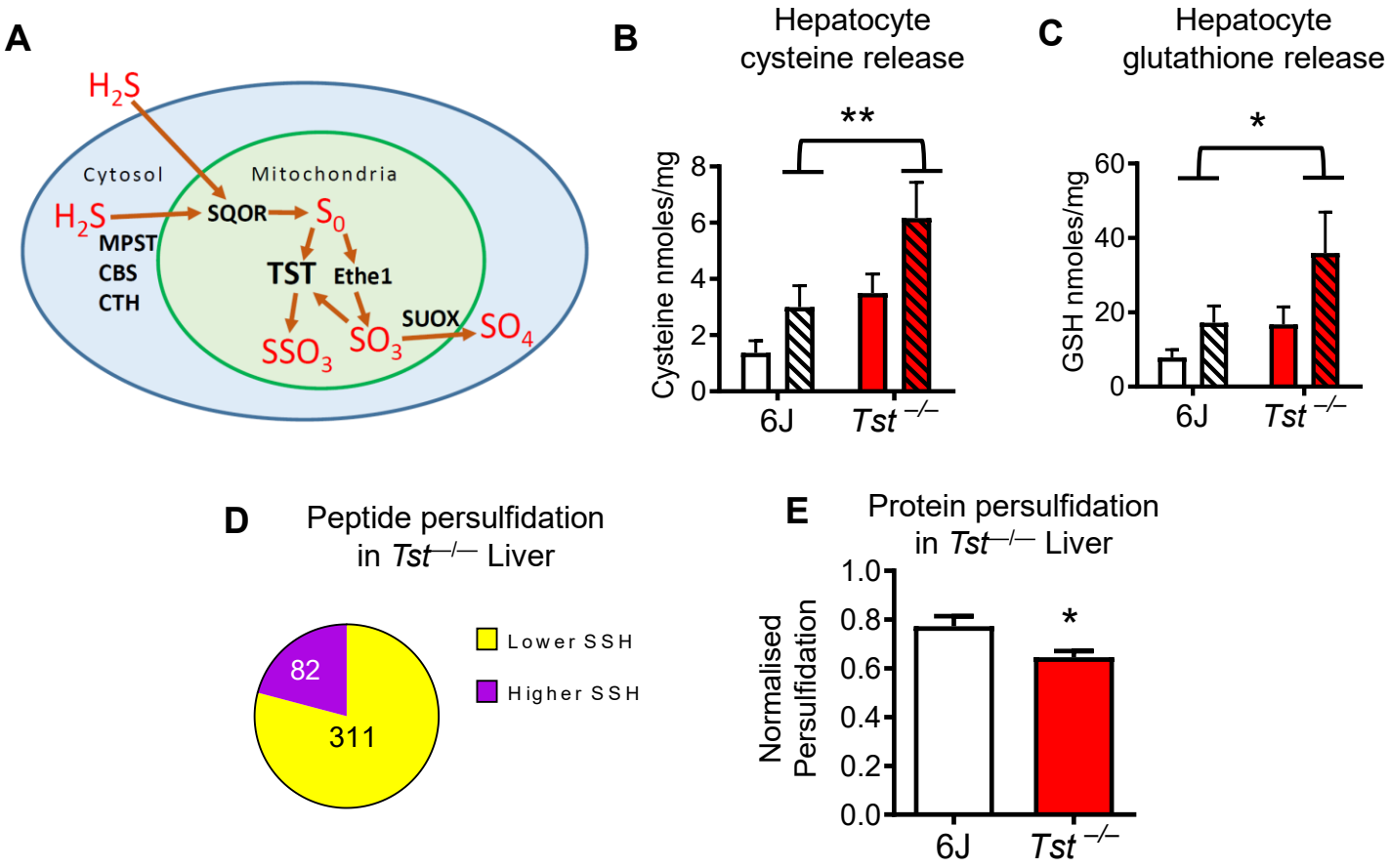
A
H_2S
Cytosol
Mitochondria
H_2S
SQOR
S_0
MPST
CBS
CTH
TST
Ethe1
SUOX
SSO_3
SO_3
SO_4
B
Hepatocyte cysteine release
**
Cysteine nmoles/mg
8
6
4
2
0
6J
Tst −/−
C
Hepatocyte glutathione release
*
GSH nmoles/mg
60
40
20
0
6J
Tst −/−
D
Peptide persulfidation in Tst−/− Liver
82
311
Lower SSH
Higher SSH
E
Protein persulfidation in Tst−/− Liver
Normalised Persulfidation
1.0
0.8
0.6
0.4
0.2
0.0
*
6J
Tst −/−

Figure 3

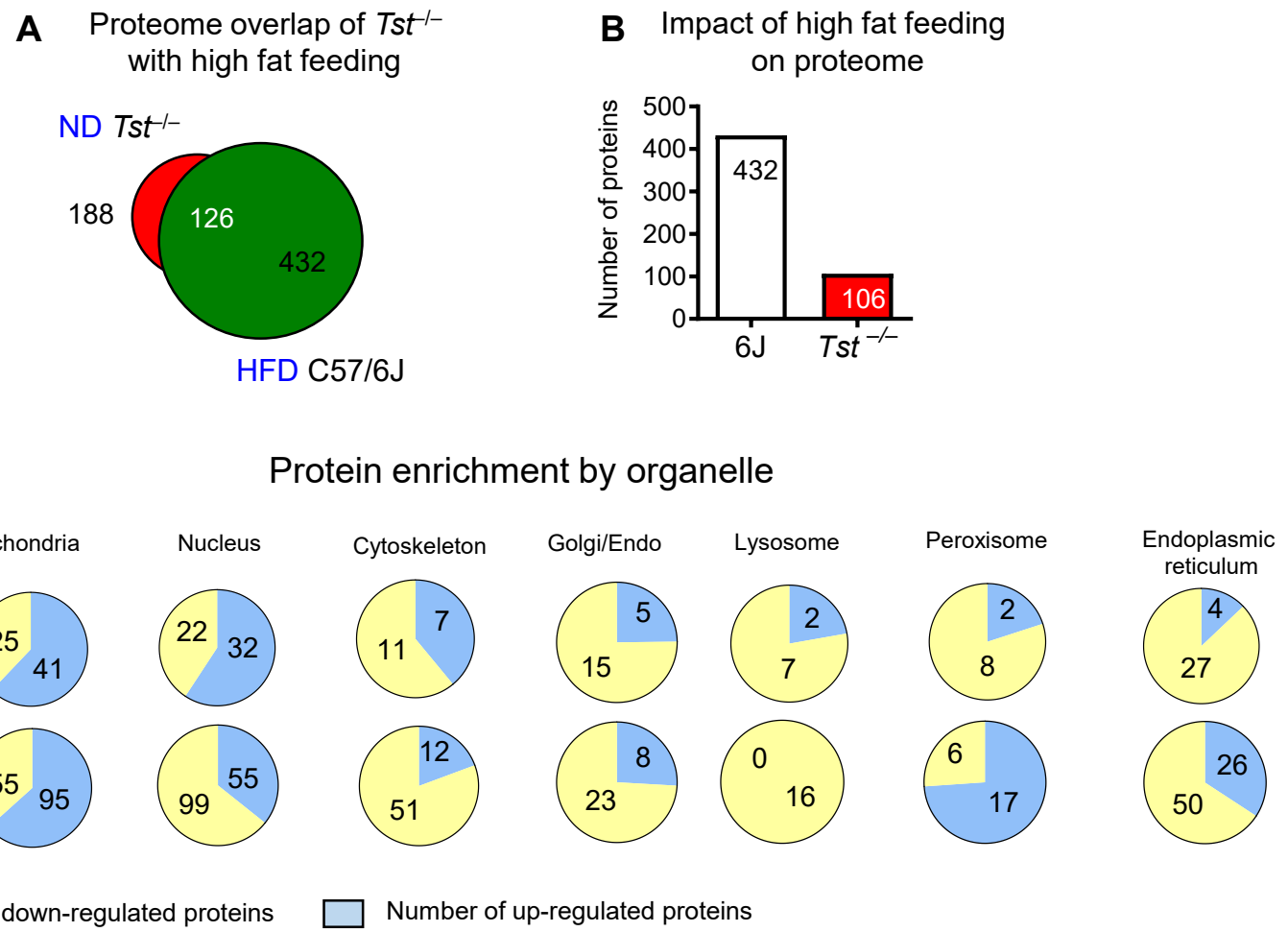
A
Proteome overlap of Tst−/− with high fat feeding
ND Tst−/−
188
126
432
HFD C57/6J
B
Impact of high fat feeding on proteome
Number of proteins
500
400
300
200
100
0
432
106
6J
Tst −/−
Protein enrichment by organelle
C
Mitochondria
Nucleus
Cytoskeleton
Golgi/Endo
Lysosome
Peroxisome
Endoplasmic reticulum
Tst−/− vs 6J
25
41
22
32
11
7
15
5
7
2
8
2
27
4
HFD vs ND
55
95
99
55
51
12
23
8
0
16
6
17
50
26
Number of down-regulated proteins
Number of up-regulated proteins

Figure 4

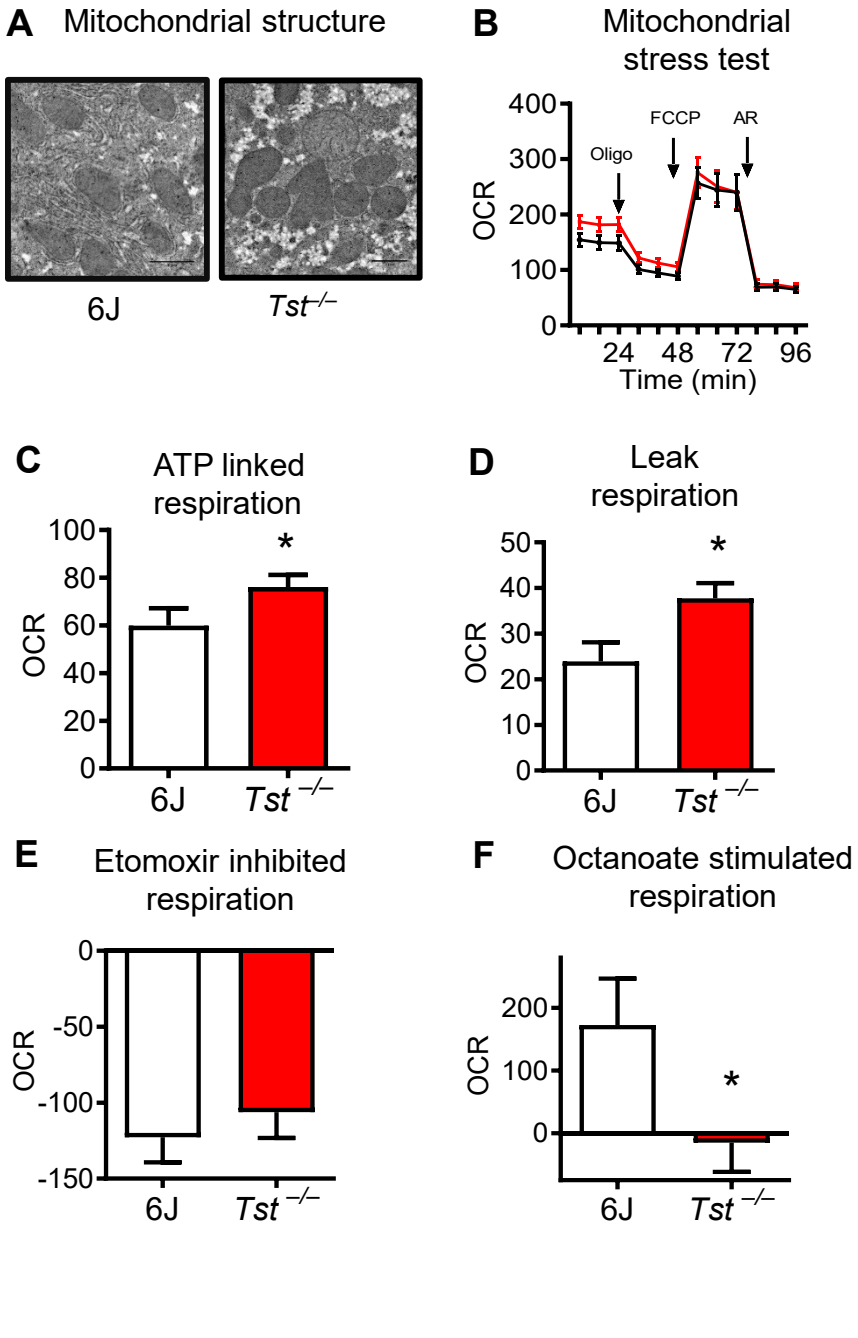
A
Mitochondrial structure
6J
Tst−/−
B
Mitochondrial stress test
OCR
Oligo
FCCP
AR
Time (min)
C
ATP linked respiration
OCR
6J
Tst −/−
D
Leak respiration
OCR
6J
Tst −/−
E
Etomoxir inhibited respiration
OCR
6J
Tst −/−
F
Octanoate stimulated respiration
OCR
6J
Tst −/−

Figure S1. *Tst* mRNA tissue expression profile in C57BL/6J mice and the metabolic fates of $^{13}C_3$ pyruvate in hepatocytes from *Tst*$^{-/-}$ mice. Related to Figure 1

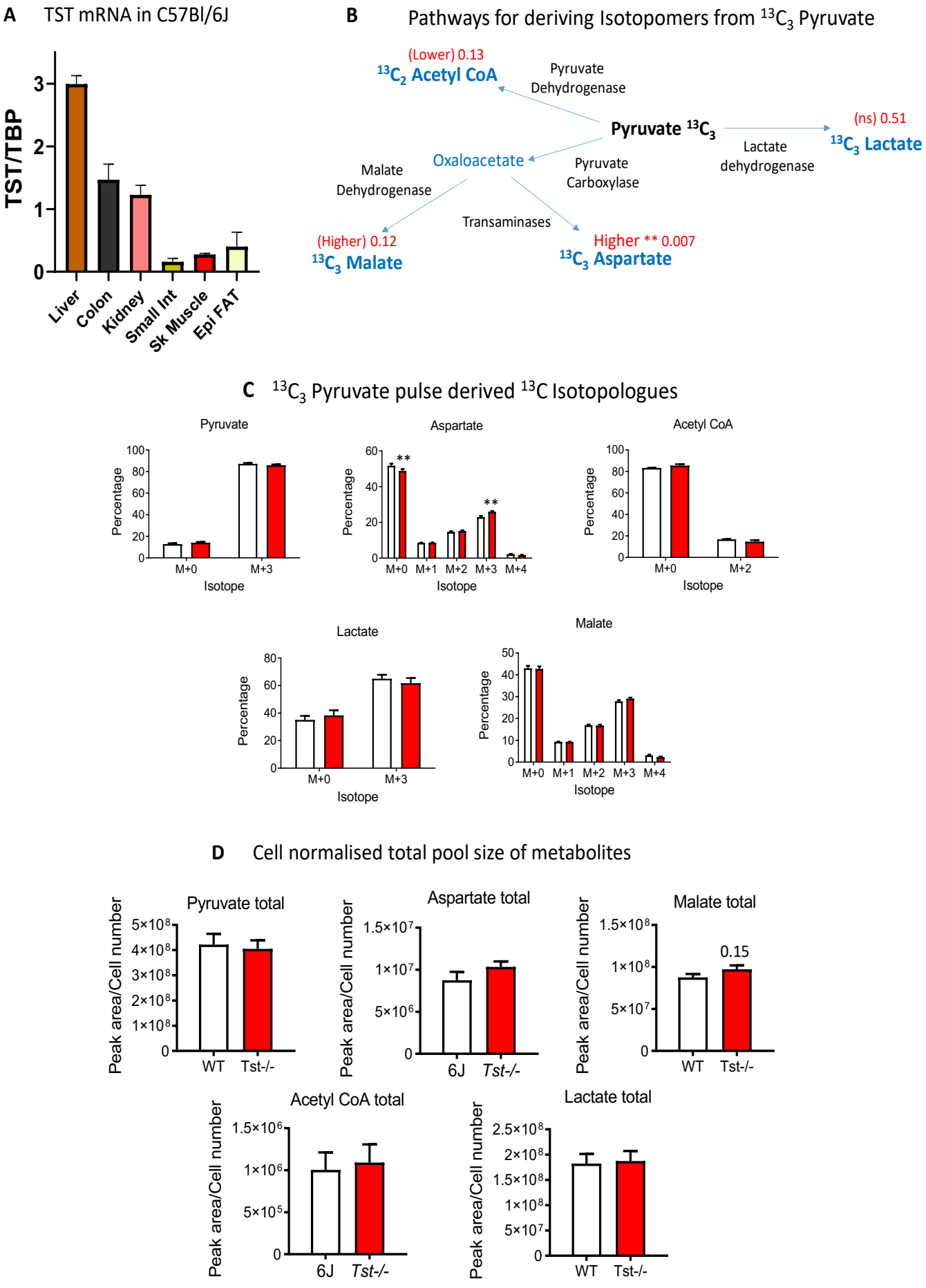

Figure S1. *Tst* mRNA tissue expression profile in C57BL/6J mice and the metabolic fates of $^{13}C_3$ pyruvate in hepatocytes from *Tst*$^{-/-}$ mice. Related to Figure 1 **(A)** Histogram showing *Tst* mRNA level across liver, colon, kidney, small intestine, skeletal muscle and epididymal fat from male C57BL/6J mice measured by realtime-PCR and normalised to *Tbp* mRNA **(B)** Diagram representing metabolites derived from pyruvate. Oxaloacetate was not detected but is indicated as an intermediate to production of malate or aspartate. The isotopologue shown on the diagram represents to most abundant detected following pulse with $^{13}C_3$ pyruvate. In red is the direction of change in hepatocytes of *Tst*$^{-/-}$ mice, with significance or P-values (when less than 0.2) from t-tests**.** (**C**) Histogram showing isotopologues derived from $^{13}C_3$ pyruvate from C57Bl/6J (white bars, n = 5) and *Tst*$^{-/-}$ (red bars n = 4) cultured hepatocytes. Data represents the amount of isotopologues detected by mass spectrometry, as a percentage of the total detected metabolite (total includes unlabelled ^{12}C and all detected ^{13}C isotopologues). Counts were first normalised to cell number. **(D)** Histograms showing the total pool size of each metabolite. Data is cell normalised mass spec counts from all isotopologues of the given metabolite, including the relevant unlabelled ^{12}C species. Data are represented as mean ± SEM. Each metabolite was analysed using a t-test, ** indicates that $P < 0.01$. P-values less than 0.2 are also indicated for showing potential trends.

Figure S2. Insulin–regulated metabolic parameters in liver and plasma of *Tst* $^{-/-}$ mice. Related to Figure 1.

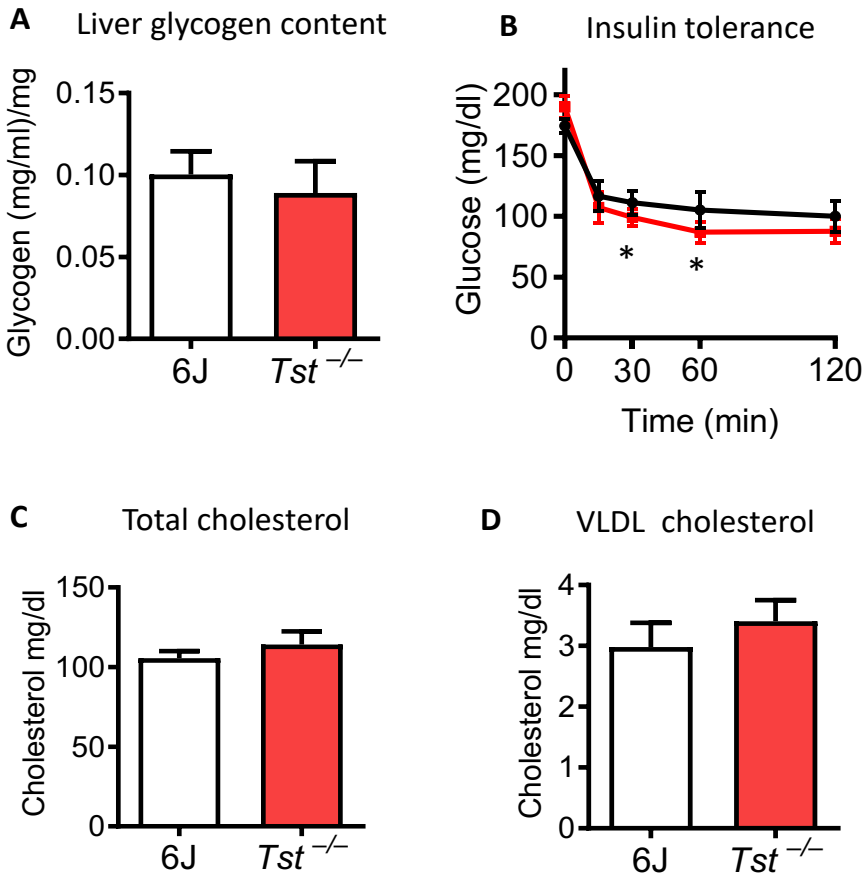

Figure S2. Insulin–regulated metabolic parameters in liver and plasma of *Tst* $^{-/-}$ mice. Related to Figure 1. (**A**) Glycogen measured from whole liver from normal diet-fed 4 hour fasted C57Bl/6J (6J; white bar, n = 5), and *Tst*$^{-/-}$ (red bar, n = 5) mice. Data are represented as mean ±SEM. (**B**) Plasma glucose (mg/dl), over 120 minutes following insulin administration (i.p., 1mU/g) in normal diet-fed 4 hour fasted C57Bl/6J (black line, n = 8) and *Tst*$^{-/-}$ (red line, n = 7) mice. (**C**) HPLC quantified total plasma cholesterol in normal diet-fed 4 hour fasted C57Bl/6J (white bar, n = 6) and *Tst*$^{-/-}$ (red bar, n = 6) mice. (**D**) HPLC quantified VLDL plasma cholesterol in normal diet-fed 4 hour fasted C57Bl/6J (white bar, n = 6), and *Tst*$^{-/-}$ (red bar, n = 6) mice. For (**B**) a Repeated Measures analysis demonstrated a significant effect of time (****) and an interaction between time and genotype (*). T-tests revealed that the decrement of glucose from baseline at 30 and 60 minutes after insulin was greater in the *Tst*$^{-/-}$ (*).

Figure S3. Hepatocytes from *Tst*$^{-/-}$ mice resist hydrogen peroxide induced mitochondrial reactive species accumulation. Related to Figure 2 and Table 1

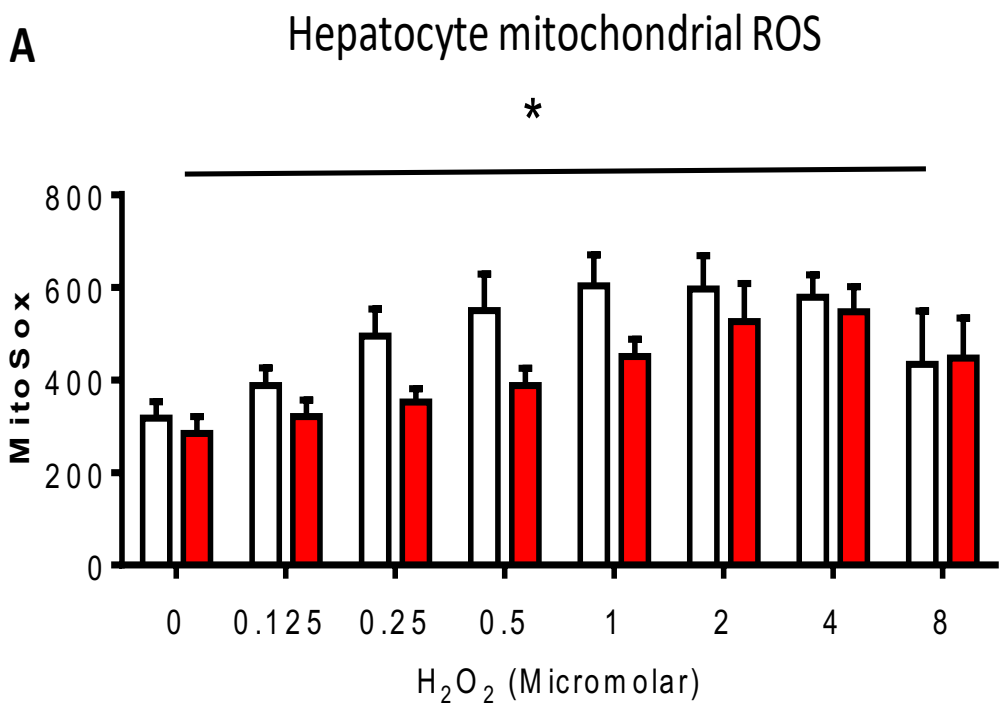

Figure S3. Hepatocytes from *Tst*$^{-/-}$ mice resist hydrogen peroxide induced mitochondrial reactive species accumulation. Related to Figure 2 and Table 1 **(A)** Mitochondrial reactive oxygen species measured from primary hepatocytes by MitoSox fluorescence from C57Bl/6J (white bars, n = 7) and *Tst*$^{-/-}$ (red bars, n = 7). Cells were exposed to a range of doses of H_2O_2 prior to MitoSox incubation and fluorescent detection. Data are represented as mean ±SEM. Significance was calculated using 2-WAY ANOVA for H_2O_2 dose and genotype. A significant effect of genotype is represented above the histogram with a *. H_2O_2 was significant to $P < 0.001$ (not represented on the histogram).

Figure S4. Persulfidation in the gluconeogenesis pathway is significantly different to global persulfidation patterns in the liver of the *Tst*$^{-/-}$ mice. Related to Figure 2 and Table 3.

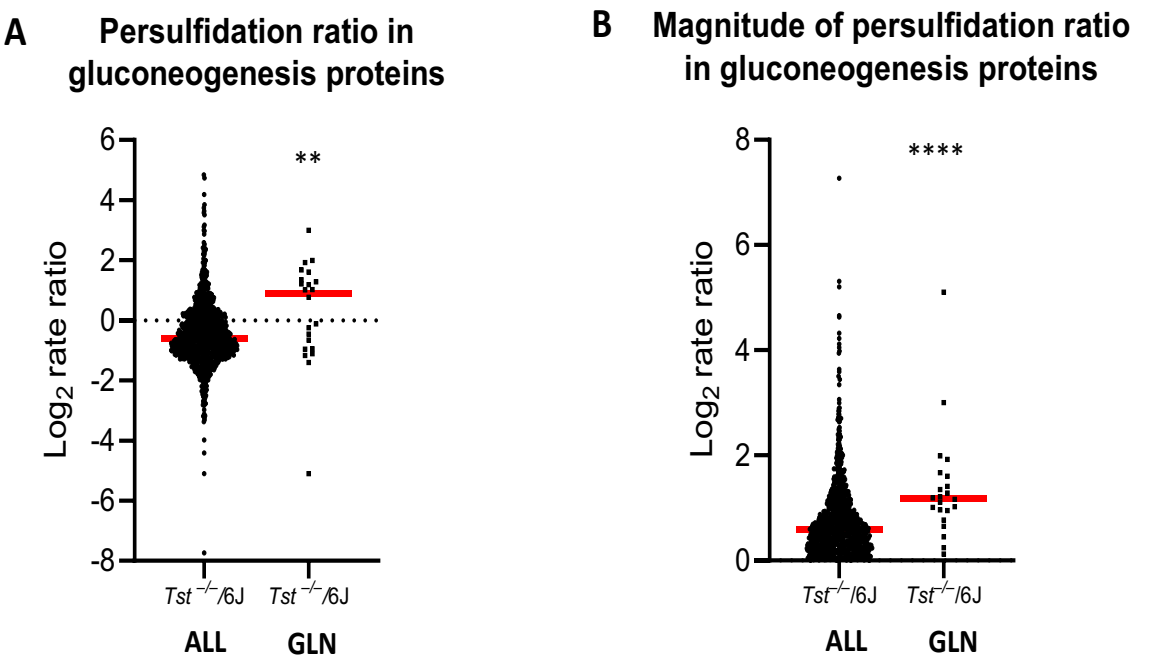

Figure S4. Persulfidation in the gluconeogenesis pathway is significantly different to global persulfidation patterns in the liver of the *Tst*$^{-/-}$ mice. Related to Figure 1, Figure 2 and Table 3. (**A**) Beeswarm plots showing the persulfidation $\log_2$ rate ratio (*Tst*$^{-/-}$ divided by 6J) for peptides in the entire data set (ALL), alongside the $\log_2$ rate ratio for peptides corresponding to proteins of gluconeogenesis (GLN). (**B**) Beeswarm plots showing the magnitude of the $\log_2$ rate ratio (independent to direction of change), for peptides in the entire data set (ALL), alongside the $\log_2$ rate ratios for peptides corresponding to proteins of gluconeogenesis (GLN). Data are represented as individual peptide $\log_2$ rate ratio values, with the median represented as a red line. Significance was calculated using the Mann-Whitney U non parametric T-test. ** $P < 0.01$, **** $P < 0.0001$.

Figure S5. Validation of proteomic profiles by select western blot is exemplified by increased mitochondrial MPST. Related to Figure 3 and Table 3.

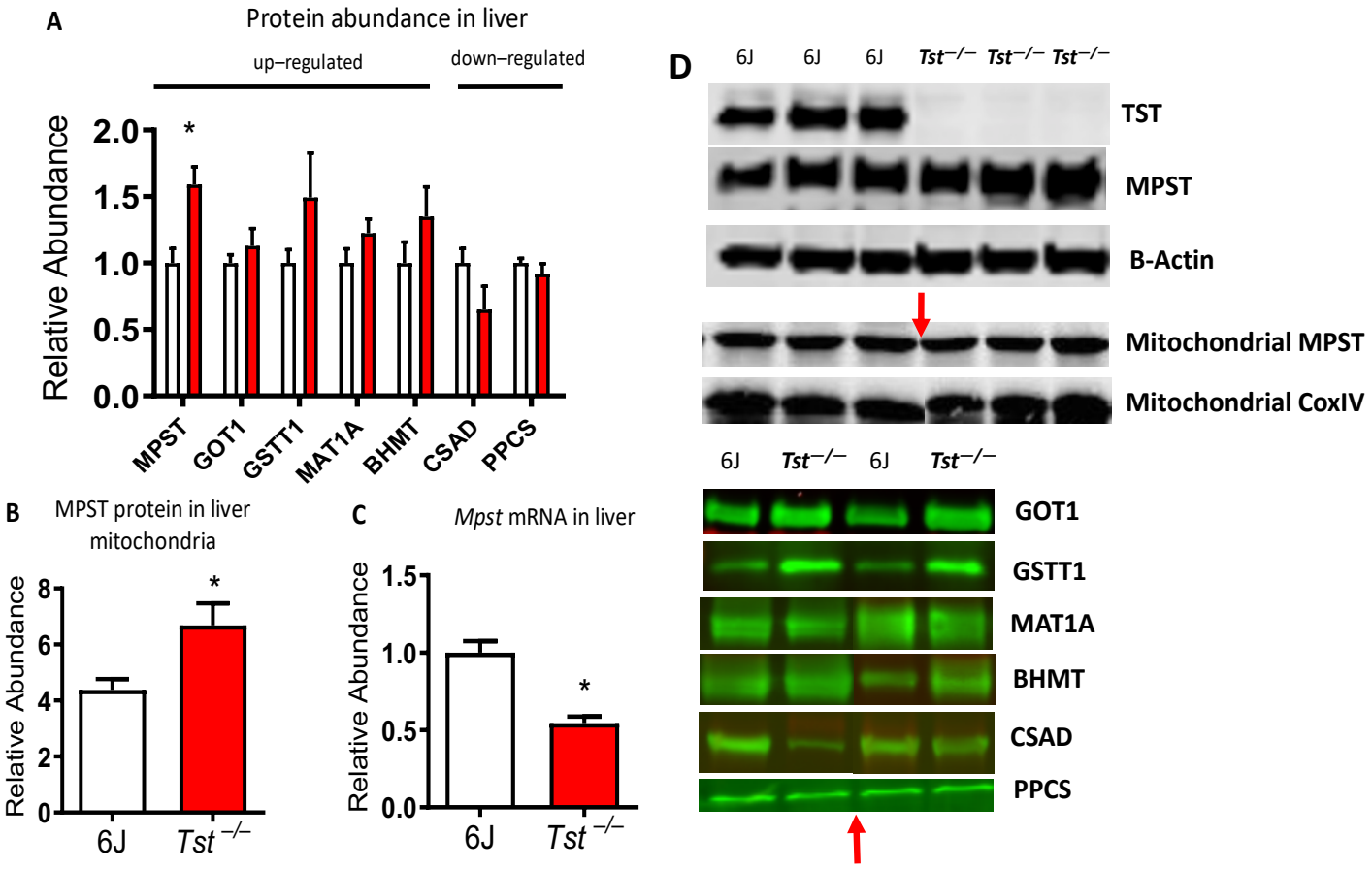

Figure S5. Validation of proteomic profiles by select western blot is exemplified by increased mitochondrial MPST. Related to Figure 2 and Table 3. (**A**) Quantification of western blots for a range of proteins found significantly up or down-regulated in the liver proteome of normal diet-fed 4 hour fasted C57Bl/6J (6J; white bar, n = 4-6) and *Tst*$^{-/-}$ (red bar, n = 4-6) mice. (**B**) Quantification of western blots for MPST from isolated liver mitochondria of normal diet-fed 4 hour fasted C57Bl/6J (white bar, n = 6), and *Tst*$^{-/-}$ (red bar, n = 6) mice. (**C**) *Mpst* mRNA quantified by real time PCR from liver of normal diet-fed C57Bl/6J (6J; white bar, n = 6) and *Tst*$^{-/-}$ (red bar, n = 6) mice. (**D**) Representative blots from LICOR imaging for the data quantified in (**A**). Red arrow indicates where superfluous lanes have been removed to simplify visualisation of genotype comparisons (GOT1, MAT1A, BHMT CSAD, mitochondrial MPST and COXIV). Data are represented as mean ±SEM. Significance was calculated using un-paired two-tailed student's t-test. * $P < 0.05$, ** $P < 0.01$, *** $P < 0.001$.

Figure S6. Hepatic proteins enriched in *Tst* $^{-/-}$ mice show under-representation of NRF2 promoter binding sites. Related to Figure 3 and Table 3.

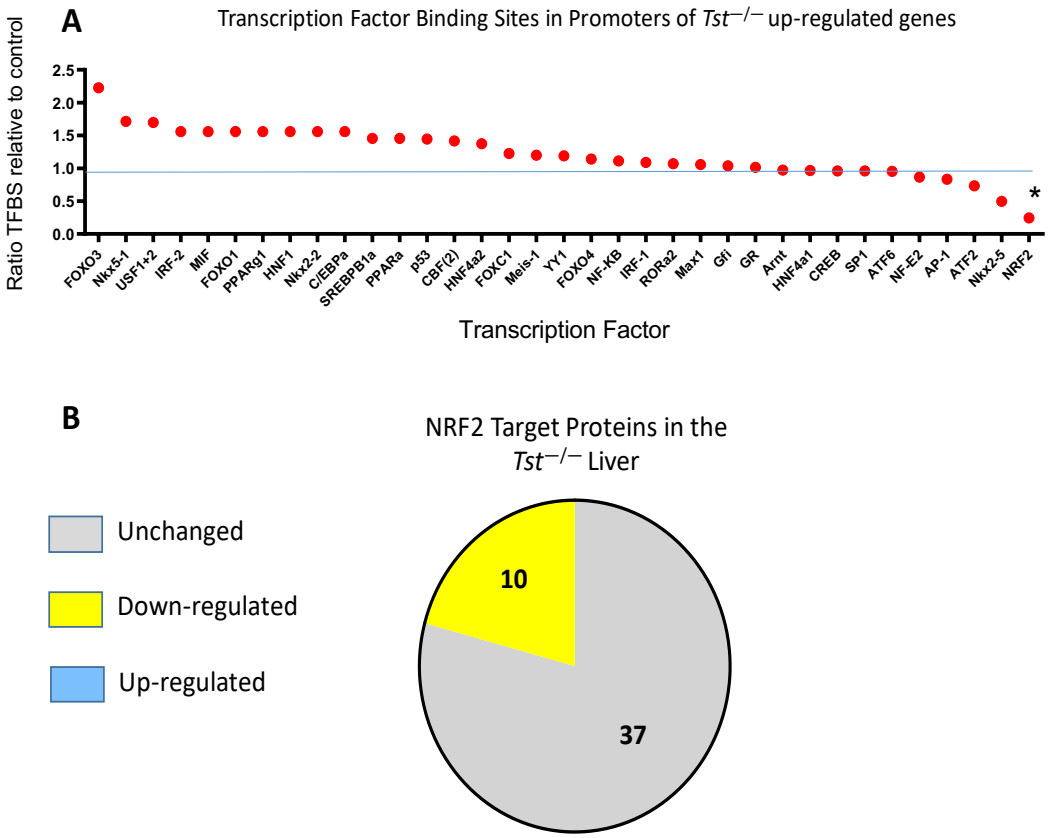

Figure S6. Hepatic proteins enriched in *Tst* $^{-/-}$ mice show under-representation of NRF2 promoter binding sites. Related to Figure 3 and Table 3. (**A**) abundance in *Tst*$^{-/-}$ liver compared to a control set of proteins that are unchanged between 6J and *Tst*$^{-/-}$. The proportion of genes containing a promoter binding site from proteins increased in *Tst*$^{-/-}$ was divided by the proportion of genes containing a binding site from a control set of genes. (**B**) Pie charts representing the number of NRF2-target proteins whose abundance is increased (blue), decreased (yellow) or unchanged (grey) in the Tst$^{-/-}$ liver. Significance of transcription factor enrichment analysis was calculated using a Fishers Exact test. * $P < 0.05$. Significance for NRF2 target abundance was performed with the Freeman-Halton Fishers Exact Test.

Figure S7. Hepatocyte respiration after high–fat feeding or after amino acid or pyruvate challenge is comparable between C57Bl/6J and *Tst*$^{-/-}$ mice *in vitro.* Related to Figure 4.

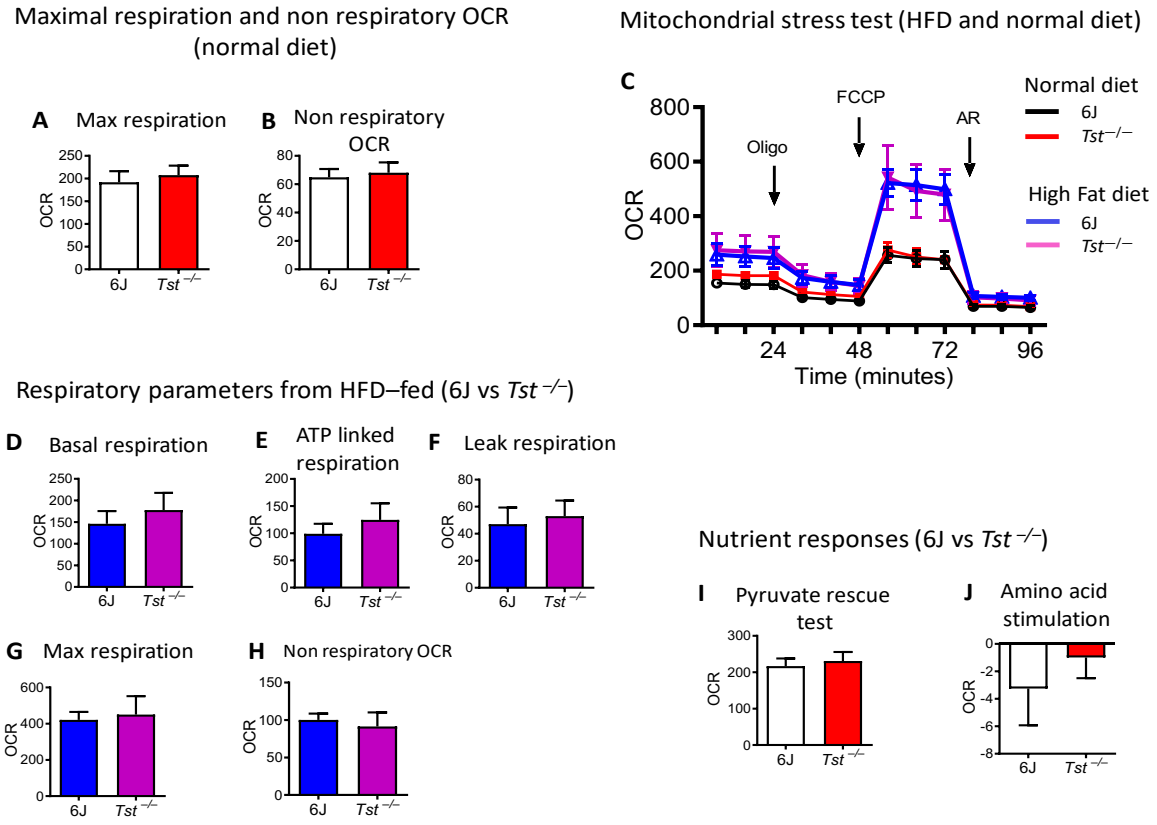

Figure S7. Hepatocyte respiration after high–fat feeding or after amino acid or pyruvate challenge is comparable between C57Bl/6J and *Tst*$^{-/-}$ mice *in vitro.* Related to Figure 4. (**A**) Maximal respiratory OCR elicited by uncoupling with FCCP, by hepatocytes from normal diet-fed C57Bl/6J (n = 6) or *Tst*$^{-/-}$ (n = 6) mice, calculated from Figure 3B. (**B**) Non-respiratory OCR remaining following the inhibition of respiration with antimycin and rotenone, by hepatocytes from normal diet-fed C57Bl/6J (n = 6) or *Tst*$^{-/-}$ (n = 6) mice, calculated from Figure 3B. (**C**) Seahorse trace representing the mean oxygen consumption rate (OCR), normalised to protein, by hepatocytes from normal diet-fed (n = 6/genotype), and high fat diet-fed (n = 4/genotype) C57Bl/6J and *Tst*$^{-/-}$mice during a mitochondrial stress test. (**D**)Basal respiratory OCR linked to ATP production (antimycin/rotenone sensitive) by hepatocytes from high fat diet-fed C57Bl/6J (n = 4) or *Tst*$^{-/-}$ (n = 4) mice, calculated from Figure S4C. (**E**) Respiratory OCR linked to ATP production (oligomycin sensitive) by hepatocytes from high fat diet-fed C57Bl/6J (n = 4) or *Tst*$^{-/-}$ (n = 4) mice, calculated from Figure S4C. (**F**) Respiratory OCR relating to proton leak (oligomycin insensitive) by hepatocytes from high fat diet-fed C57Bl/6J (n = 4) or *Tst*$^{-/-}$ (n = 4) mice, calculated from Figure S4C. (**G**) Maximal respiratory OCR elicited by uncoupling with FCCP, by hepatocytes from high fat diet-fed C57Bl/6J (n = 4) or *Tst*$^{-/-}$ (n = 4) mice, calculated from Figure S4C. (**H**) Non-respiratory OCR remaining following the inhibition of respiration with antimycin and rotenone, by hepatocytes high fat diet-fed C57Bl/6J (n = 4) or *Tst*$^{-/-}$ (n = 4) mice, calculated from Figure S4C. (**I**) Stimulation of maximal uncoupled respiration following addition of pyruvate (2mM), from normal diet-fed C57Bl/6J (n = 4) or *Tst*$^{-/-}$ (n = 4) mice. (**J**) Stimulation of maximal uncoupled respiration following addition of aspartate (1mM) and glutamax (1mM), by hepatocytes from normal diet-fed C57Bl/6J (n = 1) or *Tst*$^{-/-}$ (n = 1) mice. Data are represented as mean ±SEM. Significance was calculated using an unpaired two tailed, student's t-test. * $P < 0.05$.

Table S1. Parameters during the euglycemic hyperinsulinemic clamp

(A) Parameters during the basal (pre clamp) experiment (60-90 minutes post tracer)

Parameter	6J chow	*Tst*$^{-/-}$ chow	6J HFD	*Tst*$^{-/-}$ HFD	Genotype	Diet
Fasted Glucose 60 min (mg/dl)	116.35± 14.93	135.72± 7.22	146.50± 3.89	167.13± 9.68	*	**
Glycolysis (mg/kg/min)	11.63 ± 1.60	11.12 ± 0.62	12.89 ± 0.57	12.61 ± 0.62	ns	ns (0.09)
Glycogen synthesis (mg/kg/min)	21.48 ± 2.06	19.02 ± 2.04	15.08 ± 2.76	16.28 ± 2.50	ns	****

(B) Measurements and parameters during the clamp experiment (160-210 minutes post tracer)

Parameter	6J chow	*Tst*$^{-/-}$ chow	Genotype (chow)	6J HFD	*Tst*$^{-/-}$ HFD	Genotype (HFD)
Glucose 160 min (mg/dl)	108.0 ± 5.0	121.0 ± 10.1	ns	120.1± 3.7	125.6 ± 10.3	ns
Glucose 170 min (mg/dl)	120.3 ± 6.4	129.8 ± 5.8	ns	118.1 ± 4.1	143.9 ± 14.0	ns (0.08)
Glucose 180 min (mg/dl)	115.0 ± 5.5	125.5 ± 2.5	ns (0.08)	125.9 ± 2.9	126.7 ± 6.8	ns
Glucose 190 min (mg/dl)	124.0 ± 1.0	131.0 ± 4.6	ns	121.5 ± 4.7	116.1 ± 3.7	ns
Glucose 200 min (mg/dl)	121.0 ± 5.0	125.3 ± 5.8	ns	121.9 ± 3.0	115.7 ± 5.3	ns
Glucose 210 min (mg/dl)	113.0 ± 7.8	123.5 ± 4.6	ns	119.4 ± 4.0	116.9 ± 2.7	ns
Glucose IR 160-210 min (mg/kg/min)	84.9 ± 4.2	85.0 ± 2.6	ns	70.26 ± 4.83	69.95 ± 4.96	ns
Glucose IR 160 (mg/kg/min)	82.3 ± 5.1	87.1 ± 3.2	ns	68.8 ± 4.2	68.9 ± 5.1	ns
Glucose IR 170 (mg/kg/min)	85.2 ± 4.9	89.0 ± 3.0	ns	70.0 ± 5.1	74.6 ± 4.4	ns
Glucose IR 180 (mg/kg/min)	84.7 ± 4.4	83.5 ± 4.2	ns	70.6 ± 5.1	70.7 ± 6.2	ns
Glucose IR 190 (mg/kg/min)	85.2 ± 4.0	86.1 ± 2.1	ns	69.9 ± 4.8	69.1 ± 5.7	ns
Glucose IR 200 (mg/kg/min)	85.2 ± 4.0	84.8 ± 2.4	ns	70.4 ± 4.7	71.2 ± 4.5	ns
Glucose IR 210 (mg/kg/min)	85.2 ± 4.0	84.5 ± 2.4	ns	70.4 ± 4.7	71.2 ± 4.5	ns
Turnover (mg/kg/min)	85.97 ± 3.52	94.50 ± 3.87	ns	73.61 ± 5.07	63.08 ± 7.10	ns
Hepatic Glucose Prod. (mg/kg/min)	1.10 ± 5.31	9.92 ± 9.15	ns	3.326 ± 4.03	-6.83 ± 7.93	ns
Glycolysis (mg/kg/min)	45.90 ± 2.218	48.37 ± 2.05	ns	42.85 ± 1.48	36.42 ± 4.62	ns (0.19)
Glycogen synthesis (mg/kg/min)	40.06 ± 4.44	46.12 ± 2.68	ns	30.76 ± 5.36	26.66 ± 4.49	ns
Integral Glucose (dpm.min/mg)	$3.6e^7 \pm 1.4e^6$	$2.95e^7 \pm 1.2e^6$	*	$1.88e^7 \pm 1.4e^6$	$1.7e^7 \pm 1.6e^6$	ns
IWAT glucose utilization (ng/mg.min)	14.21 ± 4.05	18.62 ± 2.04	ns	4.53 ± 1.07	6.64 ± 1.00	ns
EWAT glucose utilization (ng/mg.min)	7.523 ± 4.39	7.21 ± 2.18	ns	2.94 ± 0.56	3.64 ± 0.39	ns
VL glucose utilization (ng/mg.min)	33.77 ± 2.98	38.66 ± 1.70	ns (0.17)	49.65 ± 9.19	47.42 ± 9.19	ns
EDL glucose utilization (ng/mg.min)	35.79 ± 11.09	40.86 ± 10.25	ns	68.79 ± 8.65	61.29 ± 11.80	ns
Soleus glucose utilization (ng/mg.min)	99.85 ± 12.38	123.60 ± 13.90	ns (0.13)	220.8 ± 24.45	198.5 ± 32.92	ns
Tibialis glucose utilization (ng/mg.min)	47.25 ± 7.22	53.67 ± 4.40	ns	74.39 ± 6.46	80.16 ± 6.09	ns
Heart glucose utilization (ng/mg.min)	161.40 ± 7.65	198.00 ± 14.09	ns (0.13)	226.6 ± 51.01	262.5 ± 23.29	ns
Liver glucose utilization (ng/mg.min)	3.53 ± 0.56	3.57 ± 0.63	ns	3.378 ± 0.39	3.58 ± 0.46	ns
End Clamp Insulin (µU/ml)	133.6 ± 7.03	126.4 ± 5.06	ns	147.2 ± 9.4	124.4 ± 10.9	ns

*** P < 0.05, ** P < 0.01, *** P < 0.001, **** P < 0.0001**

Table S1. Parameters during the euglycemic hyperinsulinemic clamp. Related to Figure 1. Metabolic parameters measured during continuous trace infusion but prior to clamp (**A**) and during maintenance of euglycemia and hyperinsulinemia (**B**) from C57Bl/6J (chow-fed, n = 3, hfd-fed, n = 8) and *Tst*$^{-/-}$ (chow-fed, n = 6, hfd-fed, n = 7) mice. Data are represented as mean ±SEM. Significance for the basal experiment (**A**) was

calculated using a 2-WAY ANOVA for *genotype* and *diet*. Significance for the clamp (**B**) was calculated for each diet separately using T-tests for *genotype*. * $P < 0.05$, ** $P < 0.01$, *** $P < 0.001$, **** $P < 0.0001$

Table S2. Hydrogen sulfide disposal by hepatocytes and mitochondria (Amperometry)

nmoles/min/mg protein	C57Bl/6J	*Tst*$^{-/-}$	Significance
Hepatocytes	3.88 +/- 0.095	4.15 +/- 0.345	**ns**
Hepatocytes (Respiratory)	1.97 +/- 0.176	2.91 +/- 0.288	*
Hepatocytes (Non-respiratory)	1.91 +/- 0.181	1.24 +/- 0.117	*
Liver Mitochondria	0.65 +/- 0.095	1.23 +/- 0.129	*
Liver Mitochondria (Respiratory)	0.26 +/- 0.060	0.50 +/- 0.080	*

*** P < 0.05**

Table S2. *Tst* deletion results in increased respiratory H_2S disposal by hepatocytes. Related to Figure 2 and Table 1. H_2S disposal rates (measured by gas selective amperometry following addition of 10 µM Na_2S) of hepatocytes (n = 6/genotype), or isolated liver mitochondria (n = 7/genotype) of ND-fed C57Bl/6J and *Tst*$^{-/-}$mice. Rates of H_2S disposal were measured with and without respiratory inhibition following addition of Antimycin (2µM). Antimycin insensitive disposal rates are referred to as non-respiratory. The Antimycin sensitive disposal rates are referred to as respiratory. Data are represented as mean ±SEM. Significance was calculated using paired two-tailed student's t-test. * P < 0.05.

Table S4. Sulfide metabolism proteins in liver proteome (*Tst*$^{-/-}$ vs C57Bl/6J, ND-fed)				
Feature ID	**Name**		**Fold Change**	**Significance**
Q3UW66	MPST	Mercaptopyruvate sulfurtrasferase	1.27	**
Q8R086	SUOX	Sulfite Oxidase	1.06	Ns
Q3UDS4	SQOR	Sulfide quinone reductase-like	1.06	Ns
Q91WT9	CBS	Cystathionine beta-synthase	1.03	Ns
Q9DCM0	ETHE1	Ethylmalonic encephalopathy 1	-1.01	Ns
Q8VCNS	CTH	Cystathionine gamma-lyase	-1.02	Ns

*** Raw P < 0.05, ** Adjusted P < 0.05**

Table S4. *Tst* deletion selectively regulates MPST in the sulfide pathway of normal diet–fed mice. Related to Figure 3 and Table 3. Relative peptide abundance of proteins of the sulfide production and disposal pathway from the liver proteome of normal diet (ND) fed mice. 'Fold Change' indicates the relative abundance of the protein in *Tst*$^{-/-}$ relative to C57Bl/6J.

Table S5. GO terms - Nutrient metabolism; reduced in ND *Tst*$^{-/-}$ liver (*Tst*$^{-/-}$ vs C57Bl/6J liver, ND-fed)

GO-ID	Name	Genes	Significance
0006629	Lipid metabolic process	19	**
0006631	Fatty acid beta-oxidation	7	**
0003995	Acyl-CoA dehydrogenase activity	3	*
0047617	Acyl-CoA hydrolase activity	2	*

*** P < 0.05, ** P < 0.01**

Table S5. *Tst* Deletion results in reduction of selective fatty acid specific GO terms. Related to Figure 3 and Table 3. Significant GO terms (glucose or lipid related) represented by proteins that are less abundant in the ND-fed *Tst*$^{-/-}$ liver compared with ND-fed C57Bl/6J. 'Genes' indicates the number of genes in the *Tst*$^{-/-}$ that represent the changes driving the GO term.

Table S6 Insulin regulated proteins in *Tst*$^{-/-}$ and C57Bl/6J mice

(A) Abundance of peptides of insulin–induced proteins (*Tst*$^{-/-}$ vs C57Bl/6J, ND-fed)

Feature ID	Name	Fold change	Significance
Q3UGT1	CPT1A	1.03	Ns
P19096	FASN	-1.04	Ns
Q3UDA8	CPT2	-1.05	Ns
Q3V2G1	APOA1	-1.10	Ns
Q5SVI5	GCK	-1.14	*

(B) Abundance of peptides of insulin–suppressed proteins (*Tst*$^{-/-}$ vs C57Bl/6J, ND-fed)

Feature ID	Name	Fold change	Significance
QO5421	CYP2E1	1.13	**
Q9D6M3	SLC25AA2	-1.03	Ns
Q8CI37	PCK1	-1.09	Ns
Q3UJ70	HMGCS1	-1.09	Ns
O08601	MTTP	-1.20	**

(C) Abundance of peptides of insulin–induced proteins (*Tst*$^{-/-}$ vs C57Bl/6J, High Fat-fed)

Feature ID	Name	Fold change	Significance
Q3UGT1	CPT1A	1.03	Ns
P19096	FASN	-1.04	Ns
Q3UDA8	CPT2	-1.05	Ns
Q3V2G1	APOA1	-1.1	Ns
Q5SVI5	GCK	-1.14	*

(D) Abundance of peptides of insulin–suppressed proteins (*Tst*$^{-/-}$ vs C57Bl/6J, High Fat-fed)

Feature ID	Name	Fold change	Significance
QO5421	CYP2E1	-1.05	Ns
Q9D6M3	SLC25AA2	-1.01	Ns
Q8CI37	PCK1	1.09	Ns
Q3UJ70	HMGCS1	-1.04	Ns
O08601	MTTP	1.09	*

*** Raw P < 0.05, ** Adjusted P < 0.05**

Table S6. Proteins regulated by insulin are broadly comparable in expression between *Tst*$^{-/-}$ and C57Bl/6J. Related to Figure 3. Relative abundance in proteins that are known to be induced (A) or suppressed

(B) by insulin in the liver, from the liver proteome of normal diet fed mice. ‘Fold Change’ indicates the relative abundance of the protein in *Tst*$^{-/-}$ relative to C57Bl/6J. Relative abundance in proteins that are known to be induced (C) or suppressed (D) by insulin in the liver, from the liver proteome of high fat diet fed mice. ‘Fold Change’ indicates the relative abundance of the protein in *Tst*$^{-/-}$ relative to C57Bl/6J.

Table S7. KEGG pathways shared by high fat feeding and TST deletion

Entry	Name	Comparison	Significance
A. Shared up-regulated pathways			
00260	Glycine, serine and threonine metabolism	*Tst*$^{-/-}$ vs 6J	**
		HFD vs ND	**
B. Shared down-regulated pathways			
00980	Metabolism of xenobiotics by cytochrome P450	*Tst*$^{-/-}$ vs 6J	****
		HFD vs ND	*
00982	Drug metabolism – cytochrome P450	*Tst*$^{-/-}$ vs 6J	****
		HFD vs ND	*
04142	Lysosome	*Tst*$^{-/-}$ vs 6J	**
		HFD vs ND	****
04390	Hippo signaling pathway	*Tst*$^{-/-}$ vs 6J	**
		HFD vs ND	****
05215	Prostate cancer	*Tst*$^{-/-}$ vs 6J	**
		HFD vs ND	*
04024	cAMP signaling pathway	*Tst*$^{-/-}$ vs 6J	*
		HFD vs 6J	*
04141	Protein processing endoplasmic reticulum	*Tst*$^{-/-}$ vs 6J	*
		HFD vs 6J	**
05211	Renal cell carcinoma	*Tst*$^{-/-}$ vs 6J	*
		HFD vs 6J	*
04722	Neurotrophin signaling pathway	*Tst*$^{-/-}$ vs 6J	*
		HFD vs 6J	*
04110	Cell cycle	*Tst*$^{-/-}$ vs 6J	*
		HFD vs 6J	**
04918	Thyroid hormone synthesis	*Tst*$^{-/-}$ vs 6J	*
		HFD vs 6J	***
04612	Antigen processing and presentation	*Tst*$^{-/-}$ vs 6J	*
		HFD vs 6J	**

*** P < 0.05, ** P < 0.01, *** P < 0.001 **** P < 0.0001**

Table S7. KEGG Pathways shared by high fat feeding and TST deletion. Related to Figure 3. (**A**) KEGG pathways that are significantly up-regulated in the same direction by both high fat diet (HFD vs ND), and *Tst* deletion (*Tst*$^{-/-}$ vs C57Bl/6J). (**B**) KEGG pathways that are significantly down-regulated in the same direction by both high fat diet (HFD vs ND), and *Tst* deletion (*Tst*$^{-/-}$ vs C57Bl/6J). 'Comparison' indicates the two groups being compared.

Table S8. Effect of high fat feeding on sulfide pathway proteins (High fat diet vs ND-fed)

Feature ID	Name	Fold change in 6J	Significance	Fold change in *Tst*$^{-/-}$	Significance
Q3UW66	MPST	1.35	**	1.15	*
Q8R086	SUOX	1.21	**	1.23	**
Q545S0	TST	1.19	Ns	n/a	n/a
Q8VCNS	CTH	-1.04	Ns	-1.06	Ns
Q9DCM0	ETHE1	-1.05	Ns	1.03	Ns
Q3UDS4	SQOR	-1.08	Ns	1.01	Ns
Q91WT9	CBS	-1.10	*	-1.06	Ns

*** Raw P < 0.05, ** Adjusted P < 0.05**

Table S8. Effect of high fat feeding on the sulfide pathway of C57Bl/6J and *Tst*$^{-/-}$ mice. Related to Figure 3. Protein abundances of the sulfide production and disposal pathway from the liver proteome of C57Bl/6J and *Tst*$^{-/-}$ mice. 'Fold Change' indicates the relative abundance of the protein in high fat diet fed mice relative to normal diet fed mice, shown separately for each genotype.

Table S9. Pathways in *Tst*$^{-/-}$ that are regulated oppositely to high fat feeding

Entry	Name	Comparison	Direction
A	**KEGG Pathways**		
00980	Metabolism of xenobiotics by cytochrome P450	*Tst*$^{-/-}$ vs 6J	Decreased
		HFD vs ND	Increased
00983	Drug metabolism – other enzymes	*Tst*$^{-/-}$ vs 6J	Decreased
		HFD vs ND	Increased
00053	Ascorbate and aldarate metabolism	*Tst*$^{-/-}$ vs 6J	Decreased
		HFD vs ND	Increased
00040	Pentose and glucoronate interconversions	*Tst*$^{-/-}$ vs 6J	Decreased
		HFD vs ND	Increased
00830	Retinol metabolism	*Tst*$^{-/-}$ vs 6J	Decreased
		HFD vs ND	Increased
B	**GO Terms**		
0006629	Lipid metabolic process	*Tst*$^{-/-}$ vs 6J	Decreased
		HFD vs ND	Increased
0006631	Fatty acid beta-oxidation	*Tst*$^{-/-}$ vs 6J	Decreased
		HFD vs ND	Increased
0003995	Acyl-CoA dehydrogenase activity	*Tst*$^{-/-}$ vs 6J	Decreased
		HFD vs ND	Increased
0047617	Acyl-CoA hydrolase activity	*Tst*$^{-/-}$ vs 6J	Decreased
		HFD vs ND	Increased

Table S9. KEGG pathways and GO terms that are regulated in the opposite direction by high fat feeding compared to Tst deletion. Related to Figure 3. (**A**) KEGG pathways that are regulated in the opposite direction by high fat diet (HFD-fed C57Bl/6J vs ND-fed C57Bl/6J), to *Tst* deletion (ND-fed *Tst*$^{-/-}$ vs C57Bl/6J). (**B**) GO terms that are regulated in the opposite direction by high fat diet (HFD-fed C57Bl/6J vs ND-fed C57Bl/6J), to *Tst* deletion (ND-fed *Tst*$^{-/-}$ vs C57Bl/6J). 'Comparison' Indicates the two groups being compared. 'Direction' indicates whether the protein abundance is decreased or increased in the first group relative to the second.

Supplemental Spreadsheet Table S3

Click here to access/download

Supplemental Videos and Spreadsheets

Table S3 Excel.xlsx